12-2013

EFFECT OF GRAPHITIC CARBON NANOMODIFIERS ON THE ELECTROMAGNETIC SHIELDING EFFECTIVENESS OF LINEAR LOW DENSITY POLYETHYLENE NANOCOMPOSITES

Byron Villacorta Hernandez
Clemson University, bvillac@clemson.edu

EFFECT OF GRAPHITIC CARBON NANOMODIFIERS ON THE ELECTROMAGNETIC SHIELDING EFFECTIVENESS OF LINEAR LOW DENSITY POLYETHYLENE NANOCOMPOSITES

A Dissertation
Presented to
The Graduate School of
Clemson University

In Partial Fulfillment
Of the Requirement for the Degree
Doctor of Philosophy
Chemical Engineering

---

by
Byron S. Villacorta Hernandez
December 2013

Accepted by:
Dr. Amod A. Ogale, Committee Chair
Dr. Todd H. Hubing
Dr. Douglas E. Hirt
Dr. Christopher L. Kitchens

ABSTRACT

Conductive polymer composites have become alternative materials for providing electromagnetic and electrostatic shielding where metals are not suitable. Polymer composites prepared with carbon nanomodifiers are corrosion-resistant, light-weight, and easy to process. Moreover, due to their nano-scale, nanocomposites can be shaped into thin-walled forms such as micro-injection molded or micro-textured extruded parts and films. The composite community has devoted considerable effort to the study and development of such composites for enhanced electrical conductivity. However, the electromagnetic shielding effectiveness (EM SE) of composites consisting of carbon nanomodifiers with medium to high concentrations has not been thoroughly examined. Therefore, in this study, the effect of crystallinity, morphology, concentration and orientation of carbon nanomodifiers on the shielding provided by their polyethylene-based composites has been investigated relative to their transport properties.

First, the electrical properties and EM SE of composites consisting of heat-treated carbon nanofibers (Pyrograf®-III PR-19 CNF) in a linear low density polyethylene (LLDPE) matrix were assessed. Heat treatment (HT) of CNF at 2500°C significantly improved their graphitic crystallinity and intrinsic transport properties, thereby increasing the EM SE of the nanocomposites. Thus, twin-screw extruded composites containing 10 vol% heat-treated PR-19 displayed a conductivity of about 10 S/m, about ten orders of magnitude better than that of the composites containing as-received nanofibers. Over a frequency range of 30 MHz to 1.5 GHz, nanocomposites containing PR-19 HT displayed

EM SE values of about 14±2 dB. Absorption was determined to be the main shielding component for the heat-treated CNF nanocomposites. The nanocomposites possessed a tensile modulus of 632±36 MPa (about twice of that of pure LLDPE). Although the strain-to-failure was about one-third that of pure LLDPE, the absolute value of 180±98% indicates a significant retention of ductility.

Second, the influence of the morphology of carbon modifiers on the electrical, thermal and mechanical properties of their composites was investigated. Four heat-treated carbon modifiers were investigated: PR-19 HT carbon nanofibers, multi-walled carbon nanotubes (MWNT HT), helical multi-walled carbon nanotubes (HCNT HT), and pitch-based P-55 carbon fibers (CF). These were melt-mixed with LLDPE in a Haake Rheomix 600 batch mixer at 10 vol%. The EM SE of the composites exhibited dependence on the modifier morphology. Thus, MWHT HT, with the highest aspect ratio, led to the largest composite electrical and thermal conductivities (34 S/m, 1 W/m.K) and EM SE (~24 dB). In contrast, HCNT HT, due to their coiled shape and low aspect ratio, led to a non-percolating microstructure in the composites, which produced poor EM SE (<1 dB). Nonetheless, HCNT HT composites displayed the highest ductility (~250%) and flexibility, which is probably owed to the matrix-modifier mechanical bonding (interlocking) provided by the helical morphology.

Using the carbon modifiers that previously led to the best EM SE (i.e., PR-19 HT and MWNT HT), the influence of composite electrical properties on the plane-wave EM SE in the VHF-UHF bands was studied further. Both graphitic nanomodifiers were dispersed in LLDPE matrix to produce a nominally random in-plane modifier orientation.

For a concentration of 10 vol% nanomodifiers, EM SE values of 22 dB and 24 dB were obtained for PR-19 HT and MWNT HT nanocomposites (2.5-mm thick), respectively. At a high concentration of 40 vol%, EM SE values as high as 68 dB and 55 dB were respectively attained. Because such nanocomposites possess only moderate electrical conductivity, a model for generally-lossy materials was used to predict the plane-wave EM SE and its components. Based on the material properties of the nanocomposites, the predicted values of EM SE were found to be consistent with the experimental values.

Finally, the electrical conductivity and EM SE of nanocomposites that contained 10 vol% of oriented graphitic nanomodifiers (PR-19 HT and MWNT HT) in LLDPE are reported. Micro-filament spinning was used to generate flow-induced orientation of the carbon nanomodifiers. Consequently, the conductivity of the resulting nanocomposites exhibited anisotropy. Thus, the in-plane conductivity in the longitudinal direction (PR-19 HT comp.: ~0.02 S/m; MWNT HT comp.: ~3 S/m) was at least an order of magnitude higher than that along the transverse direction. As measured with a rectangular waveguide (WR510, 1.45-2.2 GHz), the PR-19 HT and MWNT HT oriented nanocomposites (1-mm thick) displayed EM SE values of 0.7±0.4 dB and 3.0±0.8 dB, respectively, when the nanomodifiers were transversely oriented with the polarized electric field. In contrast, when the orientation of the nanomodifiers was parallel with the field, values of 3.2±1.0 dB and 9.0±1.0 dB were obtained, respectively. Therefore, as a result of this anisotropy, as analyzed by polarized electromagnetic waves, the composites displayed anisotropic shielding.

In summary, this study establishes the significance of the use of purified carbon nanomodifiers as suitable modifiers in polyethylene-based composites as multifunctional materials for enhanced electromagnetic shielding.

DEDICATION

As an offering of my firstfruits, this work is dedicated to He who brought me to Clemson with the purpose of revealing Himself to me: The God of Abraham, Isaac and Jacob; the God of Israel, Father of my Lord and King Jesus Christ, who saved me from sin with His own precious blood, and has graciously granted me the gift of everlasting life through faith in Him. To Him be the Glory, and Kingdom, Dominion and Power, forever and ever. Amen.

As my beloved grandmother Mrs. Elina E. Hernández used to say: "Just a little longer…, and we will see Him. Yeah, Face to face, I will see Him!" She fought the good fight of faith, and now rests in Christ awaiting the resurrection of the saints on such a Glorious Day of His Parousia.

"I Jesus have sent mine angel to testify unto you these things in the churches. I am the root and the offspring of David, and the bright and morning star. And the Spirit and the bride say, Come. And let him that heareth say, Come. And let him that is athirst come. And whosoever will, let him take the water of life freely". Rev. 22:16-17, KJV.

"He which testifieth these things saith, Surely I come quickly. Amen. Even so, come, Lord Jesus". Rev. 22:20, KJV.

Yeah, come, Lord…, to reestablish all things. Maranatha!

ACKNOWLEDGEMENTS

I would like to thank those who provided emotional, moral, academic and technical support for the completion of this research.

First of all, with great love and gratitude, I want to thank my precious wife, Mrs. Sara N. Peralta de Villacorta and my beloved son, Byron S. Villacorta Peralta for the unconditional support, self-sacrifice, encouragement and love they provided me over these years of wilderness. This work also belongs to both of you! I love you with all my heart and strength!

I want to specially thank my lovely parents: Mr. Roberto R. Villacorta and Mrs. Reina E. Hernández de Villacorta for the unconditional love, effort and patience that they have always dedicated to me. I particularly thank them for their prayers and moral support which have certainly helped me crown this victory. God bless you both!

I thank my brother Mr. Josue R. Villacorta, who I love with all my heart, for always being by my side during the times of suffering and trials. To my dear sister Mrs. Ericka Y. Villacorta de Cristales who has always cheered me up with her affection and tenderness. Without forgetting my lovely Grandmother Mrs. Concepción de Maria Marroquín whose love has made my life just special.

With the greatest appreciation, I am also deeply grateful to my advisor, Dr. Amod A. Ogale, whose support, mentoring, and patience guided me throughout these academic years to accomplish the research goals of this work. Many thanks Dr. Ogale!

I would like to thank to such an awesome professor, Dr. Todd H. Hubing, who so enthusiastically took the function of my co-advisor, helping me with the challenges that the electrical characterization of this work conveyed. Thank you Dr. Hubing!

Sincerely, I want to extend my thanks to my committee members, Dr. Douglas E. Hirt and Dr. Christopher L. Kitchens for teaching me the introductive grad-courses in the field of Chemical Engineering and whose valuable input also contributed to this study.

Dr. Ogale's research group members: Dr. Young-Pyo Jeon, Mrs. Ozgun Ozdemir, Mrs. Meng Zhang, Ms. Jin Jing, Mr. Sam Lukubira, Mr. Marlon Morales and Ms. Rebecca Always-Cooper, whose support, help and friendship made me enjoy my stay in Clemson.

I would also like to thank Mrs. Diana Stamey for her support and kindness when purchasing and dealing with administrative affairs.

I finally thank the Center for Advanced Engineering Fibers and Films for the financial support of this research through the ERC program of the National Science Foundation.

May the Lord bless you all!

TABLE OF CONTENTS

Page

Table of Contents (Continued)

Page

Table of Contents (Continued)

Page

Table of Contents (Continued)

Page

LIST OF TABLES

LIST OF FIGURES

List of Figures (Continued)

Figure Page

List of Figures (Continued)

Figure Page

List of Figures (Continued)

Figure Page

List of Figures (Continued)

Figure Page

List of Figures (Continued)

Figure Page

List of Figures (Continued)

Figure Page

List of Figures (Continued)

Figure Page

CHAPTER 1

INTRODUCTION

1.1 Introduction to conductive nanocomposites

As illustrated in **Figure 1.1**, most polymers are insulating materials that possess very low electrical and thermal conductivities in the ranges of 10^{-13}-10^{-17} S/m and 0.05-1.0 W/m.K, respectively [1, 2]. Therefore, it is necessary to add conductive modifiers to these polymeric resins to produce composites with enhanced transport properties [3, 4]. Conductive compounds such as metallic and carbonaceous conductive modifiers have been added into these insulative matrices to increase their electrical and thermal properties [5-9]. Of particular interest are carbon materials due to their low density, high strength, and outstanding corrosion resistance as compared with metals [7, 8]. This opens an opportunity for different applications [10-13].

During the 1990's decade, the availability of carbon nanomodifiers opened further applications of electrically dissipative and conductive materials [14]. The ease of processing offered by melt-mixing of such nanomodifiers in thermoplastic polymers, and the possibility of producing very thin-walled nanocomposites structures such as films, fibers and micro-injected parts, have been the driving force for the utilization of nanomodifiers in niche applications [15]. These applications range from electrostatic dissipative packaging films and electromagnetic shielding enclosures and gaskets, to novel antennas and radio frequency ID devices [16].

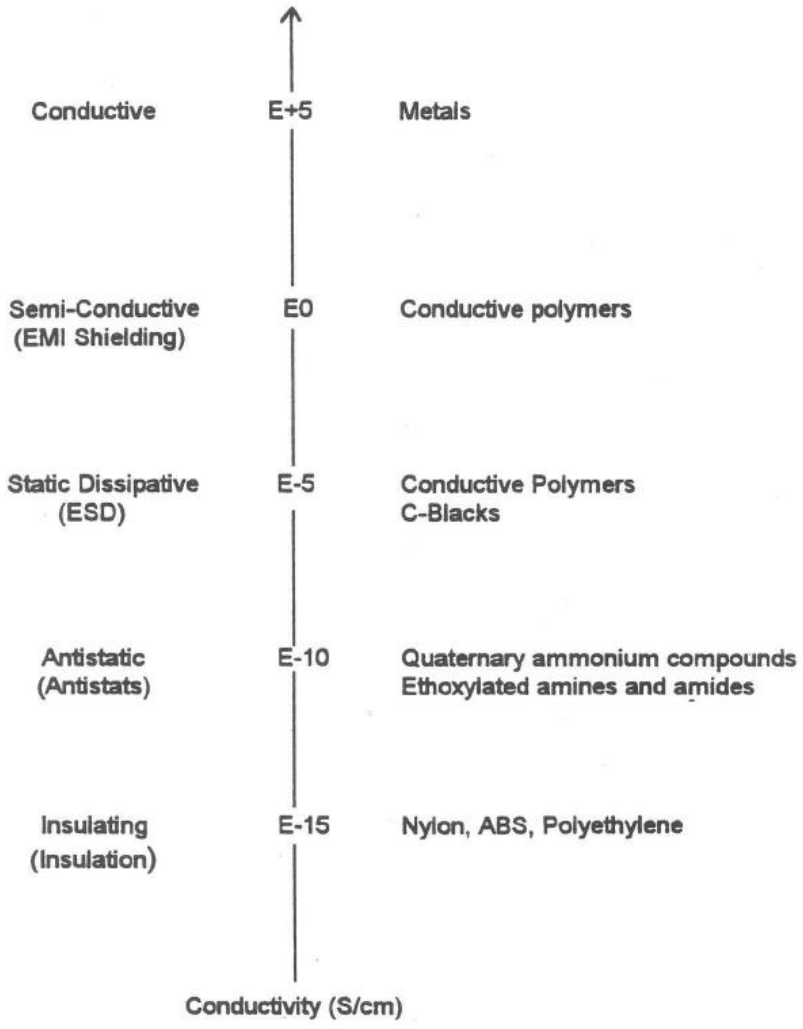

Figure 1.1. General classifications of the conductivities of different materials and their type of applications [13].

Different thermoplastic and thermoset resins modified with various types of modifiers are currently being investigated and commercialized for numerous applications [17]. It has been reported that these advanced materials are used in applications estimated at about US$30 billion worldwide [18]. The industrial applications include automotive,

aerospace, energy, electronics, healthcare, and infrastructure [18]. Specifically, the global market of electro-conductive polymeric materials is expected to be of about US$ 3 billion by 2014, with about 85% of current demand being for conductive polymer composites [19].

Polyolefins, such as polyethylene and polypropylene, are currently one of the largest groups of commodity polymers [20]. Their versatile properties range from the flexibility and ductility of linear low density polyethylene (LLDPE) to the stiffness and strength of polypropylene (PP). Their chemical and thermal stability, low processing temperatures, and low cost, are great factors that promote their utilization. In 2009, about 120 million tons of polyolefins were produced worldwide [20]. These economical and technical aspects motivate the search for advanced multifunctional composite materials that meet these requirements. Therefore, the present study was focused on investigating the transport properties of conductive composites made of graphitic carbon nanomodifiers and a ductile polyolefin matrix (linear low density polyethylene), in relation to their electromagnetic shielding effectiveness (EM SE). The following sections introduce these topics, and provide a review of the literature associated with this field of study.

1.2 Carbon nanoforms

With the discovery of carbon nanotubes by Iijima in 1991, a great deal of effort has been dedicated to the synthesis, modification, characterization, and application of different nano-sized carbon forms [21-27]. Carbon nano-whiskers, nano-cones, nano-

polyhedral crystals, nanoplatellets, nano-onions, nanohorns, and mainly, multi-walled carbon nanotubes and vapor-grown carbon nanofibers have been investigated in various literature studies [24, 27, 28].

1.2.1 Morphology of carbon nanoforms

Carbon nanotubes (CNT) consist of axially aligned single or multiple concentric graphene layers with diameters of 1-100 nm and lengths as large as 10 μm [29]. Carbon nanofibers (CNF) are a form of discontinuous graphitic filament with their multiple graphene layers arranged at certain angles with respect to the fiber axis. CNF have diameters that range 100-300 nm and lengths from 1 to 50 μm [29].

The nano-scale and the outstanding transport and mechanical properties of carbon nanofibers and nanotubes have been the major driving force for their potential utilization [25, 26, 30, 31]. Such properties are a direct consequence of their graphitic crystalline structure and of a variety of morphologies including different shapes, surfaces and high aspect ratios (i.e, length/diameter ratio) [24, 32-34]. **Figures 1.2** and **1.3** display electron micrographs showing different morphological features of commercial and experimental carbon nanofibers and carbon nanotubes, respectively.

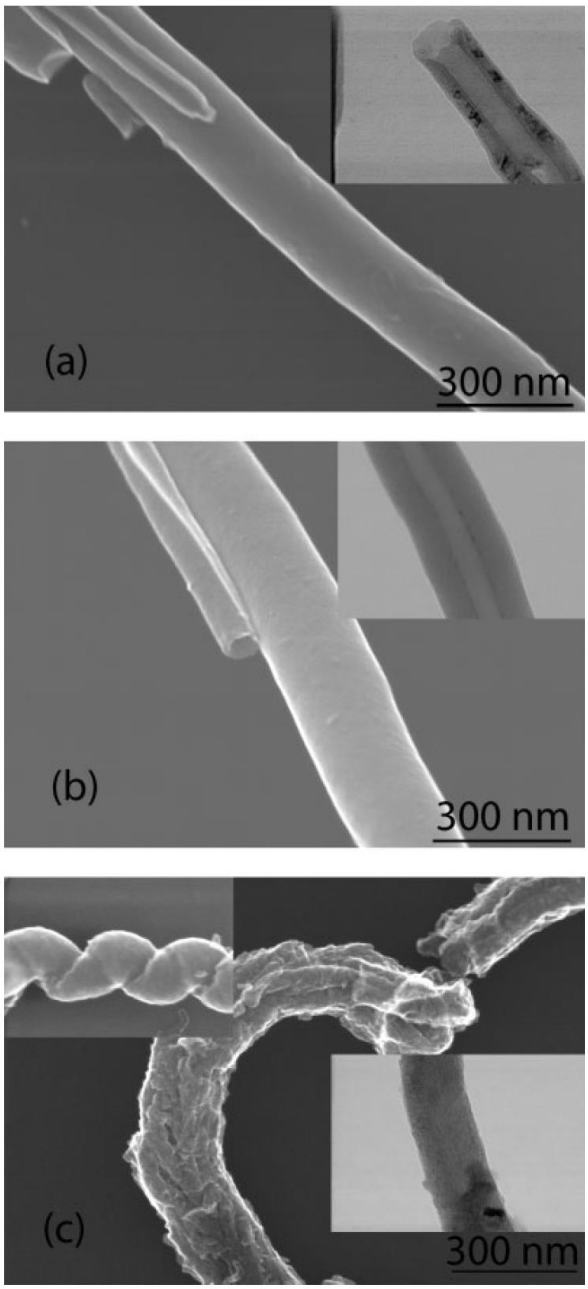

Figure 1.2. Scanning transmission electron microscopy (STEM) micrographs of carbon nanofibers (a) PR-19 (Pyrograf III, Applied Science Inc.) and (b) PR-24 (Pyrograf III, Applied Science Inc.) and (c) experimental MJ (Myongji University) carbon nanofibers. The insets are transmission electron micrographs. Adapted from [33].

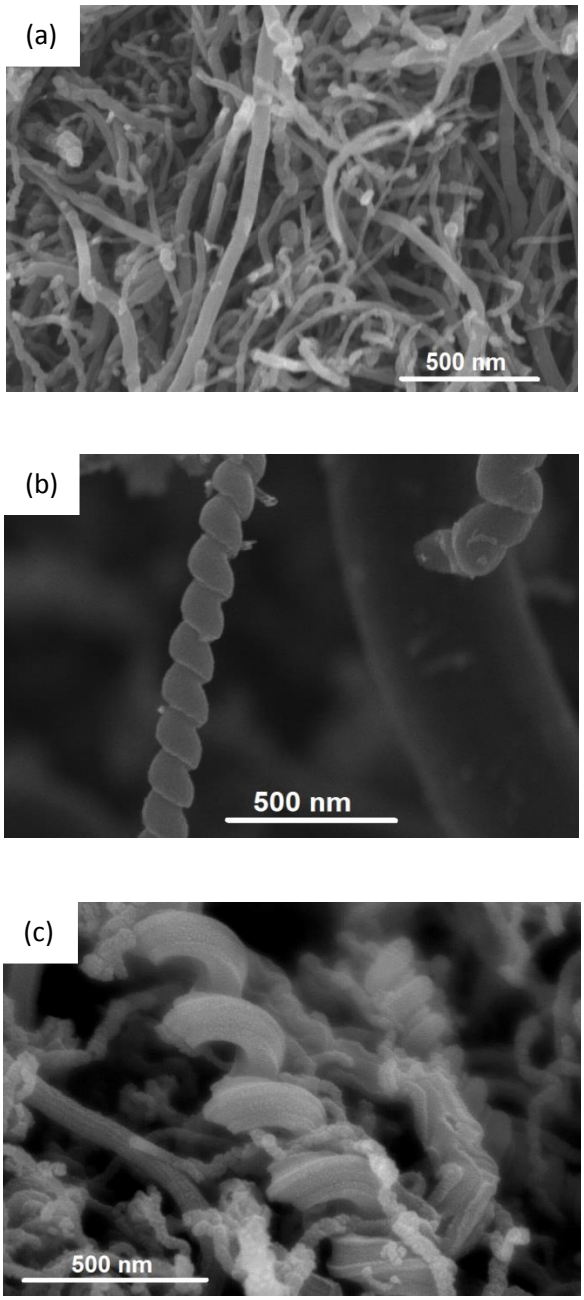

Figure 1.3. Scanning electron micrographs of carbon nanotubes (a) straight multi-walled carbon nanotubes (CheapTubes Inc.), (b) helical multi-walled carbon nanotubes (CheapTubes Inc.), and (c) experimental multi-walled carbon nano-springs (Clemson University).

1.2.2 Purification of carbon nanoforms

Carbon nanoforms are typically produced by catalytic processes, such as chemical vapor deposition (CVD), at relatively low temperatures (<1000°C) [25, 34]. This leads to low graphitic crystallinity with many crystallographic defects. It also results in the generation of amorphous carbon and other residual catalytic impurities, which unfortunately reduce their properties [25, 35]. Nonetheless, it is widely known that in their highly purified state, nanoforms exhibit outstanding transport properties [25, 27, 32, 35]. Therefore, chemical treatments are necessary to enhance the purity and graphitic crystallinity of these forms. For some carbonaceous materials, heat-treatment to graphitization temperatures (>2000°C) is conducted for the enhancement of their lattice-dominated properties [27].

Figure 1.4 is a schematic representation of the stages of the mechanism of graphitization as function of the heat-treatment temperature (HTT) of pitch-like carbon precursors. During stage 1 (< 1000°C), the basic graphitic structural units are isolated and unoriented. In stage 2 (1000°C -1500°C), densification takes place, making the basic graphitic structural units grow into isolated oriented columns. It is during this stage, that the elimination of heteroatoms produces pores. Between 1500°C and 2000°C, the stage 3 occurs; the basic graphitic structural units grow and orient themselves forming distorted layers of turbostratic carbon. Finally, above 2000°C, the final stage perfects the graphitic structure forming planar layers, allowing the growth of crystals [27].

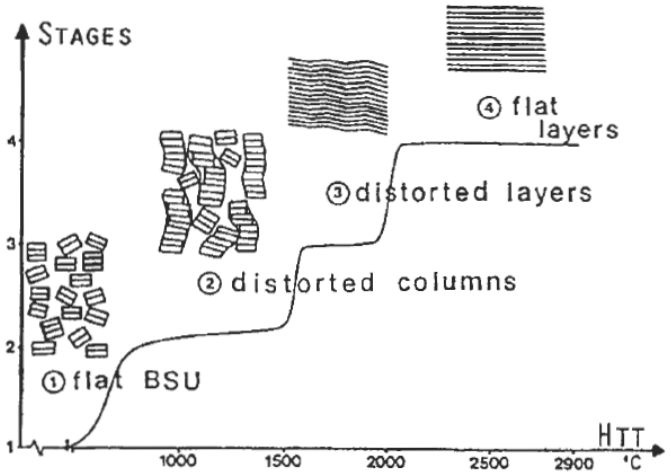

Figure 1.4. Schematic representation of the mechanism of graphitization. Adapted from [27].

The assessment of graphitic crystallographic characteristics of carbonaceous materials can be carried out by means of X-ray diffraction and Raman spectroscopy [35, 36]. For graphitic carbon, X-ray diffractograms display prominent peaks at about 26°, 42° and 44° Bragg's angular positions (2θ) corresponding to reflections of the (002), (100) and (101) planes, respectively [27]. These angular positions and their intensities indicate the interlaying spacing between the graphene layers, the crystallites thickness and width, and their orientation [27].

Raman spectroscopy is also sensitive to graphitic structures. The Raman scattering is the inelastic scattering of photons, generated by the vibrating molecular bonds [37]. In carbonaceous materials, the most important peaks occur at about 1300 cm^{-1} and 1650 cm^{-1} and are known as the D (disordered) and G (graphitic) bands. The ratio of the integrated intensities of the D peak to the G peak (Raman I_D/I_G ratio) varies

inversely with the crystal width, L_a, and is a measure of the level of graphitic crystallinity [38, 39].

1.2.3 Transport properties

The electrical and thermal conductivities of graphitic carbon forms depend on different microstructural features, such as crystal structure, crystal size, crystallographic defects, aspect ratio, shape, and in the case of carbon nanotubes, their chirality [25, 27, 32, 33, 39]. Due to such a large variety of features, a wide range of properties have been reported. For instance, carbon nanotubes can display either semi-metallic or metallic behavior depending on their chirality [28], and bulk electrical resistivities ranging from 0.02 to 2 Ω·cm (two orders of magnitude apart) have been reported for carbon nanofibers and nanotubes [35, 40, 41].

The measurement of the transport properties in single carbon nanoforms is challenging. Therefore, measurements are conducted on aligned bundles of carbon nanoforms, and estimates worked out for single forms. Thus, Zhou et al. measured an electrical resistivity of about 2.4×10^{-4} Ω·cm at 300K from a bundle of aligned single-walled carbon nanotubes (SWNT) [28]. Similarly, an estimated value of ~10^{-4} Ω·cm for a single SWNT and about 10^{-3} Ω·cm from an aligned micro-bundle at room temperature have been reported [25]. Yang reported recently an axial resistivity of 3.5×10^{-3} Ω·cm from aligned bundles of MWNT, and a transverse resistivity of 4.4×10^{-3} Ω·cm at 300K [42]. Accordingly, for the same aligned bundle of MWNT, he reported a thermal conductivity of 30 W/m.K and 18 W/m.K for the axial and transverse measurements,

respectively [42]. For bulk MWNT foils a similar thermal conductivity of 20 W/m.K has been measured [43]. Thus, the bundle transport values are at least one order of magnitude smaller than those of the pure graphite (10^{-4} Ω·cm, 2000 W/m.K) [44]. This means that the outstanding properties associated with single nanoforms are not as effective due to particle-particle contact resistance that limits the large-scale diffusion of electrons and phonons [25, 28]. Therefore, the knowledge of the bulk properties of these nanomaterials is more useful than that of single forms for their use in bulk composites.

1.2.4 Mechanical properties

In theory, due to the strength associated with the C-C bond, carbon nanotubes should be the stiffest and strongest materials [28]. Individual carbon nanotubes also show extraordinary resilience properties, which allow them to sustain a great deal of elastic deformation [45, 46]. This premise, coupled with the low density of carbon materials, is the motivation for investigating carbon nanomodifiers as mechanical reinforcing agents in potential structural applications.

Average values of Young's modulus of about 1 TPa and 30 GPa have been reported for arc-grown and catalytically CVD-grown multi-walled carbon nanotubes, respectively [26, 45]. These moduli values are about five times the modulus of steel. Moreover, tensile strength values as high as 60 GPa have also been reported for single MWNT, which is about 50 times greater than that of steel [26]. In a review, Al-Saleh and Sundararaj reported values of modulus and strength of vapor grown carbon nanofibers of

about 250 GPa and 3 GPa, respectively [47]. Koo reported moduli values of vapor grown carbon nanofibers (Pyrograf I and III) of 400 and 600 GPa for as-grown and heat-treated (3000°C) CNFs, respectively [29]. He also reported values of tensile strength of 2.7 and 7 GPa, respectively [29]. The lower tensile properties of CNFs, when compared to CNTs, are a result of their discontinuous graphitic structure. However, these strength values are comparable to those of typical high-strength polyacrylonitrile-based carbon fibers [48].

1.3 Properties of carbon nanomodifier-based nanocomposites

1.3.1 Nanocomposite transport properties

Figure 1.5 is a schematic representation of the dependency of the electrical conductivity of typical composites with respect to the concentration of modifiers added. Initially, as conductive modifiers are added to the insulative matrix, little effect is observed on conductivity because the modifiers form isolated clusters that have almost no electrical interconnection with each other. At this stage, the modifiers have electrical connection only within the clusters, and the total electrical network that they form is highly capacitive [8].

As more modifiers are incorporated, the composite reaches a critical concentration, ϕ_c, at which the modifiers form electrical connections, resulting in a conductive network. When this happens, the composite has reached the percolation threshold and clusters of "infinite" size are formed [8]. From there on, micro-conduction mechanisms take place and the electrons hop and/or tunnel from cluster to cluster across

the composite making the conductivity increase rapidly [8]. This percolation threshold displays an inverse dependency with mean modifiers cluster size, S. Finally, as more modifiers are added to the composite beyond the percolation threshold, the conductivity continues to increase but slowly.

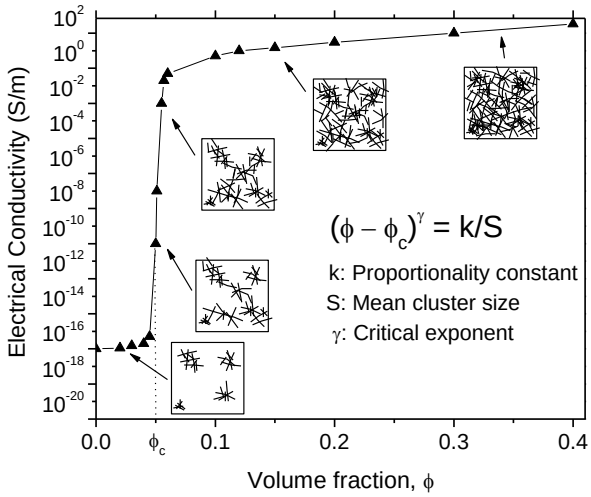

Figure 1.5. Schematic of the typical nanocomposite conductivity and composite clustering microstructure as function of modifier concentration.

Figure 1.6 displays the electrical resistivity (the inverse of conductivity) of LLDPE-based composites made of different CNF types that lead to different percolation thresholds [33]. The threshold has been found to be highly dependent on the intrinsic conductivity of the modifiers, their morphology and aspect ratio, as well as on the chemical nature of the polymeric matrix [33]. For polyolefin-based carbon nanofiber composites, typical percolation threshold ranges from 2.5 to 7.5 vol% [6, 39]. For MWNTs, percolation thresholds as low as 0.25 to 1 vol% in polypropylene (PP), 0.5-1.25

vol% in low density polyethylene (LDPE) and 0.5-2.5 vol% in high density polyethylene (HDPE) have been reported [49].

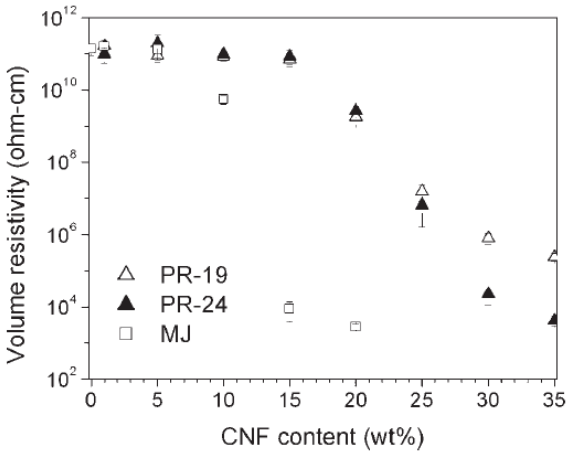

Figure 1.6. Volume resistivity of composites made of LLDPE matrix with three different carbon nanofiber types. Adapted from [33].

Literature studies have established that the electromagnetic shielding effectiveness (EM SE) of a composite is a strong function of its transport properties, and particularly of its electrical conductivity [6, 35, 50]. **Figure 1.7** depicts a positive correlation between the EM SE (X-band: 8.2-12.4 GHz) and the conductivity of various grades of carbon-based ethylene-vinyl acetate/ethylene-propylene-diene rubber (EVA/EPDM) 50/50 vol% composites [51]. Moreover, since the conductivity of a composite depends on the concentration of the conductive modifiers, the EM SE also displays a dependency on concentration. **Figure 1.8** displays a positive correlation between the X-band EM SE and the concentration of MWNT/poly(trimethylene terephthalate) (PTT) composites [52].

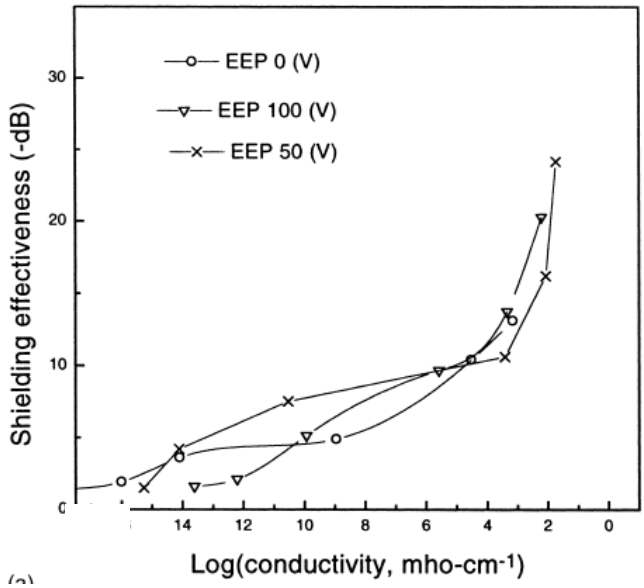

Figure 1.7. Correlation between the X-band EM SE and volume electrical conductivity of carbon-based EVA-EPDM. Adapted from [51].

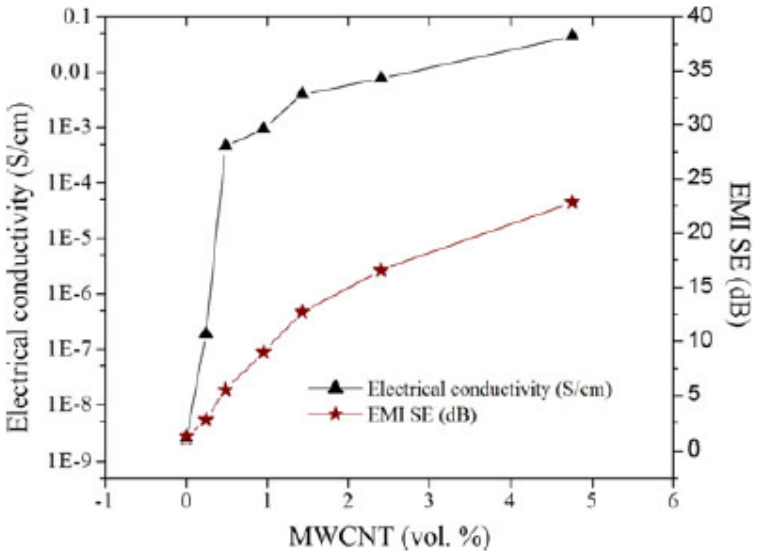

Figure 1.8. Conductivity and electromagnetic shielding effectiveness of MWNT/PTT composites as function of their nanomodifier concentration. Adapted from [52].

While the electrical conductivity accounts for the conductive loss effects, the AC electrical permittivity accounts for their dielectric lossy effects [35]. **Figure 1.9** exhibits the relative AC permittivity of MWNT/epoxy composites from 0 to 20 wt% in the X-band frequency range [16]. The real permittivity increases with the concentration due to an increase of surface area provided by the nanomodifiers, which increases the polarization in the composite [35]. The imaginary permittivity or polarization loss also increases with the modifier concentration, but this is due to an increase of enthalpic losses in the composite as the electric field varies with frequency [35].

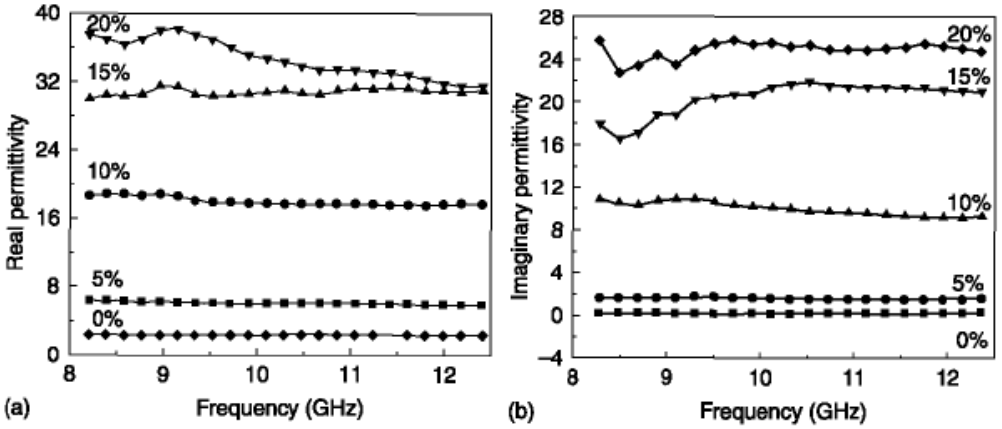

Figure 1.9. Relative AC electrical permittivity of carbon nanotube-based epoxy nanocomposites at various MWNT concentrations: (a) real permittivity and (b) imaginary permittivity. Adapted from [16].

Depending on the frequency range, different relaxation phenomena (interfacial, dipole, ionic, electronic) take place, and the dissipation due to dielectric losses depends on how close the frequency is to a relaxation peak [53, 54]. Thus, both permittivity

components depend on frequency, and this dependency becomes more prominent as the content of modifiers increases [55]. Although in a lesser proportion as compared to the conductive losses, these dielectric losses also contribute to the EM SE of these materials depending on the frequency of the waves [35].

Although the electrical and thermal conductivities are correlated for metals, the transport mechanism for phonons is fundamentally different from that of electrons [15]. This mechanistic difference is evident in the thermal conductivity of composites materials, because it is more sensitive to the matrix-modifier interface than is electrical conductivity. Thus, any interface will delay the interfacial phonon transport in the composites [56]. This is one of the reasons for the relatively small enhancement in thermal conductivity obtained by adding conductive modifiers, when compared with that attained in electrical conductivity.

Figure 1.10 displays the thermal conductivity of CNF-based Nylon-11 injection-molded composites as function of their concentration [57]. Rather than a power law relationship, an approximately linear relation is observed. At 7.5 wt%, the thermal conductivity (relative to pure Nylon-11) increased by only 0.05 W/m.K. Nonetheless, for higher concentrations of CNF in polycarbonate, a through-plane thermal conductivity value of about 0.8 W/m.K has been reported at 30 vol% [58].

The thermal conductivity of nanocomposites reported in the literature greatly varies depending on the matrix and nanomodifier types. Thus, for polyolefin-based CNF nanocomposites, values of thermal conductivity ranging from 0.55 to 5.5 W/m.K for

composites with concentrations as high as 40 vol% have been reported [15]. King et al. reported a value of only 0.46 W/m.K for CNT/polypropylene composites at about 7.5 vol% [59]. The thermal conductivity reached by these composites is important in shielding applications, because part of the shielded radiation is converted into heat [55]. Thus, for proper functioning of electronic devices, acceptable levels of heat dissipation are required.

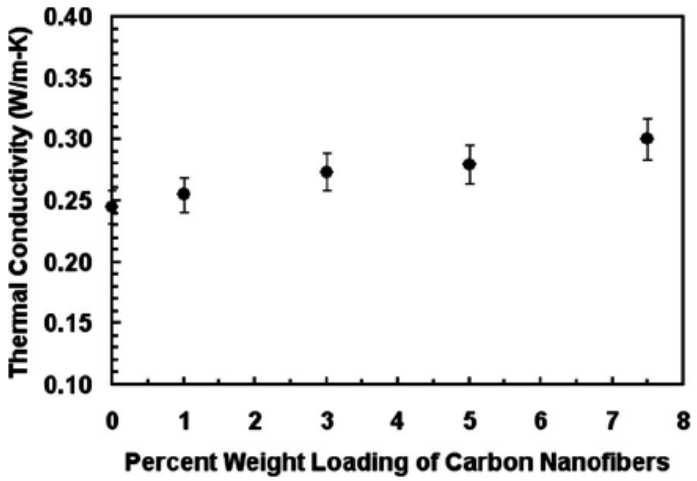

Figure 1.10. Concentration dependency of the through-plane thermal conductivity of CNF/Nylon-11 composites. Adapted from [57].

1.3.2 Nanocomposite mechanical properties

The mechanical properties of nanocomposites are highly dependent on the quality of the matrix-modifier interfacial bonding [56]. The chemical compatibility between the matrix and nanomodifier surface, as well as the mechanical interlocking

between the matrix and the surface roughness/shape of the modifiers play a key role [33, 56]. For polyolefin-based composites systems, there is an intrinsic chemical compatibility advantage as the matrix and the carbon modifiers are both hydrophobic (nonpolar). Thus, modifier shape and surface characteristics are more important. The mechanical performance will determine the type of application in which these can be utilized, i.e., structural enclosures, shielding tapes, gaskets, shielding foams or ESD films [35].

Table 1.1 displays the (a) tensile modulus, E_c , (b) the tensile strength, σ_f, and (c) the strain-to-failure, ε_f, of composites made out of MWNT and a flexible/ductile low density polyethylene (LDPE) as a function of the modifier concentration [60]. Additionally, in **Figure 1.11** the stress-strain curves for the system MWNT/chitosan from pure chitosan to 2 wt% are displayed [61]. In both nanocomposite systems, the flexibility and ductility decrease with the concentration of nanomodifiers, while their strength increases. Nonetheless, a rapid deterioration of strength at higher concentrations usually takes place [55].

Table 1.1. Tensile properties of MWNT/LDPE composites. Adapted from [60].

MWNT content	0%	1%	3%	5%	10%
σ_f [MPa]	10.7	11.8	13.1	14.5	15.6
ε_f [%]	380	320	260	160	12
E_c [GPa]	0.235	0.261	0.284	0.386	0.444

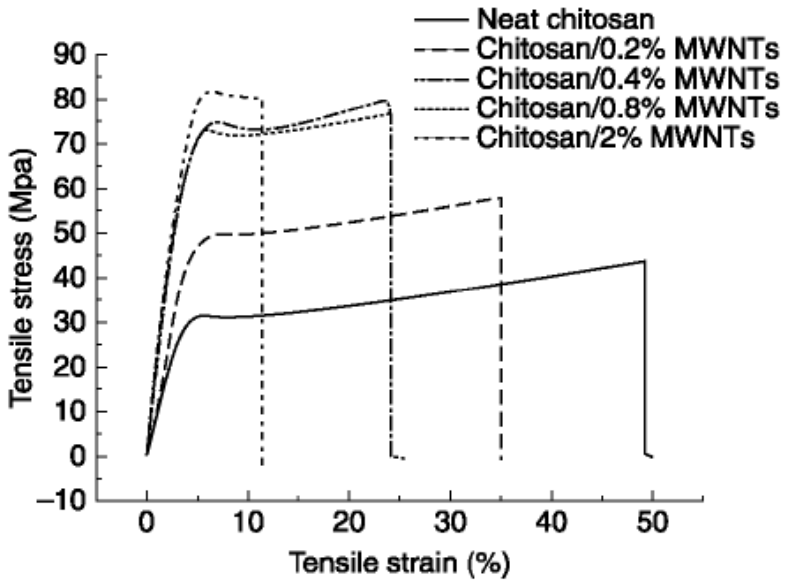

Figure 1.11. Stress-stress curves of chitosan-based carbon nanotube nanocomposites. Adapted from [61].

For different types of as-grown carbon nanofibers in LLDPE at ~15 wt%, Lee et al. reported values of elastic modulus at 300 MPa, strength of ~15 MPa, and ductility of ~100%, whereas pure LLDPE has a strength of 30 MPa and a strain-to-failure of about 700% [33]. Likewise, Morcon & Simon reported that melt-blended MWNT/polybutene composites at only 2 wt% led to a tensile strength of 19.5 MPa, which is ~40% less than that of pure polybutene [62]. Also, Zeng et al. reported that CNF (Pyrograf-III^{TM}) in poly(methylmetacrylate) at concentrations no greater than 10 wt% exhibited a deterioration in flexibility, strength and ductility of 50, 20 and 35%, respectively [63]. Therefore, the maximization of the electrical properties of these materials is required, but such enhancement must be balanced against the deterioration of the mechanical properties.

1.3.3 Processing-structure-property relationships

Polymer nanocomposites are mainly made by three different routes. In solution blending, the nanomodifiers are mixed with a polymer-solvent solution, and the polymer composite is obtained after the solvent is evaporated [20]. For in-situ polymerization, the modifiers are segregated with a low viscosity medium, mixed with the monomer, and then synthesized [20]. In melt-compounding, a molten thermoplastic polymer is intensively mixed by shear and extensional forces with the nanomodifiers [20].

The first two routes often use different solvents, which in many cases are not environmentally friendly. Furthermore, the first route cannot be used with high molecular weight polyolefins which are practically insoluble in most organic solvents [20]. The third route is an economical way to produce nanocomposites and is also fast, continuous and scalable for industrial production.

Figure 1.12 is a schematic representation of how the microstructure, modifier dispersion and electrical network vary with the level of mixing energy applied to a composite at a constant modifier concentration. At low levels of mixing energy, the nanomodifiers form isolated clusters with no electrical inter-connection. As the mixing energy is increased, the shearing forces in the melt are able to partially rupture the clusters, aggregating some modifiers that initiate the electrical connection of clusters [64]. In this stage of dispersion level, the modifiers start to form an electrical network.

This process continues with mixing until a point where maximum network is reached, in which most modifiers are interconnected across the composite. Nonetheless, the dispersion level for this stage is still at an intermediate level. From this point of

maximum network, if more mixing energy is applied, the modifiers get more dispersed, to the point of being isolated from each other or even broken by excessive mixing that leads to reduced electrical connectivity [64]. Therefore, an optimization of the mixing conditions is desirable to maximize the electrical properties of the composites.

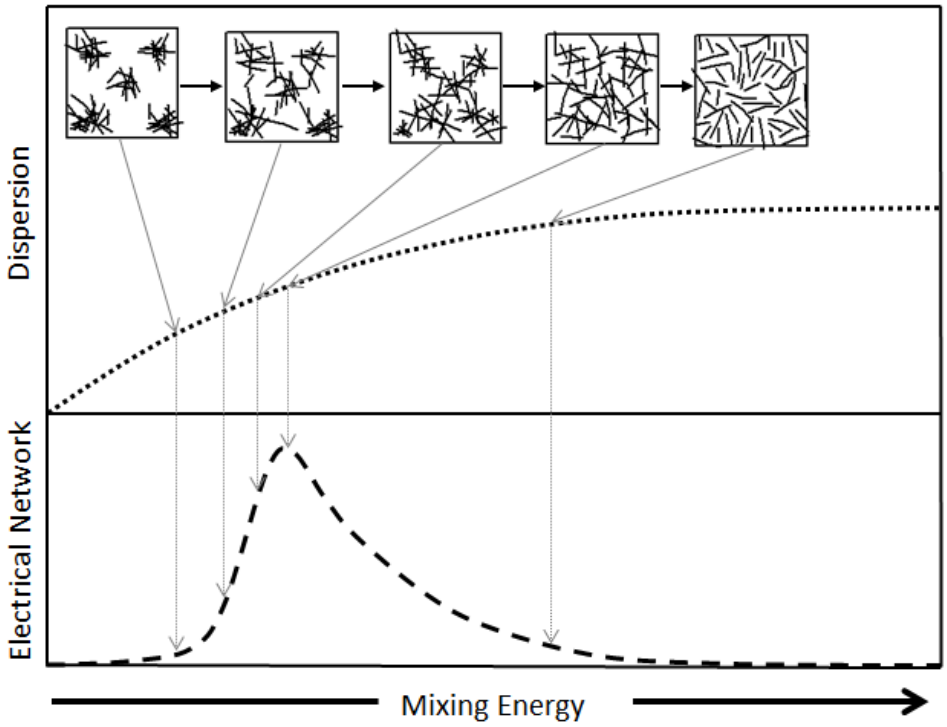

Figure 1.12. Schematic representation of the influence of the mixing energy on the microstructure, dispersion and electrical network for a composite of fixed concentration.

The energy of mixing basically depends on four parameters: (a) melt temperature; (b) mixing geometry; (c) mixing speed, with which energy of mixing scales with its second power; and (d) the mixing time, with which the energy of mixing keeps a proportional relationship [65].

Figures 1.13 and **1.14** respectively display the electrical resistivity and EM SE for CNF/HDPE composites at 7.5 vol% prepared by batch-mixing at different mixing speeds and mixing times [6]. It is worth noting that, for a given CNF concentration, high mixing times and mixing speeds increased the resistivity of the composites and reduced their EM SE. Thus, high mixing energy levels led to poor electrical networks, whereas softer mixing conditions produced good conductivity levels and shielding performance.

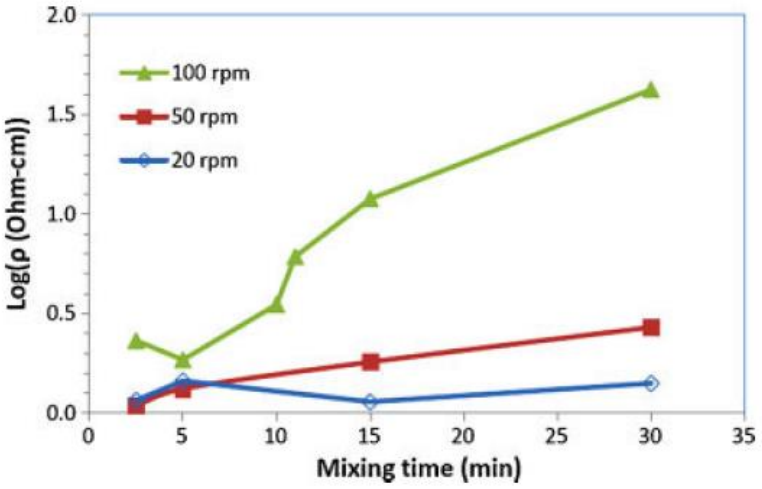

Figure 1.13. Effect of melt-mixing conditions on the electrical resistivity of CNF/HDPE composites at 7.5 vol%. Adapted from [6].

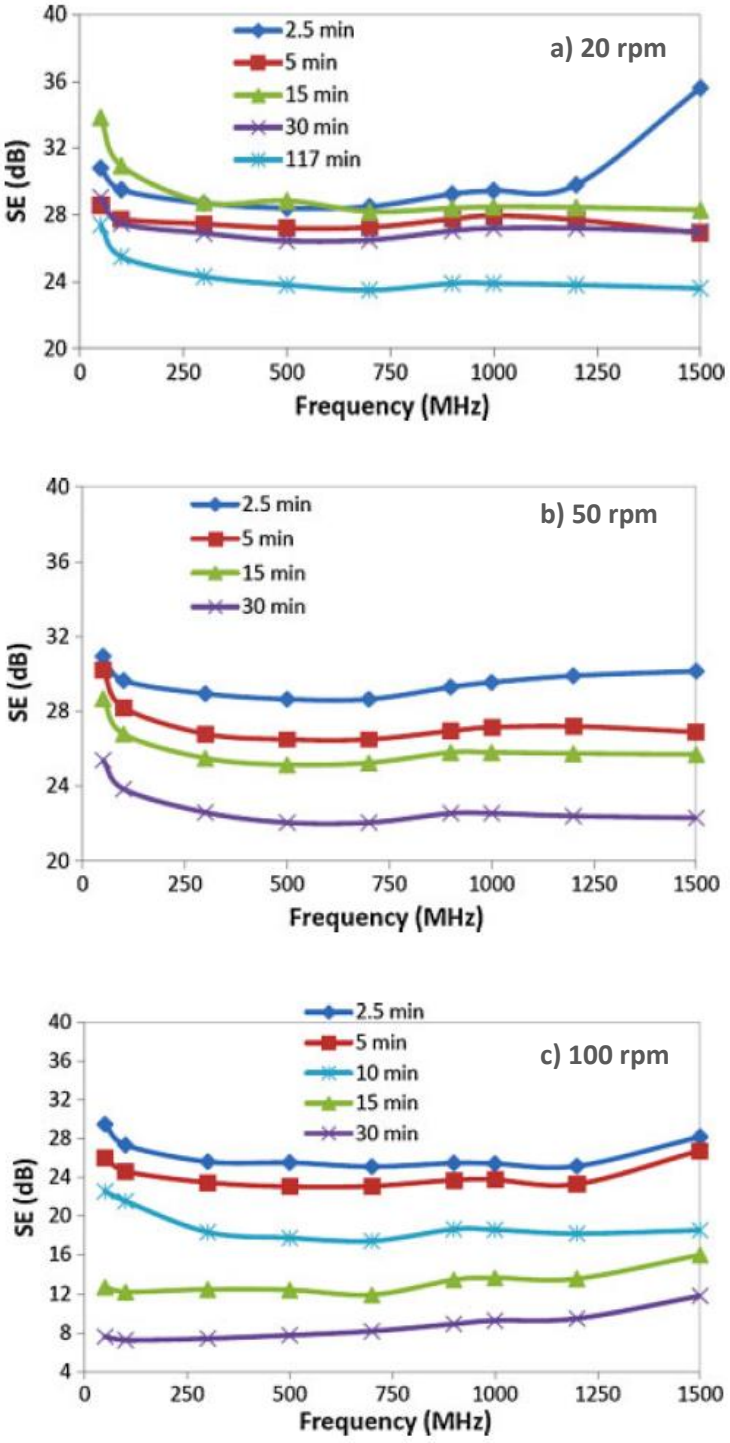

Figure 1.14. Effect of melt-mixing conditions on EM SE of CNF/HDPE composites at 7.5 vol% a) 20 rpm, b) 50 rpm, c) 100 rpm. Adapted from [6].

Different polymer processing techniques apply different levels of shear/elongational flow-fields to the modifiers, which results in a preferred orientation of the modifiers [66-68]. This preferred orientation leads to anisotropic properties of the composites [19, 55]. As shown in **Figure 1.15**, after increasing the injection speed from 8 to 30 cm^3/s, an increase of two orders of magnitude in the surface resistivity of the composites was found [19]. This change was attributed to the alignment gained by the CNTs due to the surface shearing during the injection [19]. In contrast, when the injection temperature was increased from 285 to 300°C a reduction of about 100 kΩ/sq was observed due to a more random distribution of the CNTs [19].

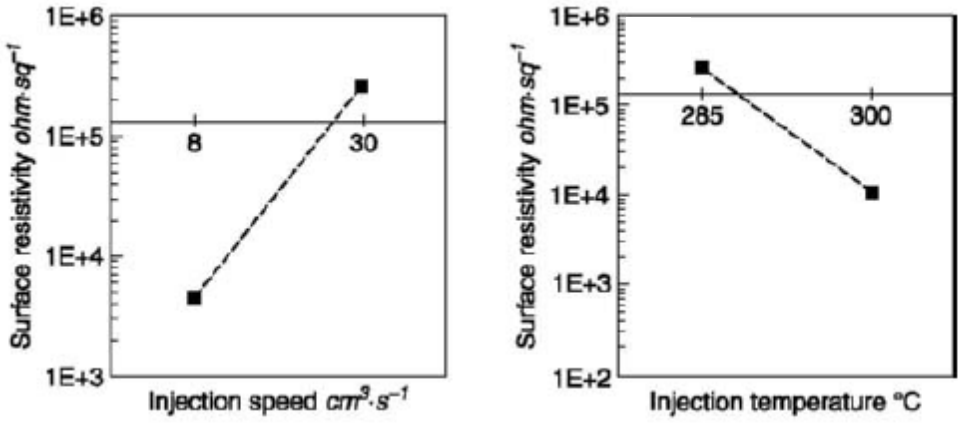

Figure 1.15. Effect of injection speed and injection temperature on the surface resistivity of injection-molded polycarbonate/CNT nanocomposites. Adapted from [19].

1.4 Electromagnetic and electrostatic shielding

1.4.1 Electromagnetic compatibility with polymer composites

The increasing miniaturization of electronic devices makes it necessary for diverse circuits to operate in close proximity to each other [69]. Frequently, these circuits/devices affect each other adversely due to electromagnetic, impedance or conductive coupling [69]. In computational and automation control systems, the mal-functioning caused by these forms of electromagnetic interference (EMI) might make the systems fail catastrophically [70]. Thus, the development and proper application of electromagnetic compatibility strategies that prevent coupling problems and minimize noise and electrostatic discharges has become a major focus for circuit designers [69].

Electromagnetic compatibility (EMC) is a field of engineering concerned with the operation and design of electrical/electronic systems in a manner that makes them immune to electromagnetic interference (EMI), and/or inoffensive to other susceptible devices [71]. This includes minimizing EMI generation at its source, reducing or eliminating coupling paths by proper circuit layout, shielding, filtering, and grounding practices for keeping the EMI emissions and discharges within specific limits to guaranty a safe operation [71, 72]. In these approaches, electromagnetic shielding effectiveness (EM SE) and electrostatic discharge (ESD) protection can be particularly important in EMC design.

Traditionally, these compatibility requirements have been met by using metals. However, in recent years, the utilization of multifunctional electrically conductive

materials such as hybrid structures and advanced composite materials for electromagnetic shielding has been demonstrated [17, 71, 72]. It is in this area of specialized compatibility applications, where novel conductive carbon nanomodifier/polymer nanocomposites have taken a role as potential substitutes for traditional metallic materials [10, 35, 71, 72].

Recently, several studies have been devoted to the study of the EM SE performance of conductive carbon-based polymer composites [6, 10, 11, 66, 73]. For instance, Arjmand et al. obtained EM SE values of about 25 dB in the X-band frequency range for 1.85-mm thick composites made of MWNT/polycarbonate composites at only 5 wt% [66]. For relatively low frequencies, Yang et al. reported EM SE values of 13, 16 and 21 dB at 1.5 GHz for composites (1.5-mm thick) made with PR-24 CNF in liquid crystal polymer for the concentrations of 5, 10 and 15 %, respectively [73]. Janda et al. reported values of 13 dB at 1 GHz for 3.2-mm thick composites made of carbon fibers and Nylon-6,6 at 40 wt% [11]. For polyolefin-based composites, Al-Saleh and Sundararaj reported EM SE values of about 30 dB in the 30 MHz-1.5 GHz frequency range for 2-mm thick composites consisting of graphitic carbon nanofibers and HDPE at 7.5 vol% [6]. They have also studied MWNT in isotactic PP, where EM SE values as high as 35 dB in the X-band were reported for 7.5 vol% and 1-mm thick samples [10].

1.4.2 Frequency bands

Different electronic devices are designed to operate at different frequencies of the radio spectrum. The operating frequencies of such devices will determine in many

regards the type of applications in which are utilized [74]. **Table 1.2** summarizes the different frequencies of the radio spectrum and their primary applications. Because of the broad range of frequencies, the microwave and radio engineers have created a nomenclature for the different radio frequencies, and have designated names to different bands [75]. **Figure 1.16** places such radio frequency nominations and bands designations into the electromagnetic spectrum. For digital devices, radio frequencies higher than 30 MHz are of interest [70]. Of particular relevance are frequencies up to 3 GHz that include the VHF and UHF bands in which many digital systems, TV and FM broadcasting, cell phones, radars and other systems operate [6, 70, 74].

Frequency is inversely related to wavelength [75]. Thus, a microwave with a frequency of 300 GHz will have a wavelength of only 1 mm, whereas some shortwave radio frequency can be as large as 100 m long [75]. The length-scale (physical size) of a device relative to the wavelength of the surrounding frequencies will determine in many cases its gain/performance and its functionality [75]. Thus, low-frequency devices require quite large elements, while high frequencies need relatively smaller ones. For instance, a half-wave dipole antenna will have a characteristic length associated with its wavelength. Thus, a small receiving antenna will work more efficiently at high frequencies [76].

Table 1.2. Individual bands of the radio spectrum and primary applications. Adapted from [74].

Band	Frequency	Applications
Extreme High Frequency (EHF)	30-300 GHz	Radar, advanced communication systems, remote sensing, radio astronomy
Super High Frequency (SHF)	3-30 GHz	Radar, satellite communication systems, aircraft navigation, radio astronomy, remote sensing
Ultra High Frequency (UHF)	300 MHz-3 GHz	TV broadcasting, radar, radio astronomy, microwave ovens, cellular telephones
Very High Frequency (VHF)	30-300 MHz	TV and FM broadcasting, mobile radio communications, air traffic control
Medium Frequency (MF)	300 kHz-3 MHz	AM broadcasting
Low Frequency (LF)	30-300 kHz	Radio beacons, weather broadcast stations for air navigation
Very Low Frequency (VLF)	3-30 kHz	Navigation and position location
Ultra Low Frequency (ULF)	300 Hz-3 kHz	Audio signals on telephone
Super Low Frequency (SLF)	30-300 Hz	Ionospheric sensing, electric power distribution, submarine communication
Extreme Low Frequency (ELF)	3-30 Hz	Detection of buried metal objects
	<3 Hz	Magnetotelluric sensing of the Earth' structure

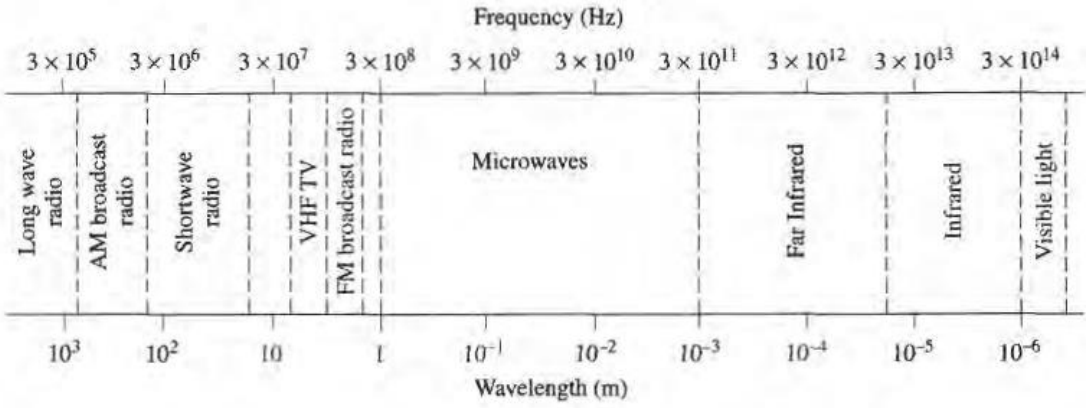

Typical Frequencies	
AM broadcast band	535–1605 kHz
Short wave radio band	3–30 MHz
FM broadcast band	88–108 MHz
VHF TV (2–4)	54–72 MHz
VHF TV (5–6)	76–88 MHz
UHF TV (7–13)	174–216 MHz
UHF TV (14–83)	470–890 MHz
US cellular telephone	824–849 MHz
	869–894 MHz
European GSM cellular	880–915 MHz
	925–960 MHz
GPS	1575.42 MHz
	1227.60 MHz
Microwave ovens	2.45 GHz
US DBS	11.7–12.5 GHz
US ISM bands	902–928 MHz
	2.400–2.484 GHz
	5.725–5.850 GHz
US UWB radio	3.1–10.6 GHz

Approximate Band Designations	
Medium frequency	300 kHz to 3 MHz
High frequency (HF)	3 MHz to 30 MHz
Very high frequency (VHF)	30 MHz to 300 MHz
Ultra high frequency (UHF)	300 MHz to 3 GHz
L band	1–2 GHz
S band	2–4 GHz
C band	4–8 GHz
X band	8–12 GHz
Ku band	12–18 GHz
K band	18–26 GHz
Ka band	26–40 GHz
U band	40–60 GHz
V band	50-75 GHz
E band	60-90 GHz
W band	75-110 GHz
F band	90-140 GHz

Figure 1.16. The electromagnetic spectrum. Adapted from [75]

1.4.3 Electromagnetic coupling problem

The process of generation, transmission, and reception of electromagnetic energy in electronic systems is depicted in **Figure 1.17** [70]. Here, the source (e.g., lightning, RF transmitters, high speed data trace, electric motors) emits electromagnetic energy, which is transferred through a coupling path (e.g., cables, antennas, ground), and received by another receptor (e.g., RF receivers, high speed data trace, integrated circuits, telephones). This process can be either intentional or unintentional. When this coupling process between two or more devices becomes unintentional, there is an electromagnetic compatibility problem [70]. This coupling process can be: a) either capacitive or inductive depending on whether the interfering field is the electric, *E*, or the magnetic, *H*; b) conductive, if electric currents are causing interference; or c) radiated, when electromagnetic waves are involved [69, 70]. Most cases are a combination of these processes.

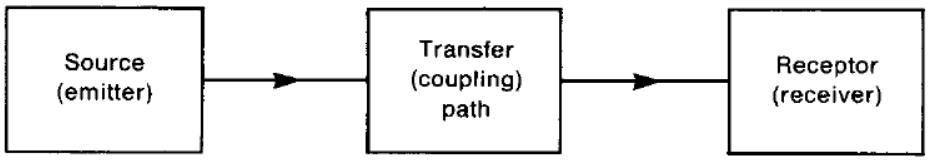

Figure 1.17. Basic decomposition of an EMC coupling process. Adapted from [70].

There are three approaches for preventing this undesired interference: a) suppression of the emission at the source, b) making the coupling path as inefficient as possible, and c) minimizing the susceptibility of the receptor [70]. The best approach is to

minimize the source, which is usually carried out by means of proper circuit design and layout [70]. The second approach, often used in addition to the first, consists of shielding and filtering strategies that reduce or change the characteristic of the coupling path. The third approach is difficult to achieve and can only be used in special cases [69, 70].

The emitted energy can be either conducted (wires) or radiated (wireless) depending on the coupling path type [70]. The current study is devoted to radiated emissions only. Thus, to turn the coupling path between the source and the receptor of radiating frequencies as inefficient as possible, shielding enclosures are necessary. **Figure 1.18** is an illustration of the two main purposes of a shield. For case (a), the radiation generated by a source of noise is contained inside the shield, preventing the external antenna receptor from receiving such noise. For case (b), a susceptible device is protected from the external radiation. In either case, the coupling path has been reduced by the shield [70].

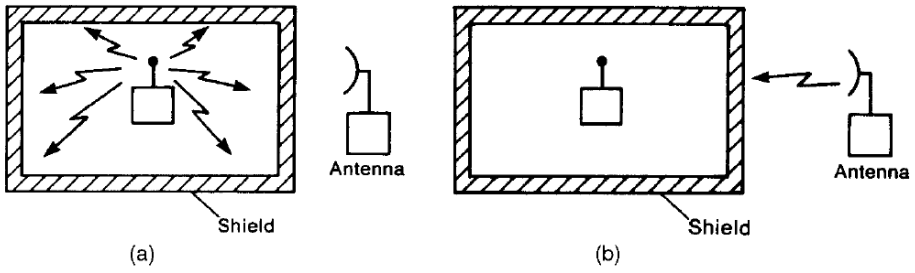

Figure 1.18. Illustration of the two purposes of a shield enclosure (a) contention of the field, and (b) exclusion of the field. Adapted from [70].

The characteristics of an electromagnetic wave depend on the source and the distance from the source [69]. The space around the source can be divided in two zones as shown in **Figure 1.19**. Near the source, the EM-field can be very complex and the ratio of the electric field to the magnetic field (i.e., the wave impedance, $\eta = E/H$) is determined by the characteristics of the source [69, 70]. At a distance greater than the angular wavelength, $\lambda/2\pi$, the wave impedance becomes constant and equals the characteristic impedance of the media in which it travels (in the vacuum or air $\eta_o = 120\pi\ \Omega$), and the electric and magnetic fields are orthogonal forming a plane-wave [69]. The type of waves dealt in this study will be of the far-field type.

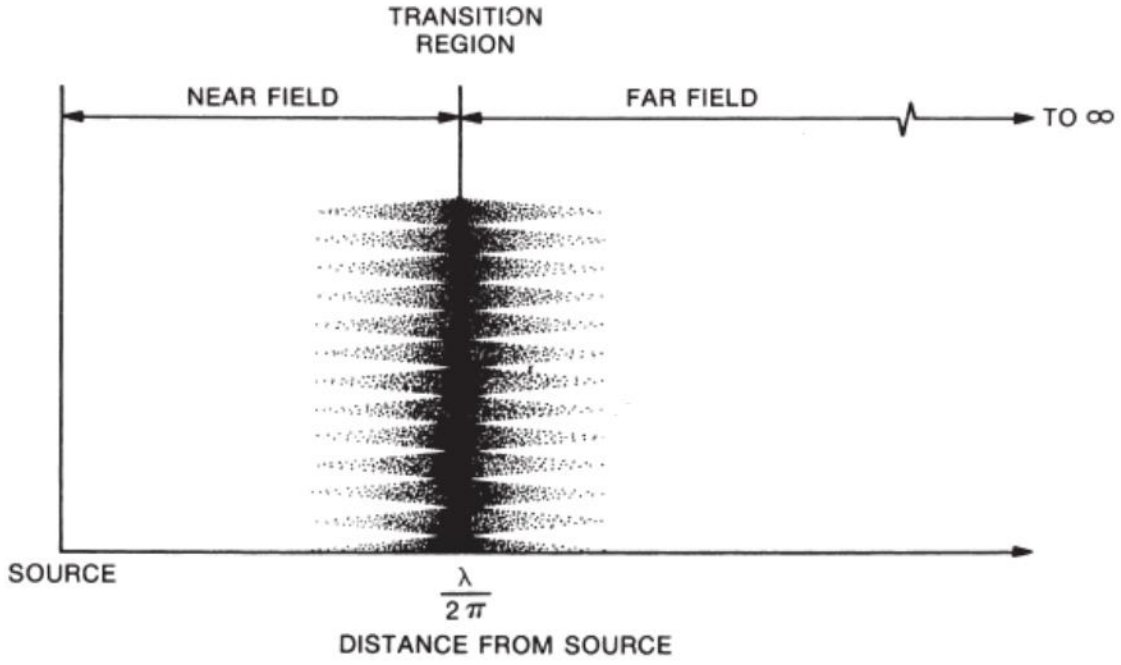

Figure 1.19. Near and far field zones of the surroundings of a source of electromagnetic radiation. Adapted from [69].

1.4.4 Shielding effectiveness

The shielding effectiveness (SE) of a barrier can be specified in terms of the reduction of either electric (E) or magnetic field strength (H) caused by the barrier [69]. As depicted in **Figure 1.20,** SE is defined as a logarithmic ratio (decibel) of the field measured at a given point with the shield, to that measured at the same point in the absence of the shield [69, 72]. Thus, the electric shielding effectiveness is defined as:

$$SE = -20 \log \left| \frac{E^{tr}}{E^{inc}} \right| \tag{1.1}$$

where, E^{tr} and E^{inc} are the electric fields measured with the materials present (transmitted) and without the material present (incident), respectively. The magnetic shielding effectiveness is similarly defined as:

$$SE = -20 \log \left| \frac{H^{tr}}{H^{inc}} \right| \tag{1.2}$$

The electromagnetic shielding effectiveness, which accounts for the attenuation of both fields, is analogously defined in terms of wave power, P, as:

$$SE = -10 \log \left| \frac{P^{tr}}{P^{inc}} \right| \tag{1.3}$$

For non-magnetic conductive materials, such as conductive carbon-based polymer composites, only electric shielding effectiveness is of interest. Moreover, if the incident field is a plane-wave and the intrinsic impedance of the material on both sides of the shield is the same (air in most cases), these three definitions can be interchangeably used. Nonetheless, the definitions in terms of electric field or power are the most standardized [70]. All shielding measurement methods are based on these basic definitions.

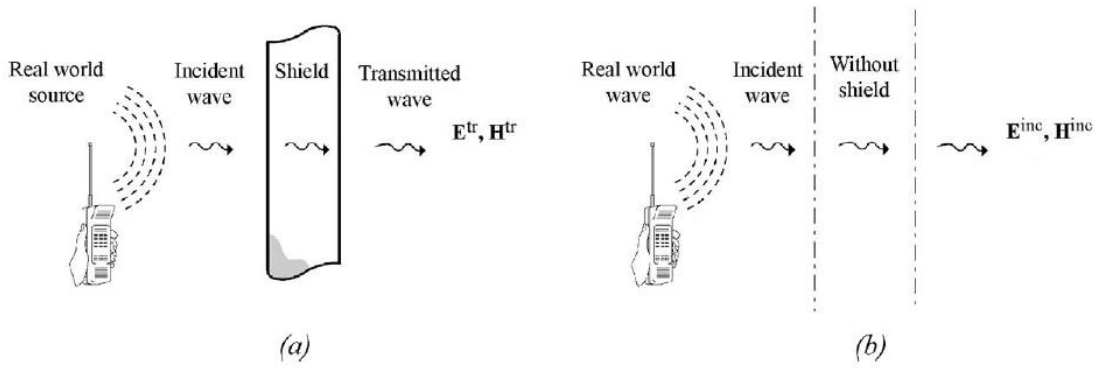

Figure 1.20. Representation of configuration (a) with the shield, and (b) without the shield for the evaluation of the shielding effectiveness. Adapted from [72].

1.4.5 Shielding mechanisms

Figure 1.21 is a schematic diagram of the interaction of the electric field of a plane-wave with a shield made of an electrically thin material, i.e., specimen thickness << skin-depth, which is typical of materials with low-to-intermediate conductivities [10, ASTM-D4935]. In this process, three basic shielding mechanisms can be identified: a) reflection of the incident wave at the first surface due to the change of wave impedance ($\eta \rightarrow \eta_o$), corresponding to reflection loss, E_{R_1}; b) absorption of the wave due to attenuation imparted by the lossy characteristics of the material along the material thickness, corresponding to absorption loss, E_{A_1}; and c) internal multiple reflections that undergo subsequent attenuations and transmissions at both surfaces, and contribute to the primary reflection, E_{R_1}, and transmission, E_{T_1}, at each side of the barrier.

For electrically thick materials (i.e., specimen thickness >> skin-depth, typical of highly conductive materials), the primary reflection loss, E_{R_1}, and absorption loss, E_{A_1},

greatly attenuate the amplitude of the field due to its highly lossy properties (i.e., conductivity, permittivity and permeability), and multiple reflections do not occur significantly [16, 55, 70].

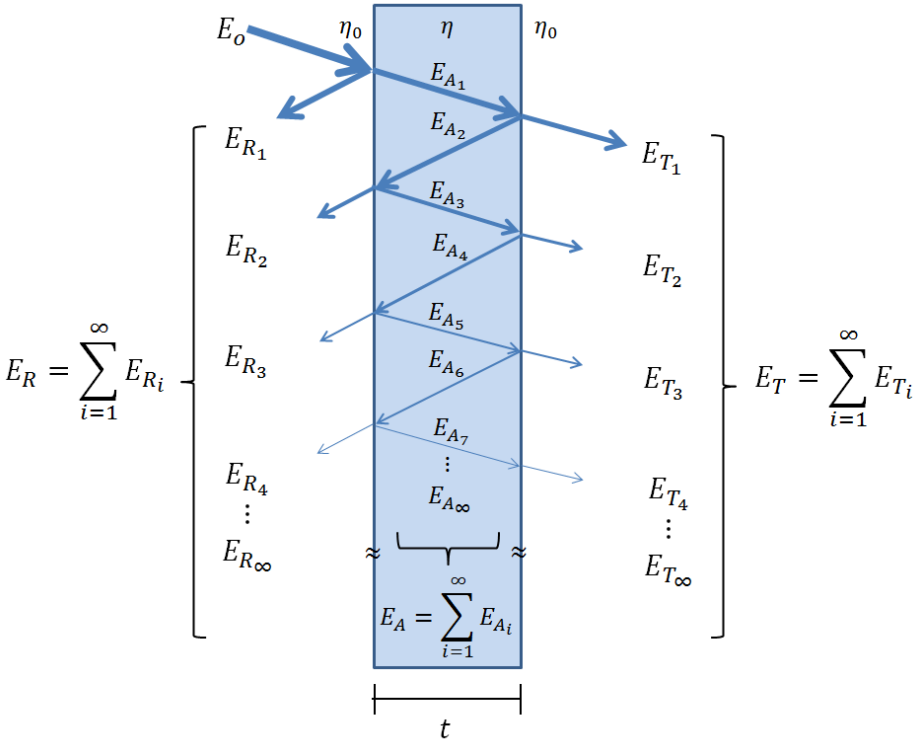

Figure 1.21. Shielding mechanisms undergone by an electromagnetic wave in an electrically thin material.

From the interaction of the field with the shield, three field components can be identified: the total reflected component, E_R; the total absorbed component, E_A; and the total transmission component, E_T [16]. Thus, the wave power balance ($P \propto E^2$) of these three components is [10, 55]:

$$P_o = P_R + P_A + P_T \tag{1.4}$$

Dividing (1.4) by the incident wave power, P_o, it yields:

$$1 = \frac{P_R}{P_o} + \frac{P_A}{P_o} + \frac{P_T}{P_o} = R + A + T \tag{1.5}$$

where, R, A and T are defined as reflectance, absorbance and transmittance, respectively. These will determine the reflective, absorptive and total shielding components, respectively [10, 55].

1.4.6 Electrostatic discharge (ESD)

Another important EMC technique is electrostatic discharge (ESD) protection, which deals with the safe dissipation of electrostatic charge. Electrostatic discharge (ESD) occurs due to the separation of charges in non-conductive materials and results in intense electric fields [70]. This difference in electrical potential will be equilibrated as soon as the charge finds a conductive path to leak to the ground, or "arc", when the voltage reaches the breakdown of the material [69]. If these transient discharges flow through the device itself, significant damage can occur for susceptible circuitry components [12, 72].

Metals are typically used for protecting devices from ESD. However, for charge dissipation, such high conductivity levels are usually not needed. **Table 1.3** displays a common classification of materials based on the bulk and surface resistivity ranges typically required for the different applications ranging from the shielding, conductive, static dissipation, antistatic to the purely insulative.

Table 1.3. Material classification based on surface and bulk resistivities. Adapted from [77].

Classification	Surface Resistivity	Bulk Resistivity
Shielding	0.01–1 Ω	< 10 Ω-m
Conductive	0–10^5 Ω	< 10^2 Ω-m
Static dissipative	10^5–10^9 Ω	10^2–10^9 Ω-m
Antistatic	10^9–10^{14} Ω	
Insulative	> 10^{14} Ω	

Thus, resistivities ranging from 10^2 to 10^9 Ω.m (10^{-9} to 10^{-2} S/m) are commonly required for electrostatic dissipation [12, 33, 77]. Because of this conductivity range for ESD, conductive compounds such aliphatic amines, quaternary ammonium salts, amides and deposited metals are frequently used in antistatic coatings, foams, bags and conductive boxes [79, 79]. Moreover, the commercialization of conductive polymer composites, with low fractions of conductive modifiers, has recently been taking relevance in this area as potential substitutes of these materials [17]. In recent Clemson studies, Lee et al. reported that LLDPE composites made with experimental CNF at only ~5 vol% (10^8 Ω·m) led to dissipate 99% of the applied charge in just 0.01 seconds [33].

1.4.7 EMC regulations

Typically, 20-30 dB of shielding is considered a good level of attenuation for polymer composites [35, 66]. However, the actual level of attenuation required for a

specific application will depend on regulatory requirements for permissible electromagnetic emissions. These levels establish limits in terms of electric field for commercial and industrial digital devices at different frequency levels [70]. A digital device is defined as an unintentional radiator that generates frequencies higher than 9 kHz and uses digital techniques in its circuitry [70].

In the United States, the Federal Communication Commission (FCC) is the agency in charge of regulating these limits [69, 70]. Outside the United States, the International Special Committee on Radio Interference (CISPR) is in charge. Most countries follow CISPR recommendations, and the most utilized standard is the CISPR 22, which is similar to that of FCC [70]. In this study, only the regulations for radiating devices are of interest.

Table 1.4 contains the radiating emission limits for Class B digital devices (i.e., devices for residential environment) as specified by FCC. The electric field limits are expressed in μV/m and dBμV/m (i.e., $\frac{\mathrm{dB\mu V}}{\mathrm{m}} = 20\log_{10}\left(\frac{\mathrm{V/m}}{1\mu\mathrm{V/m}}\right)$) [70]. Thus, to comply with these limits, the electric field must be no greater than 40 dBμV/m as measured at 3 m from the emitting device in a special shielded setup, known as semi-anechoic chamber. If during these measurements, a field of 60 dBμV/m is obtained, a shielding enclosure that provides at least 20 dB of EM SE would be required for the device to comply with the FCC limits.

Table 1.4. FCC emission limits for Class B digital devices at 3 m. Adapted from [69].

Frequency (MHz)	Field Strength (μV/m)	Field Strength (dB μV/m)
30–88	100	40.0
88–216	150	43.5
216–960	200	46.0
>960	500	54.0

The ESD regulations used most frequently are the Military Standards Mil-B-81705B and Mil-B-81705C [33, 80]. To qualify a material as ESD dissipative by this standard, 99% (1 % cut-off) of the initial induced charge must be dissipated is less than 2 seconds, or 90% (10 % cut-off) in less than 0.5 seconds.

1.4.8 EM SE characterization methodologies

As illustrated in **Figure 1.22**, radiated emissions measurements in digital devices are typically made in semi-anechoic chambers that simulate open-field conditions [70]. This consists of a shielded room with special radio-frequency absorbing cones that prevent external fields and internal reflections from interfering with those emitted by the tested device. A special detecting antenna is used to measure the field at such position [70].

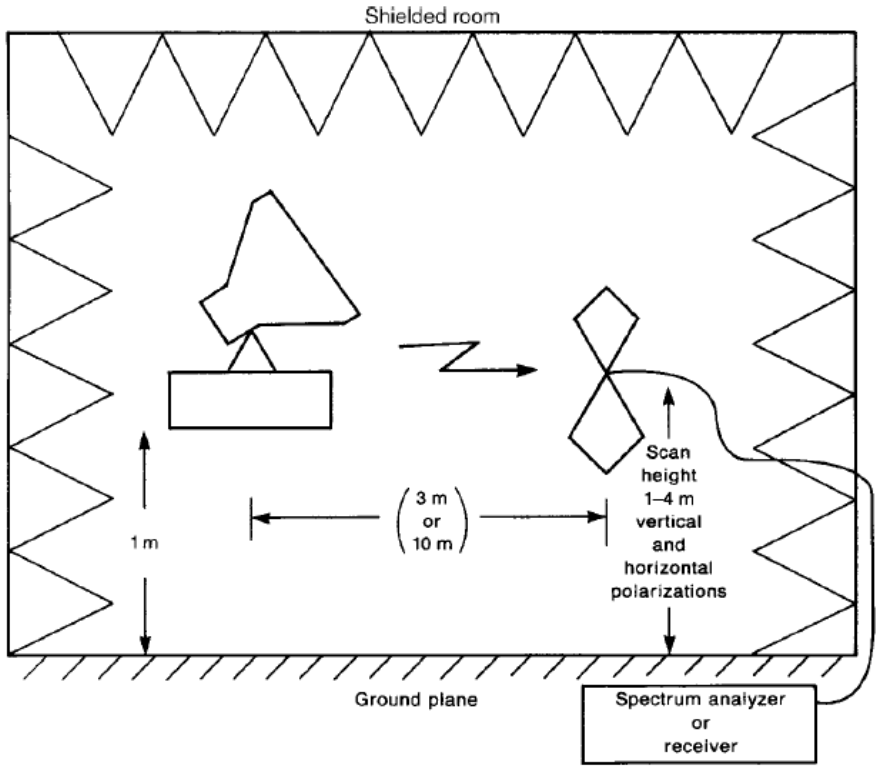

Figure 1.22. Illustration of a semi-anechoic chamber for measuring radiated emissions from digital devices. Adapted from [70].

The testing of materials (rather than devices) for shielding applications is made by slightly different approaches, and most methods are based on the MIL-STD-285 and MIL-G-83528 [71]. These can be highly elaborated methods that require large installations such as dual chambers and special antennas. One of these methods is shown in **Figure 1.23**, where two shielded chambers are separated by a relatively small perforation in which the sample is placed. An antenna emits the radiating frequencies in one chamber. The receipting antenna located in the second chamber receives the portion of the fields that is able to pass through the sample. The relative amount of attenuation of

the field obtained with the material present to that attained without the material is thus measured. Signal generators are used to generate the fields and amplifiers are connected to the transmitting antenna, whereas spectrum and network analyzers are commonly used for measuring the fields.

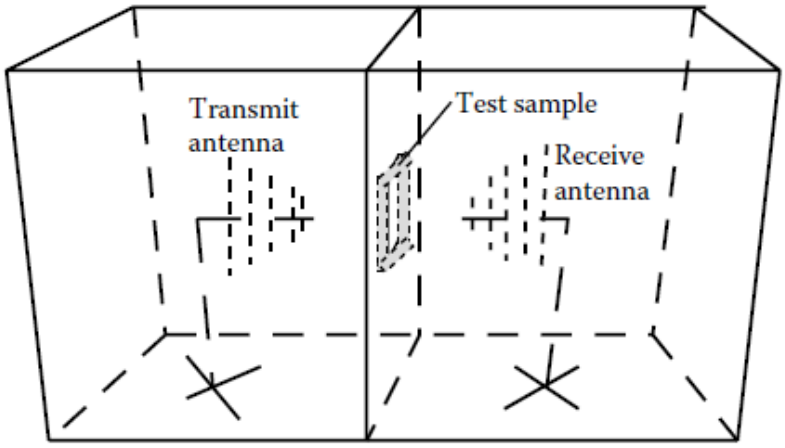

Figure 1.23. EM SE measurement according to Mil-STD-285. Adapted from [71].

Due to the large length-scale of the installations (< 4 m) required by MIL-STD-285, usually only frequencies greater than 500 MHz can be tested. Thus, slotted transmission lines with coaxial fixtures or special waveguides are alternatively used due to their wider frequency ranges, relatively lower cost, smaller physical size, and ease of assembly [6, 71, 81, ASTM D4935]. These methods also offer a good level of dynamic range (80-100 dB), a variety of wave propagation modes, and are based on standard tests methods such as ASTM D4935 [75, ASTM D4935]. They require shielding specimens of dimensions equal to those of the flange of the waveguides, thus smaller amounts of materials are required. Such specimens are inserted between the two halves of a split

transmission line, or placed into a slit in a continuous transmission line. The relative attenuation of the fields with and without the material is measured. **Figure 1.24** is a schematic of a split coaxial line, which is the type of methodology used throughout this study to assess the EM SE of the carbon-based nanocomposites hereby developed.

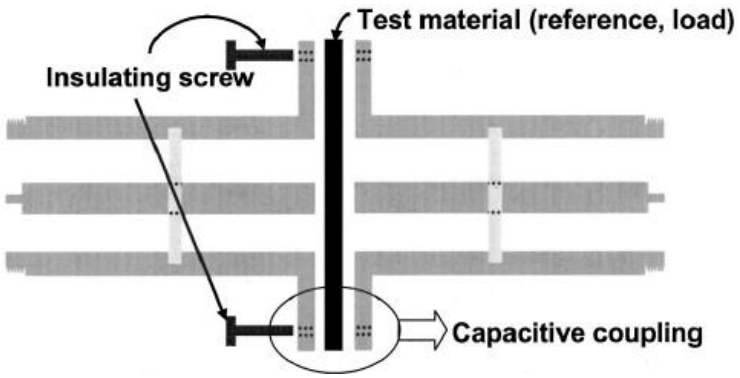

Figure 1.24. Split coaxial transmission line for EM SE measurements. Adapted from [81].

1.5 Objectives

The literature review indicates that a considerable effort has been devoted to the study of conductive carbon modifiers-based nanocomposites for enhanced electrical conductivity. However, the electromagnetic shielding effectiveness (EM SE) of composites consisting of carbon nanomodifiers with medium to high concentrations has not been thoroughly investigated. Therefore, the primary goal of this research was to investigate the electromagnetic shielding performance of nanocomposites consisting of graphitic carbon nanomodifiers and a ductile linear low density polyethylene (LLDPE). For this study three different heat-treated carbon nanomodifiers were included. The EM

SE was investigated in relation with the electrical and mechanical properties of the composites, which are directly influenced by the microstructure and electrical network formed by the modifiers in the polymeric matrix. Therefore, the specific objectives of this research were to:

1. investigate the effect of the level of graphitic crystallinity of carbon nanomodifiers on the electromagnetic shielding effectiveness of their LLDPE nanocomposites;
2. determine the role of morphology of different carbon modifiers on the electromagnetic shielding of their LLDPE nanocomposites;
3. model the influence of the composite electrical properties on the electromagnetic shielding of in-plane randomly oriented carbon nanomodifier-based nanocomposites with intermediate and high nanomodifier concentrations; and
4. investigate the influence of flow-induced carbon nanomodifier orientation on the electromagnetic shielding of polarized electromagnetic waves by the LLDPE nanocomposites.

The outline of the remaining dissertation is as follows:

Chapter 2 initially describes the effect of carbon nanofiber concentration on the conductivity of their LLDPE composites to determine the percolation threshold of this composite system. Next, it focuses on the influence of the level of graphitization of

carbon nanofibers on the electromagnetic shielding of their percolated nanocomposites. Highly graphitic CNFs, treated at temperatures greater than 2000°C, led to enhanced shielding in their composites. The results of this chapter have been published in reference [35].

Once the necessity of utilizing highly graphitic modifiers was established, the influence of different heat-treated carbon modifiers, with different morphologies (shapes and dimensions), on the electromagnetic shielding of composites prepared by a softer melt-mixing with LLDPE was studied in Chapter 3.

In Chapter 4, the effect of high nanomodifier concentrations on the electromagnetic shielding of their nanocomposites was investigated. In addition, a theoretical understanding of the role that the composite electrical properties play on the EM SE of in-plane randomly oriented nanocomposites was performed and compared to the experimental results. The results presented in this chapter have been published in reference [55].

Because nanomodifier orientation also affects the shielding performance of composites, flow-induced nanomodifier orientation was used to prepare composites with a preferred modifier orientation and anisotropic electrical conductivity. The EM SE performance of such oriented nanocomposites as analyzed by polarized electromagnetic waves was assessed and discussed in Chapter 5.

Finally, Chapter 6 summarizes the conclusions of this work, and provides recommendations for future studies.

1.6 References

1. Strong AB. Plastics, Materials and Processing. United States of America: Pearson Education Inc., 2006.

2. Mark JE. Physical Properties of Polymers Handbook. United States of America: Springer Science+Business Media, LLC, 2007.

3. Hull D. Clyne TW. An Introduction to Composite Materials. New Delhi: Cambridge University Press, 1996.

4. Chawla KK. Composite Materials, Science and Engineering. Germany: Spring-Verlag New York Inc., 1987.

5. Al-Saleh MH, Gelves GA, Sundararaj U. Copper nanowire/polystyrene nanocomposites: Lower percolation threshold and higher EMI shielding. Composites Part A 2011;42:92-97.

6. Al-Saleh MH, Sundararaj U. Electrically conductive carbon nanofiber/polyethylene composite: effect of melt mixing conditions. Polym Adv Technol 2011;22:246-253.

7. Gelves G, Lin B, Sundararaj U, Haber J. Low Electrical Percolation Threshold of Silver and Copper Nanowires in Polystyrene Composites. Adv Func Mater 2006;16:2423-2430.

8. Dani A, Ogale AA. Electrical Percolation Behavior of Short-fiber Composites: Experimental Characterization and Modeling. Compos Sci Technol 1996;56:911-920.

9. King JA, Morrison FA, Keith JM, Miller MG, Smith RC, Cruz M, Neuhalfen AM, Barton RL. Electrical Conductivity and Rheology of Carbon-Filled Liquid Crystal Composites. J App Polym Sci 2006;101:2680-2688.

10. Al-Saleh MH, Sundararaj U. Electromagnetic interference shielding mechanisms of CNT/polymer composites. Carbon 2009;47:1738-1746.

11. Janda NB, Keith JM, King JA, Perger WF, Oxby TJ. Shielding-Effectiveness Modeling of Carbon-Fiber/Nylon-6,6 Composites. J Appl Polym Sci 2005;96:62-69.

12. Pratt TH. Electrostatic Ignitions of Fires and Explosions. New York: American Institute of Chemical Engineers, 2000.

13. Gupta G, Yee H. EMI Shielding Effectiveness of Conductive Composites. SPE ANTEC 1991, 1991;566-570.

14. McNallyT, Potschke P. Polymer-carbon nanotube composites, Preparation, properties and applications, United Kingdom: Woodhead Publishing Limited, 2011.

15. Gupta RK, Kennel E, Kim K-J. Polymer Nanocomposites Handbook. United States of America: Taylor and Francis Group, LLC, 2010.

16. Nanni F, Valentini M. Electromagnetic properties of polymer-carbon nanotube composites. In: McNally T, Pötschke P, editors. Polymer-carbon nanotube composites, Preparation, properties and applications. Cambridge, UK: Woodhead Publishing, 2011, pp. 329-346.

17. Bal S, Samal SS. Carbon nanotube reinforced polymer composites–A state of the art. Bull Mater Sci. 2007;30:379-386.

18. Markets and Markets, http://www.marketsandmarkets.com/Market-Reports/advanced-functional-material-1221.html as viewed 20 August 2013.

19. Lew CY, Dewaghe C, Claes M. Injection moulding of polymer-carbon nanotube composites. In: McNally T, Pötschke P, editors. Polymer-carbon nanotube composites, Preparation, properties and applications. Cambridge, UK: Woodhead Publishing, 2011, pp. 155-192.

20. Kaminsky W. Polyolefin-carbon nanotube composite by in-situ polymerization. In: McNally T, Pötschke P, editors. Polymer-carbon nanotube composites, Preparation, properties and applications. Cambridge, UK: Woodhead Publishing, 2011, pp. 3-24.

21. Iijima S. Helical microtubules of graphitic carbon. Nature 1991;354:56-58.

22. Tomanek D, Enbody RJ. Science and Application of Nanotubes. New York: Kluwer Academic/Plenum Publishers, 2000.

23. Geckeler KE, Nishide H. Advanced Nanomaterials. Volume 1. Germany: Wiley-VCH, 2010.

24. Endo M, Iijima S, Dresselhaus MS. Carbon nanotubes. United States of America: Elsevier Science Ltd., Pergamon, 1996.

25. Tanaka K, Yamabe T, Fukui K. Science and Technology of Carbon Nanotubes. United Kingdom: Elsevier Science Ltd., 1999.

26. Harris PJF. Carbon Nanotube Science, Synthesis, Properties and Applications. United Kingdom: Cambridge University Press, 2009.

27. Burchell TD. Carbon Materials for Advanced Technologies. Netherlands: Elsevier Science Ltd., 1999.

28. Gogotsi Y. Nanotubes and Nanofibers. United States of America: Taylor and Francis Group LLC, CRC Press, 2006.

29. Koo JH. Polymer Nanocomposites. United States of America: The McGraw-Hill Companies, Inc., 2006.

30. Saito R, Dresselhaus G, Dresselhaus MS. Physical Properties of Carbon Nanotubes. London: Imperial College Press, 1998.

31. Léonard F. The Physics of Carbon Nanotube Devices. United States of America: William Andrew Inc., 2009.

32. Lee S, Kim T-R, Ogale AA, Kim M-S. Surface and structure modification of carbon nanofibers. Synth Met 2007;157:644-650.

33. Lee S, Kim M, Ogale AA. Influence of Carbon Nanofiber Structure on Properties of Linear Low Density Polyethylene Composites. Polym Eng Sci 2010;50:93-99.

34. Wang W, Yang K, Gaillard J, Bandaru PR, Rao AM. Rational Synthesis of Helically Coiled Carbon Nanowires and Nanotubes through the Use of Tin and Indium Catalysts. Adv Mater 2008;20:179–182.

35. Villacorta BS, Ogale AA, Hubing TH. Effect of Heat Treatment of Carbon Nanofibers on the Electromagnetic Shielding Effectiveness of Linear Low Density Polyethylene Nanocomposites. Polym Eng Sci 2013;53:417-423.

36. He BB, Two-Dimensional X-Ray Diffraction. United States of America: John Wiley & Sons, Inc., 2009.

37. Amer MS. Raman Spectroscopy for Soft Matter Applications. United States of America: John Wiley & Sons, Inc., 2009.

38. Lee S. Effect of Carbon Nanofibers on the Microstructure and Properties of Polymer Nanocomposites. PhD dissertation, Clemson University, 2007.

39. Lee S, Dab S-Y, Ogale AA, Kimb M-S. Effect of heat treatment of carbon nanofibers on polypropylene nanocomposites. J Phys Chem Solids 2008;69:1407–1410.

40. Lee S, Ogale AA. Microstructure of Carbon Nanofiber/Thermotropic Liquid Crystalline Polymer Composites. J App Polym Sci 2009;113:2872–2880.

41. Singjai P, Changsarn S, Thongtem S. Electrical resistivity of bulk multi-walled carbon nanotubes synthesized by an infusion chemical vapor deposition method. Mater Sci Eng A 2007;443:42-46.

42. Yang K. Inter-Tube Bonding and Defects in Carbon Nanotubes and the Impact on the Transport Properties and Micro-Morphology. PhD Dissertation, Clemson University, 2009.

43. Yi W, Lu L, Zhang DL, Pan ZW, Xie SS. Linear specific heat of carbon nanotubes. Phys Rev B 1999;59:R9015.

44. Hone J, Whitney M, Piskoti C, Zettl A. Thermal conductivity of single-walled carbon nanotubes. Phys Rev B 1999;59:4.

45. Salvetat J-P, Bonard J-M, Thomson NH, Kulik AJ, Forró L., Benoit W, Zuppiroli L. Mechanical properties of carbon nanotubes. Appl Phys A 1999;69:255–260.

46. Daraio C, Nesterenko VF, Jin S. Impact response by a foamlike forest of coiled carbon nanotubes. J App Phys 2006;100:064309.

47. Al-Saleh MH, Sundararaj U. Review of the mechanical properties of carbon nanofiber/polymer composites. Composites Part A 2011;42:2126–2142.

48. Naito K, Tanaka Y, Yang J-M, Kagawa Y. Tensile properties of ultrahigh strength PAN-based, ultrahigh modulus pitch-based and high ductility pitch-based carbon fibers. Carbon 2008;46:189-195.

49. Nobile MR. Rheology of polymer-carbon nanotube composite melts. In: McNally T, Pötschke P, editors. Polymer-carbon nanotube composites, Preparation, properties and applications. Cambridge, UK: Woodhead Publishing, 2011, pp. 428-481.

50. Mahmoodi M, Arjmand M, Sundararaj U, Park S. The electrical conductivity and electromagnetic interference shielding of injection molded multi-walled carbon nanotube/polystyrene composites. Carbon 2012;50:1455-1464.

51. Das NC, Chaki TK, Khastgir D, Chakraborty A. Electromagnetic Interference Shielding Effectiveness of Conductive Carbon Black and Carbon Fiber-Filled Composites based on Rubber and Rubber Blends. Adv Polym Tecnol 2001;20:226-236.

52. Gupta A, Choudhary V. Electrical conductivity and shielding effectiveness of poly(trimethylene terephthalate)/multiwalledcarbon nanotubes composites. J Mater Sci 2011;46:6416-6423.

53. Ramo S, Whinnery JH, Van Duzer T. Fields and Waves in Communication Electronics. United States of America: John Wiley & Sons, Inc., 1984.

54. Kasap SO. Principles of electronic materials and devices, New York: McGraw-Hill, 2002.

55. Villacorta BS, Hubing TH, Ogale AA. Influence of Composite Electrical Properties on the VHF-UHF Electromagnetic Shielding Characteristics of Polyolefin-Carbon Nanoparticle Composites. Compos Sci Tecnol, DOI: 10.1016/j.compscitech.2013.10.003.

56. Advani SG. Processing and Properties of Nanocomposites. United States of America: World Scientific Publishing Co. Pte. Ltd., 2007.

57. Moore AL, Cummings AT, Jensen JM, Shi L, Koo JH. Thermal Conductivity Measurements of Nylon11-Carbon Nanofiber Composites. J Heat Transfer 2009;131:091602-1.

58. Agarwal S, Khan MMK, Gupta RK. Thermal conductivity of polymer nanocomposites made with carbon nanofibers. Polym Eng Sci 2008;48:2474-2481.

59. King JA, Johnson BA, Via MD, Ciarkowski CJ. Effects of carbon fillers in thermally conductive polypropylene based resins. Polym Compos 2010;31:497-506.

60. Xiao KQ, Zhang LC, Zarudi I. Mechanical and rheological properties of carbon nanotube-reinforced polyethylene composites. Compos Sci Technol 2007;67:177-182.

61. Goh SH. Mechanical properties of polymer-polymer-grafted carbon nanotube composites. In: McNally T, Pötschke P, editors. Polymer-carbon nanotube composites, Preparation, properties and applications. Cambridge, UK: Woodhead Publishing, 2011, pp. 347-375.

62. Morcon M, Simon G. Polyolefin-carbon nanotube composites. In: McNally T, Pötschke P, editors. Polymer-carbon nanotube composites, Preparation, properties and applications. Cambridge, UK: Woodhead Publishing, 2011, pp. 511-544.

63. Zeng J, Saltysiak B, Johnson WB, Schiraldi DA, Kumar S. Processing and properties of poly(methylmetacrylate)/carbon nanofiber composites. Composites Part B 2004;35:245-9.

64. Kasaliwal G, Villmow T, Pegel S, Pötschke P. Influence of material and processing parameters on carbon nanotube dispersion in polymer melts. In: McNally T, Pötschke P, editors. Polymer-carbon nanotube composites, Preparation, properties and applications. Cambridge, UK: Woodhead Publishing, 2011, pp. 92-132.

65. Tadmor Z, Gogos CG. Principles of Polymer Processing. United States of America: John Wiley & Sons, Inc., 1979.

66. Arjmand M, Mahmoodi M, Gelves GA, Park S, Sundararaj U. Electrical and electromagnetic interference shielding properties of flow-induced oriented carbon nanotubes in polycarbonate. Carbon 2011;49:3430-3440.

67. Abbasi S, Carreau PJ, Derdouri A. Flow induced orientation of multiwalled carbon nanotubes in polycarbonate nanocomposites: Rheology, conductivity and mechanical properties. Polymer 2010;51:922-935.

68. Kuringer R.J., Alam MK, Anderson DP, Jacobsen RL. Processing and Characterization of aligned vapor grown carbon fiber reinforced polypropylene. Composites Part A 2002;33:53-62.

69. Ott HW. Electromagnetic Compatibility Engineering. United States of America: John Wiley & Sons, Inc., 2009.

70. Paul CR. Introduction to electromagnetic compatibility. United States of America: John Wiley & Sons, Inc., 1992.

71. Tong XC. Advanced Materials and Design for Electromagnetic Interference Shielding. United States of America: Taylor & Francis Group, LLC, 2009.

72. Celozzi S, Araneo R, Lovat G. Electromagnetic Shielding. United States of America: John Wiley & Sons, Inc., 2008.

73. Yang S, Lozano K, Lomeli A, Foltz HD, Jones R. Electromagnetic interference shielding effectiveness of carbon nanofiber/LCP composites. Composites Part A: Appl Sci Manuf 2005;36(5):691-697.

74. Ulaby FT. Fundamentals of Applied Electromagnetics. United States of America: Prentice Hall, Inc., 2001.

75. Pozar DM. Microwave Engineering. United States of America: Addison-Wesley Publishing Company, Inc., 1990, 2005.

76. Brown RG, Sharpe RA, Hughes WL, Post RE. Lines, waves, and antennas. The Transmission of Electric Energy. New York: The Ronald Press Company, 1973.

77. Kaiser KL. Electrostatic Discharge. United States of America: Taylor & Francis Group LLC, 2006.

78. Cooper G, Langer G, Rosinski J. Submicron Aerosol Losses in Aluminum Mylar Bags. J App Meteor 1979;18:57-68.

79. Wegrzynska J, Chlebicki J. Preparation, Surface-Active and Antielectrostatic Properties of Multiple Quaternary Ammonium Salts. J Surfact Deterg 2006;9:221-226.

80. Danni AA. Experimental Characterization and Modeling of Electrical Percolation Phenomenon in Short Fiber Composites. PhD Dissertation, Clemson University, 1995.

81. Hong YK, Lee CY, Jeong CK, Lee DE, Kim K, Joo J. Method and apparatus to measure electromagnetic interference shielding efficiency and its shielding characteristics in broadband frequencies. Rev Scient Instr 2003;74:2.

CHAPTER 2

EFFECT OF GRAPHITIC CRYSTALLINITY OF CARBON NANOFIBERS ON THE ELECTROMAGNETIC SHIELDING EFFECTIVENESS OF LINEAR LOW DENSITY POLYETHYLENE NANOCOMPOSITES

2.1 Introduction

As reviewed in various literature studies cited in Chapter 1, research on conductive carbon-based polymer composites for electromagnetic shielding is of topical interest [1-18], including nanocomposites obtained from carbon nanomodifiers [4, 5, 9, and 12]. Nanoforms such as carbon nanofibers (CNF) [10, 11, 13, 19, 20] may offer a size advantage to polymeric nanocomposite films because of their very small diameter (<0.5 μm), high aspect ratio and good electrical and mechanical properties when compared with traditional carbon fibers [7, 15, 19, 21, 22].

For most carbon nanoforms, impurities such as amorphous carbon and catalysts generated during the production processes decrease their transport and mechanical properties as compared with their crystalline state [23-25]. Therefore, post-process chemical treatments are often carried out. Studies on nanocomposites made with purified CNF and amorphous polymers have been previously reported [23]; such nanocomposites possessed a strain-to-failure of less than 5%. In this chapter a linear low-density polyethylene (semicrystalline) matrix with a large strain-to-failure for potential use in ductile/flexible nanocomposite applications was investigated.

Specifically, the effect of ultra-high temperature heat treatment (2500°C) of CNFs on their graphitic crystallinity is reported in relation to the electrical properties and the electromagnetic shielding effectiveness of such nanofibers in a LLDPE matrix. Relative contributions from different shielding components were also assessed for the nanocomposites. The results of this chapter have been published as "Effect of Heat Treatment of Carbon Nanofibers on the Electromagnetic Shielding Effectiveness of Linear Low Density Polyethylene Nanocomposites" [26].

2.2 Experimental

2.2.1 Materials

Carbon nanofibers, Pyrograf® III PR-19 (Applied Science Inc.), were used as electrical modifiers. Such CNFs are made by chemical vapor deposition (CVD) from natural gas as precursor by using a Fe-sulfide catalyst at about 900 ºC and have a diameter of 148±60 nm, and lengths ranging from 10 to 100 μm [20, 25].The matrix polymer was Poly(ethylene-co-1-octene), Dowlex^{TM} 2045 (Dow Chemical), a film grade linear low density polyethylene (LLDPE). It has a density of 0.920 g/cm^3, DSC melting point of 122ºC, and melt flow index of 1 g/10 min (190°C/2.16 kg, ASTM D1238).

2.2.2 Processing

A DSM Xplore 15 cc twin-screw micro-compounder (DSM) was used to prepare ~10 vol% (20 wt%) nanocomposites for as-received PR-19 CNF at 190°C and 20 rpm for 2 min in a co-rotating mode. One hour of ultra-high thermal treatment at 2500°C was carried out for PR-19 CNF in a Thermal Technology HP50-7010 furnace in helium atmosphere prior to compounding [24]. After heat treatment, PR-19 HT CNF were also compounded with LLDPE at 10 vol% (~20 wt%), following the same procedure as that used for untreated CNF-based nanocomposites. Such nanocomposites were processed by thermal compaction into circular sheets about 2.5 mm thick and 133 mm diameter utilizing a Carver laboratory press. Four replicates were made and tested for each composite type (i.e., n = 4). The influence of melt-mixing on the EM SE of composites consisting of 10 vol% PR-19 HT CNF in LLDPE matrix is documented in Appendix A. Finally, for assessing the thickness effect on the EM SE of the PR-19 HT nanocomposites at 10 vol%, 133-mm diameter samples were produced in two additional thicknesses: 0.25 mm and 0.75 mm. Three replicates (n = 3) were prepared and tested for each thickness.

2.2.3 Characterization

Raman spectroscopy was conducted for the CNFs to analyze the disordered (D) and graphitic (G) bands observed in carbon materials at 1315 cm^{-1} and 1580 cm^{-1}, respectively. A Renishaw micro-Raman spectroscope equipped with a 785 nm wavelength diode laser was used. The WiRE software, (version 3.2), was used to analyze

and integrate the peaks to determine the I_D/I_G Raman ratio [25]. Wide-angle X-ray diffraction (Rigaku-MSC, Houston, TX) was also conducted on the CNFs before and after the heat treatment using Cu target Kα radiation with a wavelength of 1.5406 Å [25]. The spectra were analyzed using Polar software version 2.6.7 from Stonybrook Technology and Applied Research (STAR). The X-ray source was operated at 45 kV and 0.65 mA, and the sample exposure time was 1 hour.

The bulk electrical resistivity (BER) of the CNF themselves, before and after heat treatment, was measured using a Keithley 196 System digital multi-meter (DMM) while compressing the CNFs at 50 MPa in an insulating fixture. The bulk electrical resistivity of the CNFs was computed from the measured resistance and sample geometry while being pressurized [27]. The DC volume electrical conductivity, σ (S/m), of the nanocomposites was measured using a Keithley 6517B High Resistance Meter connected to a Keithley 8009 Resistivity Test Fixture (ASTM D257). The alternating polarity method was performed by means of the Keithley 6524 software. The relative humidity and temperature of the experimental area were monitored using a 6517-RH humidity probe and a 6517-TP thermocouple, respectively. For the very conductive nanocomposites (i.e., $\sigma > 10^{-1}$ S/m), the conductivity was obtained from resistance measurements of sample specimens that were 12.5 mm wide, 2.5 mm thick and with lengths of about 25 mm, using a Keithley 196 System DMM. Silver paint was applied on the surfaces at each end of the samples and their resistance was measured. From the sample geometry and the resistance measurements, the conductivity was computed from four replicates (n = 4).

The static decay time was measured using an Electro-Tech Systems, Inc. 406D Static-Decay Meter that complies with the Federal Test Method 101D, Method 4046 and Military Standard Mil-B-81705C. This standard requires that 99% of the initial induced charge be dissipated is less than 2 seconds for qualifying material per Mil-B-81705C. The Static-Decay Meter was calibrated by the ESD Testing Laboratory of Electro-Tech Systems, Inc. (Glenside PA) prior to the measurements. Details on ESD measurements are documented in Appendix B.

The complex electrical permittivity (real ε' and imaginary ε'') of the nanocomposites, in their sheet form (2.5 mm thick), was measured utilizing an Agilent 4291B RF Impedance/Material Analyzer and an Agilent 16453A Dielectric Material Test Fixture. Prior to the measurements, the analyzer was calibrated utilizing an Agilent calibration kit (short (0 Ω), open (0 S), load (50 Ω)). Short/open/load fixture compensation was also applied to increase the accuracy of the measurements. The analysis frequency range was 30 MHz to 1.5 GHz. Details about permittivity measurements are also documented in Appendix B.

An Electro-Metrics EM-2107A coaxial transmission line test fixture was used to apply a far-field electromagnetic wave to the nanocomposite specimens (ASTM D4935). The electromagnetic shielding effectiveness (EM SE) was determined from the logarithmic ratio of the measured transmitted power with the material present, $P_{T,W}$, to the transmitted power without the material present, $P_{T,WO}$, which is represented with the reference specimen [ASTM D4935, 21]:

$$EM\ SE\ = -10 \log \frac{P_{T,W}}{P_{T,WO}} \quad (2.1)$$

The calibrated unit has a dynamic range greater than 80 dB. The accuracy of the calibration was checked by measuring a set of Mylar®-gold composite standard specimens. The EM-2107A test fixture was connected through coaxial cables to an Agilent Technologies N5230A PNA Series Network Analyzer that was calibrated with a 85033D 3.5 mm calibration kit. For measuring EM SE, each circular nanocomposite specimen was aligned between the test fixtures and measured at frequencies from 30 MHz to 1.5 GHz. The sample diameter was 133 mm, and four replicates were tested for each nanocomposite type. EM SE measurements details are documented in Appendix B.

Finally, the dispersion level of the nanomodifiers within the LLDPE matrix was assessed by inspection of the cross-section of the cryo-fracturated nanocomposites (Hitachi S-4800, SEM). For each type of nanocomposite, four different macroscopic locations were investigated by SEM. For each location, five different spots (micro-scale) were imaged. Representative SEM micrographs are presented in **Figure 2.1**. From approximately forty SEM micrographs thus obtained, not even one major cluster was positively identified in any of the micrographs. Thus, it is believed that these twin-screw extruded nanocomposites possess acceptable level of dispersion and distribution of CNFs, which may result from the fact that both LLDPE and CNFs are hydrophobic entities.

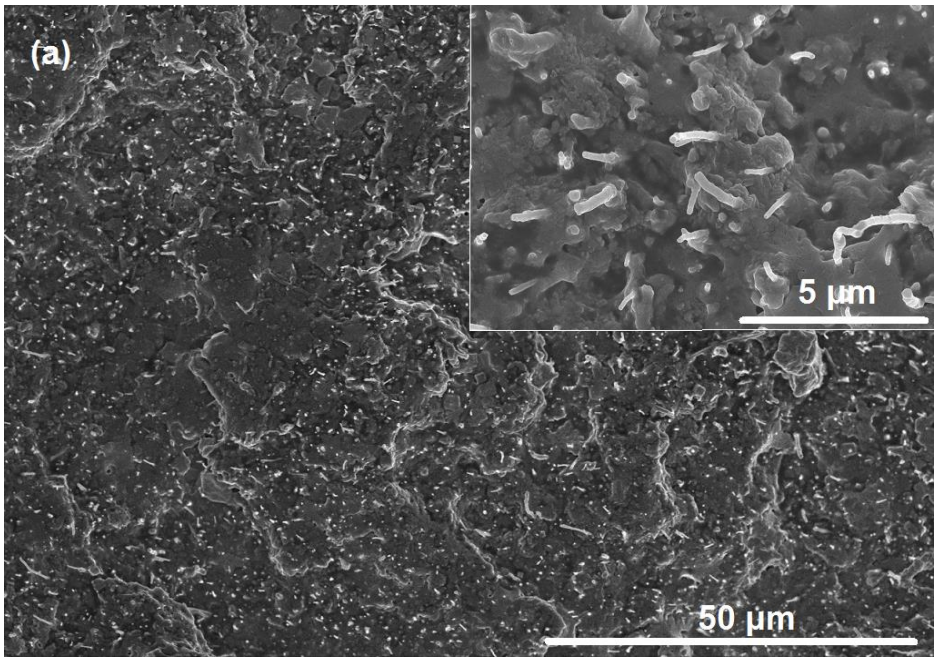

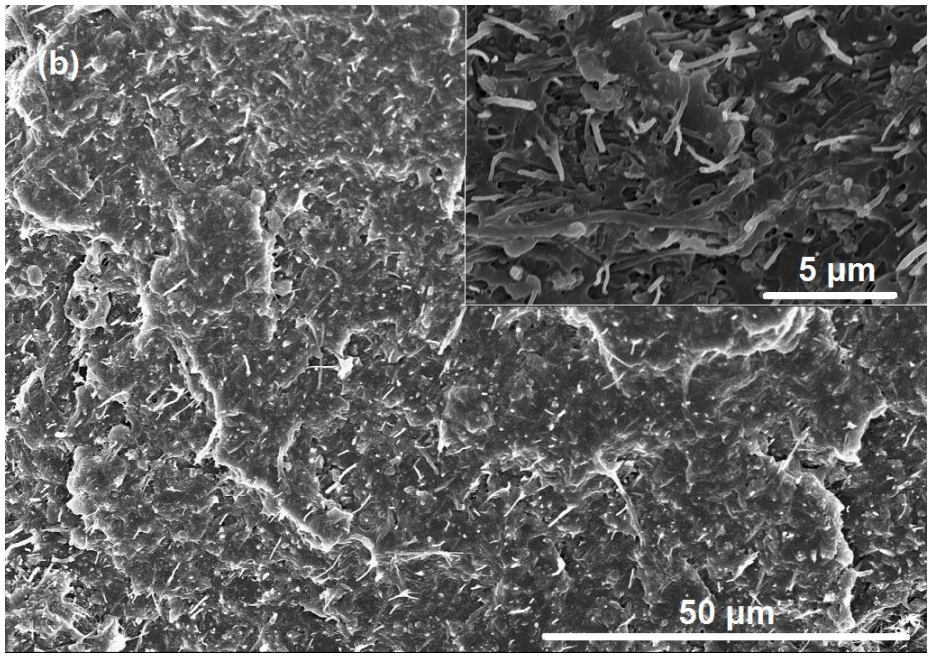

Figure 2.1. Scanning electron micrographs (SEM) of nanocomposites at 10 vol%: (a) untreated PR-19, and (b) heat-treated PR-19. Insets display the microstructure at higher magnification.

2.3 Results and Discussion

2.3.1 Carbon nanofibers: heat treatment and properties

The I_D/I_G Raman ratio of carbonaceous materials is directly related to their graphitic disorder or "defects". Hence, their I_D/I_G Raman ratio is inversely related to its level of graphitic crystallinity, which in turn controls its transport properties such as its intrinsic electrical and thermal conductivity [24, 25]. Representative Raman spectra for CNF are displayed in **Figure 2.2**. As-received PR-19 CNF displayed an I_D/I_G Raman ratio of 4.06±0.07, whereas the PR-19 HT CNF had an I_D/I_G Raman ratio of only 0.96±0.04 (replicates n = 8 in both cases). Thus, after heat treatment, PR-19 underwent a significant reduction in its I_D/I_G Raman ratio, as result of its improved graphitic structure.

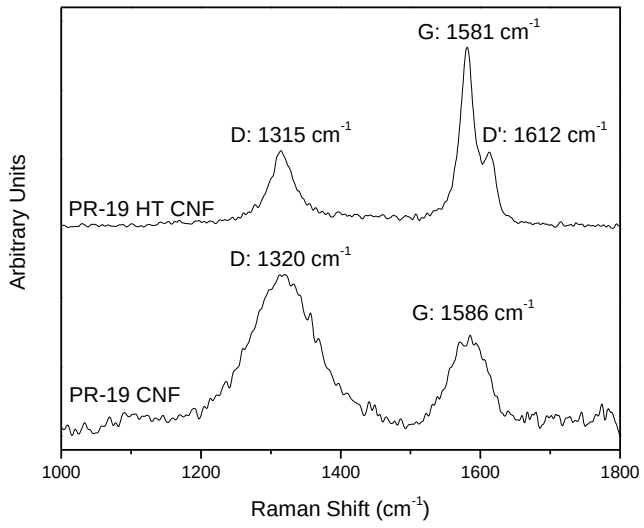

Figure 2.2. Raman spectra of untreated (PR-19) and heat-treated (PR-19 HT) carbon nanofibers.

Wide-angle X-ray diffraction was carried out for the as-received and heat-treated PR-19 CNF. Prior to the analyses, a silicon standard powder for X-ray diffraction (Standard Reference Material® 640d from the National Institute of Standards & Technology) was mixed with the CNF to assure the accuracy in locating the 2θ peak angle for the (002) graphene interlayer spacing. Representative X-ray diffractograms of the CNF are displayed in **Figure 2.3**. The heat treatment not only increased the intensity of the (002) peak for the PR-19 HT CNF, but also increased the 2θ angles from 26.0º for as-received PR-19 to 26.2º for heat-treated PR-19 [24]. From these values of 2θ, the graphitic interlayer spacing (d_{002}), which is related to the graphitic crystallinity of the CNF, was calculated using Bragg's law. The as-received and heat-treated PR-19 showed interplanar d_{002} spacing of 0.3424 nm and 0.3397 nm, respectively. Using the d_{002} value of 0.3440 nm for turbostratic carbon and 0.3354 nm for perfect graphite the graphitization level of the as-received and heat-treated PR-19 CNFs was 18% and 50%, respectively. These results are consistent with the I_D/I_G Raman ratios previously discussed [20, 24].

The intrinsic transport properties of the CNFs were assessed, particularly its bulk electrical resistivity (BER) was measured at 50 MPa compaction pressure. As-received PR-19 CNF showed a bulk resistivity of 2.0±0.2 Ω·cm (n = 6), whereas the PR-19 HT CNF had a BER of only 0.03±0.01 Ω·cm (n = 6 in both cases) at 50 MPa, which means an enhancement in their bulk electrical conductivity of about two orders of magnitude upon heat treatment [20]. This is consistent with the Raman spectroscopy and X-ray diffraction results conducted for the CNFs.

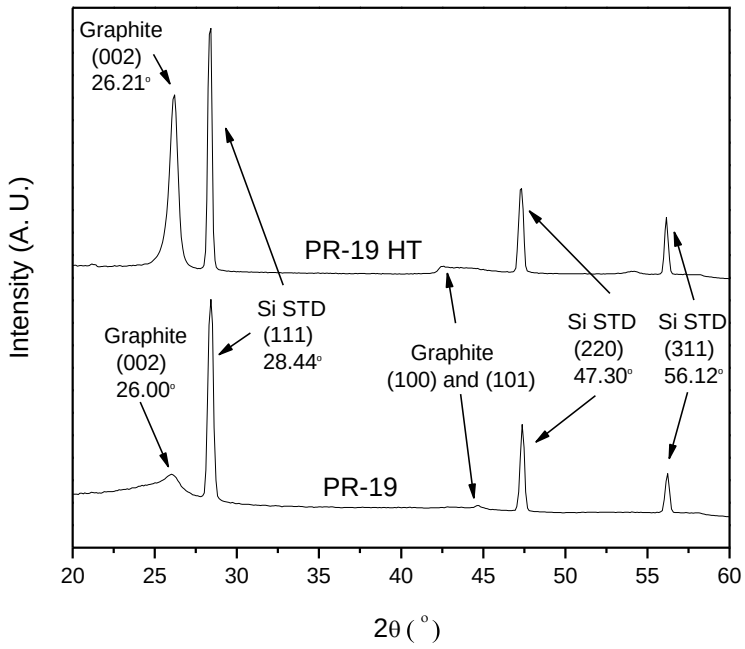

Figure 2.3. Wide angle X-ray diffractograms of untreated (PR-19) and heat-treated (PR-19 HT) carbon nanofibers. A small quantity of NIST-calibration grade silicon was added to the samples for accurate determination of 2θ angles of various peaks.

2.3.2 Nanocomposites

The DC electrical conductivity σ (i.e., the inverse of the DC electrical resistivity $\sigma = {}^{1}/_{\rho}$) of the nanocomposites was measured at ~25 °C and ~50 % relative humidity. Initial results, displayed in **Figure 2.4**, showed that the conductivity of untreated PR-19 nanocomposites at a concentration of 3 vol% was $3.8 \pm 1.5 \times 10^{-14}$ S/m (n

= 4). After increasing this concentration to 10 vol% (i.e. by half order of magnitude), untreated PR-19 nanocomposites crossed the percolation threshold (ϕ_c ~8 vol%). They displayed a conductivity of $4.4\pm0.7x10^{-9}$ S/m (n = 4) (compared with $7.0\pm1.1x10^{-15}$ S/m for pure LLDPE), and retained a great deal of the tensile properties of the pure resin, as shown in our previous work [19]. However, for the untreated PR-19 nanocomposites, even at fully percolated concentrations as high as 25 vol% (40 wt%), the conductivity only reached $6.5\pm3.0x10^{-5}$ S/m. In contrast, at only 3 vol%, the heat-treated PR-19 HT nanocomposites displayed a conductivity of $6.5\pm0.4x10^{-4}$ S/m (n = 4), which is an order of magnitude higher than that of the very-highly loaded untreated PR-19 nanocomposites at 25 vol%. Consequently, nanocomposites were prepared at only 10 vol% of PR-19 HT, which turned out to be in the fully percolated regime and retained tensile properties similar to those of the untreated PR-19 nanocomposites (10 vol%). At 10 vol%, PR-19 HT nanocomposites displayed a conductivity of $1.0\pm0.1x10^{1}$ S/m as compared to $4.4\pm0.7x10^{-9}$ S/m (n = 4) for their untreated counterparts. This means that the heat treatment provided an improvement in the conductivity of the nanocomposites of about ten orders of magnitude. The electrostatic discharge (ESD) characteristic of the nanocomposites was also measured. Both, PR-19 and PR-19 HT nanocomposites at 10 vol% were ESD dissipative and complied with the Mil-B-81705C requirements.

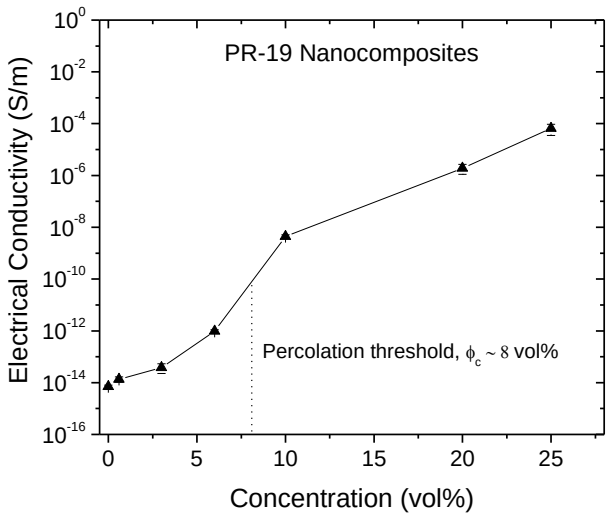

Figure 2.4. Concentration dependence of electrical conductivity of nanocomposites prepared with as-received PR-19 carbon nanofibers.

The complex electrical permittivity ($\varepsilon = \varepsilon' - j\varepsilon''$), as measured with the Agilent 16453A Dielectric Material Test Fixture, is displayed in **Figure 2.5** as a function of frequency for the untreated and heat-treated CNF nanocomposites. $\varepsilon'/\varepsilon_0$ represents the dimensionless real relative permittivity or dielectric energy storage, and $\varepsilon''/\varepsilon_0$ the dimensionless imaginary relative permittivity or polarization loss. The permittivity of the vacuum ε_0, is 8.85418x10^{-12} F/m. For the heat-treated PR-19 HT nanocomposites, the real and imaginary permittivity tend to decrease with frequency, whereas for the untreated CNF nanocomposites, both quantities are fairly frequency independent. The PR-19 HT nanocomposites exhibited an overall permittivity of (228±43)-(239±13)j at

100 MHz, decreasing to (3±2)-(11±6)j at 1.5 GHz (n = 4 in both cases). On the other hand, the untreated PR-19 nanocomposites displayed a permittivity of (13±2)-(0.5±0.1)j at 100 MHz, and their magnitude remained practically unchanged up to 1.5 GHz (at (12±1)-(0.5±0.1)j, (n = 4). These results establish that the heat treatment not only enhanced the capacitive behavior of the nanocomposites, but also increased the lossy component (i.e., $\varepsilon''/\varepsilon_0$). This is important, since $\varepsilon''/\varepsilon_0$ along with the DC conductivity σ, contributes to the electromagnetic absorption component of a material's shielding effectiveness [13].

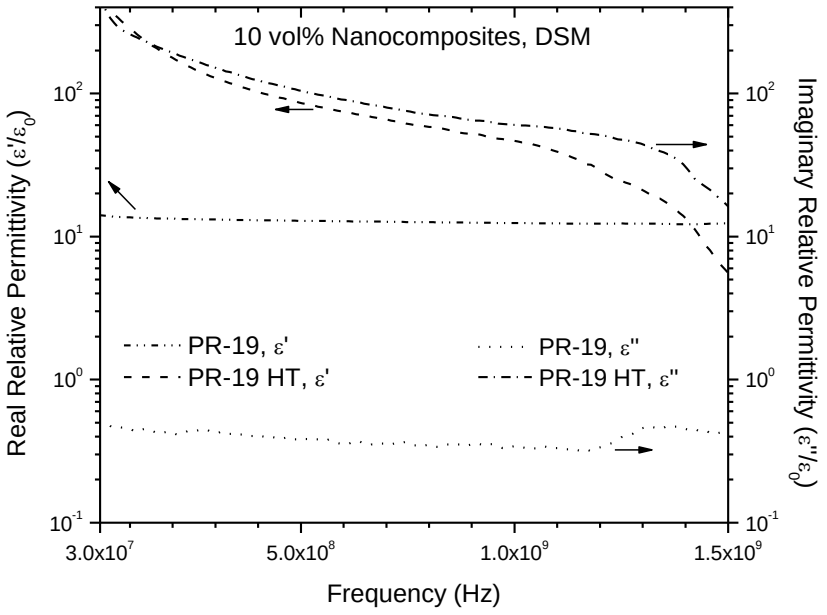

Figure 2.5. Complex relative electrical permittivity of representative PR-19 and PR-19 HT nanocomposites at 20 wt% (10 vol%) CNFs over a frequency range of 30 MHz to 1.5 GHz.

2.3.3 Electromagnetic shielding effectiveness (EM SE)

The EM SE of PR-19 HT and untreated PR-19 nanocomposites measured using the ASTM D4935 test procedure is displayed in **Figure 2.6**. The error bars in **Figure 2.6** represent the 95% confidence intervals obtained from the statistical analysis of four replicates. Untreated PR-19 nanocomposites at 10 vol% (20 wt%) displayed an EM SE of only 1±0.2 dB, whereas the EM SE of PR-19 HT nanocomposites was 14±2 dB (n = 4 in both cases). Thus, the heat treatment of the CNF improved the EM SE of the nanocomposites by about 13 dB. This increase in EM SE corresponds to an increase in electrical conductivity of ten orders of magnitude (10^{1} vs. 10^{-9} S/m). The EM SE enhancement is accompanied by an increase in permittivity from (13±2)-(0.5±0.1)j, n = 4, to (228±43)-(239±13)j, n = 4, at 100 MHz. This is 18 times the polarization and almost 500 times greater polarization loss. In contrast to these results, conventional P-55 pitch-based short carbon fiber-LLDPE composites (2.5 mm thick), prepared at the same processing conditions, equipment and loading level, showed only 3 dB of total shielding for the same frequency range, as shown in our previous work [19]. These results are consistent with those reported in the literature [22] for short-carbon fiber/PE composites, prepared by batch mixing (for 5 min) at a similar volume fraction (20 wt%, 2.5 mm thick), which displayed a shielding effectiveness of only 4 dB in the S, C, X and Ku frequency bands (i.e., 2-18 GHz).

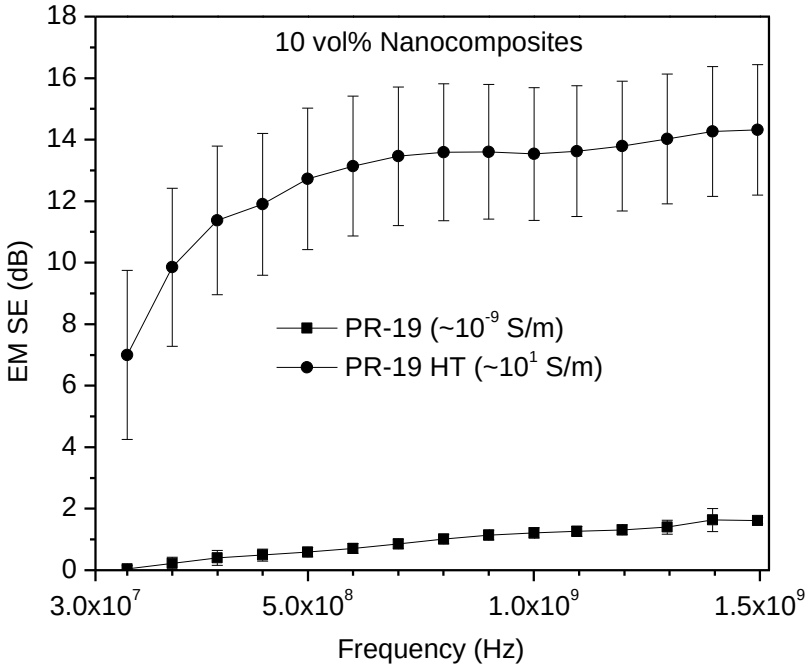

Figure 2.6. Electromagnetic shielding effectiveness (EM SE) of CNF-LLDPE nanocomposites over a frequency range of 30 MHz to 1.5 GHz. Nanocomposites were obtained from untreated (PR-19) and heat-treated (PR-19HT) carbon nanofibers at 20 wt% (10 vol%); error bars represent 95% confidence intervals.

The shielding ability of a homogeneous material is a function of its intrinsic impedance η. For an EM plane wave, η is the ratio of the magnitude of the electric field to that of the magnetic field that passes through the material [1]. The electrical conductivity σ, electrical permittivity ε, and magnetic permeability μ, are related to the intrinsic impedance as [1]:

$$\eta = \sqrt{\frac{\mu}{\varepsilon - \frac{\sigma}{\omega} j}} \tag{2.2}$$

where, ω is the angular frequency of the radiation (rad/sec).

For non-magnetic conductive materials (i.e., $\mu = \mu_0 = 4\pi \text{ x } 10^{-7}$ H/m and $\sigma \gg \omega\varepsilon$), the intrinsic impedance η of such materials is primarily dependent on the DC electrical conductivity σ [1]. Hence, the electrical conductivity is of paramount importance for attaining high values of EM SE. However, at high frequencies and low conductivities, the overall "polarizability" of the material is better expressed as a complex electrical permittivity, which not only accounts for the dielectric storage, but also for the losses at high frequencies due to the phase lag between the applied electric field and the matrix-CNF interfacial dipole moments with respect to the frequency variation ω [2, 13]. Thus, in nanocomposites, whose conductivity is not high compared to pure metals (i.e., ~10^6-10^7 S/m), the polarization loss ε'' also plays a role in determining the EM SE, primarily in the absorptive component of shielding. This can be viewed as another entropic effect to be added to that of the DC conductivity ($\varepsilon'' + \sigma/\omega$) [2].

2.3.4 Shielding mechanisms

To determine the shielding components for the nanocomposites, the scattering parameters, S_{21}, and, S_{11}, were measured and corrected with the reference specimens as detailed in Appendix B. They respectively define transmittance, T, and reflectance, R [28]:

$$T = \left|\frac{P_T}{P_0}\right| = |S_{21}|^2 \tag{2.3}$$

$$R = \left|\frac{P_R}{P_0}\right| = |S_{11}|^2 \tag{2.4}$$

The total shielding effectiveness (dB) and reflective shielding effectiveness (dB) were obtained as [3]:

$$EM\ SE\ = -10 \log T \tag{2.5}$$

$$EM\ SE_R = -10 \log (1 - R) \tag{2.6}$$

The absorptive shielding effectiveness can then be computed from their difference as:

$$EM\ SE_A = EM\ SE - EM\ SE_R \tag{2.7}$$

The absorptive and reflective shielding components for representative nanocomposites are shown in **Figure 2.7**. For PR-19 nanocomposites, the EM SE increases with frequency and reflection appears to be the dominant mechanism. In PR-19 HT nanocomposites absorption ($EM\ SE_A$) is the predominant component. In addition, both components are less sensitive to frequency for PR-19 HT nanocomposites than those of untreated nanocomposites. The absorptive component of shielding $EM\ SE_A$ depends on the entropic or "lossy" properties of the nanocomposites (i.e., $EM\ SE_A = f(\sigma, \varepsilon'')$) [2]. Thus, as the heat treatment increased the DC electrical conductivity, σ, and polarization loss, ε'', of the nanocomposites, the absorptive component also improved.

In applications where external radiation must be kept from interfering with an electronic circuit, the overall shielding provided by the enclosure is of importance, regardless of the mechanism. In contrast, when an electronic circuit couples to other circuits in the same enclosure, an absorptive shielded enclosure is preferred. Reflective enclosures can cause large fields to build up internally, which can enhance unwanted coupling between circuits inside the enclosure. These results indicate that PR-19 HT nanocomposites are suitable materials for applications where absorptive shielding is required over the VHF and UHF frequency bands.

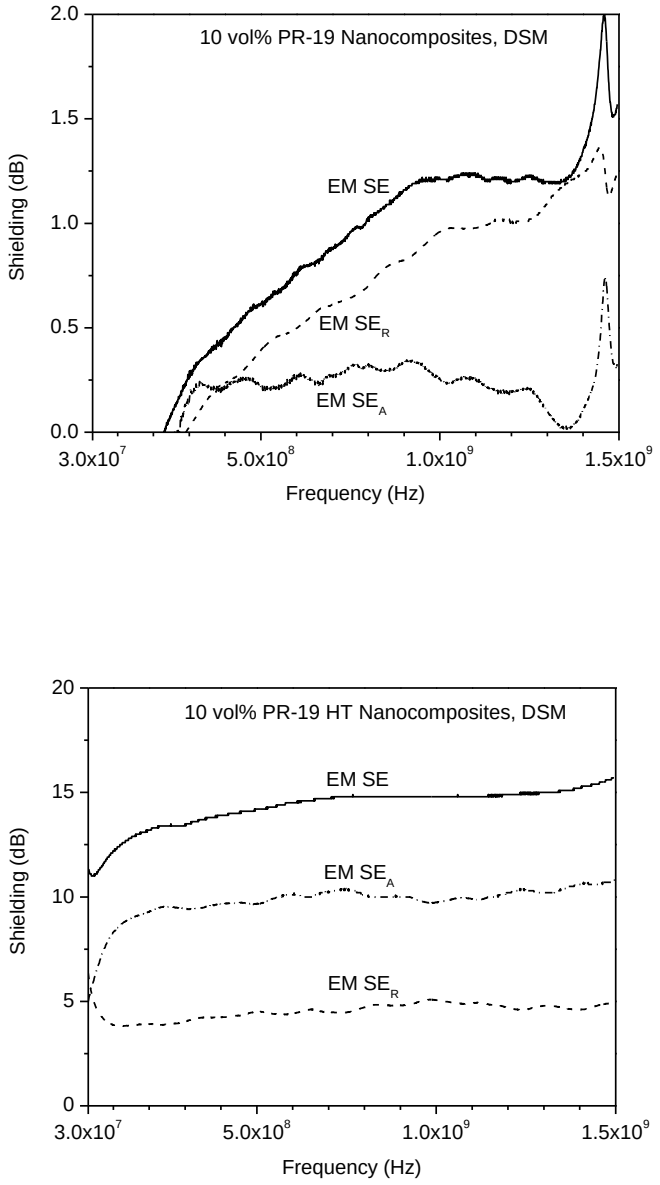

Figure 2.7. Representative spectra of total shielding effectiveness (EM SE) and reflective component (EM SE_R) over a frequency range of 30 MHz to 1.5 GHz for (a) PR-19 and (b) PR-19 HT nanocomposites at 20 wt% (10 vol%). The difference (EM SE_A) represents the absorption component.

The effect of sample thickness on the EM SE of PR-19 HT nanocomposites was assessed at 10 vol% CNFs (three replicates per thickness, n = 3). The measurements were conducted on sample thicknesses ranging from 0.25 to 2.5 mm (representing one order of magnitude difference) with an intermediate thickness of 0.75 mm. **Figure 2.8** indicates that, at 1.5 GHz, the EM SE is directly proportional to the sample thickness t, which would be expected for any homogeneous (or at least pseudo-homogeneous) material when the absorption component dominates. The reflective component of shielding can be estimated from the intercept of the linear regression of the EM SE and sample thickness data. The intercept of 4.3 dB is consistent with the experimentally measured $EM\ SE_{R\ @1.5\ GHz}$ of 4.9 dB displayed in **Figure 2.7**. These results are likely due to the microstructural uniformity of the nanocomposites from the perspective of EM SE properties.

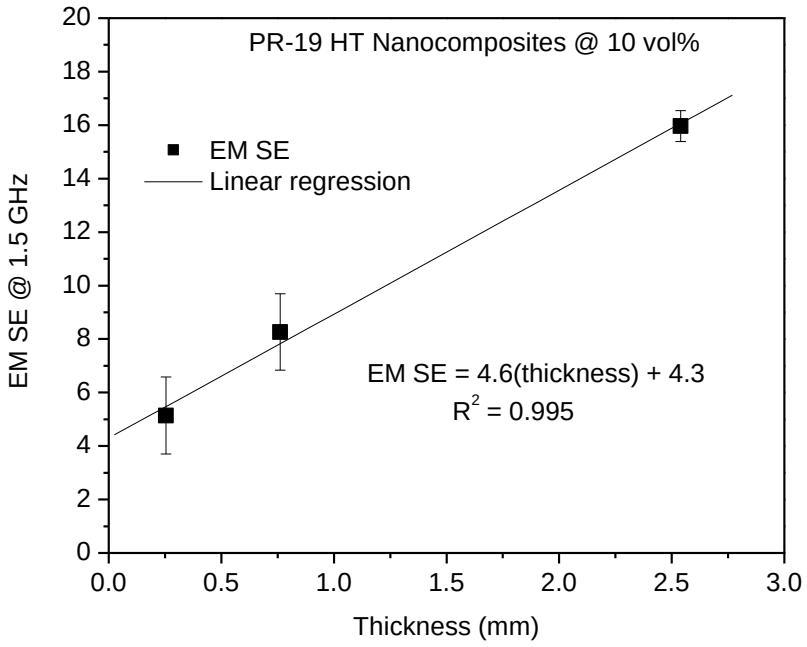

Figure 2.8. Effect of sample thickness on the EM SE of PR-19 HT nanocomposites at 10 vol% (20 wt%). Error bars represent 95% confidence intervals and the straight line represents linear least-squares regression fit.

Finally, the effect of solid nanomodifiers on the tensile properties of the resulting composites was assessed using the ASTM D638 Type V technique (die-cut, dogbone-shaped specimens of 25 mm of gauge-length, 3 mm of width and 1 mm of thickness) in an ATS Universal 900 tensile tester at across-head speed of 25 mm/min. At 10 vol%, PR-19 HT nanocomposites displayed a tensile modulus of 632±36 MPa, tensile strength of 14.2±1.5 MPa and strain-to-failure of 180±98 % (n = 6 in all cases). Thus, as compared

with pure LLDPE, which has a modulus of 325±85 MPa, strength of 30±5 MPa, and strain-to failure of 685±105% (n = 6), the modulus increased by about 100 %, but the strength decreased by about 50 %. Nonetheless, thin extruded nanocomposite films still displayed a very good level of flexibility. It is important to note that while the nanocomposites were generally less ductile as compared to the pure LLDPE, they still retained a fairly high strain-to-failure of 180±98 %, compared to about 2% displayed in typical carbon fiber/LLDPE composites at the same volume fraction, as shown in our previous work [19]. Coupled with an EM SE of about 14±2 dB, such nanocomposites indicate a potential in flexible packaging and micromolding applications.

2.4 Conclusions

After an ultra-high temperature thermal treatment at 2500°C, PR-19 HT nanofibers showed a significant increase in their graphitic crystallinity and two orders of magnitude increase in their bulk electrical conductivity. Subsequently, nanocomposites containing 10 vol% (~20 wt%) PR-19 HT exhibited an outstanding improvement in their electrical conductivity (ten orders of magnitude) and electromagnetic shielding effectiveness (EM SE increase of ~13 dB) as compared to their untreated counterparts. Over a frequency range from 30 MHz to 1.5 GHz, the EM SE of the PR-19 HT nanocomposites at 10 vol% was about 14±2 dB (n = 4). These EM SE values were significantly larger than those measured for untreated PR-19 nanocomposites (~1±0.2 dB, n = 4). The total EM SE (dB) of PR-19 HT nanocomposites increased almost linearly with the thickness of the sample, and approached the EM SE target of 20 dB (for residential electronics applications) for the thickest ones. Absorption was the predominant shielding mechanism, which combined with their flexibility and ductility, make such nanomaterials promising alternatives for electromagnetic compatibility (EMC) applications.

2.5 References

1. Paul CR. Introduction to Electromagnetic Compatibility. United States of America: John Wiley & Sons, Inc., 1992.

2. Ramo S, Whinnery JR, Van Duzer T. Fields and Waves in Communication Electronics. United States of America: John Wiley & Sons, Inc., 1984.

3. Al-Saleh MH, Sundararaj U. Electromagnetic interference shielding mechanisms of CNT/polymer composites. Carbon 2009;47:1738-1746.

4. Al-Saleh MH, Gelves GA, Sundararaj U. Copper nanowire/polystyrene nanocomposites: Lower percolation threshold and higher EMI shielding. Composites Part A 2011;42:92-97.

5. Al-Saleh MH, Sundararaj U. Electrically conductive carbon nanofiber/polyethylene composite: effect of melt mixing conditions. Polym Adv Technol 2011;22:246-253.

6. Gelves G, Lin B, Sundararaj U, Haber J. Low Electrical Percolation Threshold of Silver and Copper Nanowires in Polystyrene Composites. Adv Func Mater 2006;16: 2423-2430.

7. Dani A, Ogale AA. Electrical Percolation Behavior of Short-fiber Composites: Experimental Characterization and Modeling. Compos Sci Technol 1996;56:911-920.

8. King JA, Morrison FA, Keith JM, Miller MG, Smith RC, Cruz M, Neuhalfen AM, Barton RL. Electrical Conductivity and Rheology of Carbon-Filled Liquid Crystal Composites. J App Polym Sci 2006;101:2680-2688.

9. Keith JM, King JA, Miller MG, Tomson AM. Thermal conductivity of carbon fiber/liquid crystal polymer composites. J Appl Polym Sci 2006;102:5456-5462.

10. Yang S, Lozano K, Lomeli A, Foltz HD, Jones R. Electromagnetic interference shielding effectiveness of carbon nanofiber/LCP composites. Composites Part A: Appl Sci Manuf 2005;36(5):691-697.

11. Lozano K, Yang S, Zeng Q. Rheological analysis of vapor-grown carbon nanofiber-reinforced polyethylene composites; J. Appl. Polym. Sci., 2004;93:155-162.

12. King JA, Johnson BA, Via MD, Ciarkowski CJ. Effects of carbon fillers in thermally conductive polypropylene based resins. Polym Compos 2010;31:497-506.

13. Nanni F, Valentini M. Electromagnetic properties of polymer-carbon nanotube composites. In: McNally T, Pötschke P, editors. Polymer-carbon nanotube composites, Preparation, properties and applications. Cambridge, UK: Woodhead Publishing, 2011, pp. 329-346.

14. Wang SF, Ogale AA. Continuum space simulation and experimental characterization of electrical percolation behavior of particulate composites. Compos Sci Technol 1993;46:93-103.

15. Dani A, Ogale AA. Percolation in Short-fiber Composites: Cluster Statistics and Critical Exponents. Compos Sci Technol 1997; 57:1355-1361.

16. King JA, Via MD, Keith JM, Morrison FA. Effects of Carbon Fillers on Rheology of Polypropylene-based Resins. J Compos Mat 2009;43:3073-3089.

17. Xiao KQ, Zhang LC, Zarudi I. Mechanical and rheological properties of carbon nanotube reinforced polyethylene composites. Compos Sci Technol 2007;67:177-182.

18. Kum CK, Sung Y, Han MS, Kim WN, Lee HS, Lee S, Joo J. Effect of Morphology on the Electrical and Mechanical Properties of the Polycarbonate/Multi-Walled Carbon Nanotube Composites. Macromol Res 2006;14:456-460.

19. Villacorta BS, Ogale AA. Effect of Ultra-High Thermal Treatment of Carbon Nanofibers on EMI SE of LLDPE Nanocomposites. SPE ANTEC 2011, 2011;11:0093.

20. Lee S, Kim M, Ogale AA. Influence of Carbon Nanofiber Structure on Properties of Linear Low Density Polyethylene Composites. Polym Eng Sci 2010;50:93-99.

21. Janda NB, Keith JM, King JA, Perger WF, Oxby TJ. Shielding-Effectiveness Modeling of Carbon-Fiber/Nylon-6,6 Composites. J Appl Polym Sci 2005;96:62-69.

22. Ling Q, Sun J, Zhao Q, Zhou Q. Microwave absorbing properties of linear low density polyethylene/ethylene–octene copolymer composites filled with short carbon fiber. Mater. Sci Eng B 2009;162:162-166.

23. Jimenez GA, Jana SC. Electrically conductive polymer nanocomposites of polymethylmethacrylate and carbon nanofibers prepared by chaotic mixing. Composites Part A: Appl Sci Manuf 2007;38:983-93.

24. Lee S, Da S, Ogale AA, Kim M. Effect of heat treatment of carbon nanofibers on polypropylene nanocomposites. J Phys Chem Solids 2008;69:1407-1410.

25. Lee S, Kim T, Ogale AA, Kim M. Surface and structure modification of carbon nanofibers. Synth Met 2007;157:644-650.

26. Villacorta BS, Hubing TH, Ogale AA. Effect of Heat Treatment of Carbon Nanofibers on the Electromagnetic Shielding Effectiveness of Linear Low Density Polyethylene Nanocomposites. Polym Eng Sci 2013;53:417-423.

27. Singjai P, Changsarn S, Thongtem S. Electrical resistivity of bulk multi-walled carbon nanotubes synthesized by an infusion chemical vapor deposition method. Mater Sci Eng A 2007;443:42-46.

28. Park SH, Theilmann P, Yang K, Rao AM, Bandaru PR. The influence of coiled nanostructure on the enhancement of dielectric constant and electromagnetic shielding efficiency in polymer composites. Appl Phys Lett 2010;96:043115.

CHAPTER 3

MORPHOLOGICAL INFLUENCE OF CARBON MODIFIERS ON THE ELECTROMAGNETIC SHIELDING OF THEIR LINEAR LOW DENSITY POLYETHYLENE COMPOSITES

3.1 Introduction

In Chapter 2, it was explained that electrically conductive modifiers are added to polymers to form electrical networks within the polymeric matrix [1-5]. This improves the lossy transport properties of the material, which directly influence the electromagnetic shielding [6]. Moreover, it was shown that the intrinsic transport properties of the modifiers themselves influence the composite transport properties and shielding. Thus, after significantly reducing the bulk electrical resistivity of a commercial grade carbon nanofiber by heat treatment at graphitization temperatures, the resulting composite conductivity and electromagnetic shielding (EM SE) displayed a very significant improvement.

Literature studies indicate that for a given graphitic crystallinity of the modifiers and fixed melt-mixing conditions, the composite properties will also depend on the morphological features of the modifiers, such as aspect ratio, shape and diameter [7-11]. However, the effect of different carbon-based nano-morphologies on the electromagnetic shielding of their polyethylene nanocomposites has not been fully investigated. Therefore, this chapter explores the effect of three different heat-treated carbon-based

nanomodifiers on the EM SE of their composites prepared by melt-mixing with a flexible linear low-density polyethylene matrix. Mesophase pitch-based carbon fibers (P55) with a similar graphitic content were also included in this study with the purpose of comparing micro- vs. nano-morphologies. The microstructural, electrical, thermal, and mechanical properties of such composites are reported in relation to their electromagnetic shielding performance.

3.2 Experimental

3.2.1 Materials

The matrix polymer used throughout this study was Poly(ethylene-co-1-octene), (Dowlex^{TM} 2045), a film grade flexible linear low density polyethylene (LLDPE). It has a density of 0.920 g/cm^3, DSC melting point of 122ºC, and melt flow index of 1 g/10 min (190°C/2.16 kg, ASTM D1238). Carbon nanofibers, Pyrograf® III PR-19 (Applied Science Inc.), straight (MWNT), and helical multi-walled carbon nanotubes (HCNT) from CheapTubes Inc., were used as nanomodifiers. PR-19 CNFs are made by chemical vapor deposition (CVD) from natural gas as precursor by using a Fe-sulfide catalyst at about 900ºC, and have a specific surface area of 15-25 m^2/g [12,13]. MWNT are also produced by CVD from methane with a Ni-Fe catalyst and have about 60 m^2/g of specific surface area, whereas HCNT were made of C_2H_2 precursor by CVD at 500°C with a Fe_2O_3 catalyst and have a specific surface area of less than 30 m^2/g [14]. With the purpose of comparing the performance of three different nano-morphologies with

traditional micro-fibers, mesophase pitch-based Cytec Thornel® P-55 short carbon fibers (CF) were also used (length: 0-2 mm, diameter ~10 μm).

For the electrical composite properties, one of the most important factors is the intrinsic electrical conductivity of the modifier phase. This, in turn, is a strong function of its graphitic crystallinity, which can be increased by heat-treating the nanomodifiers to temperatures exceeding 2000°C as demonstrated in Chapter 2 and previous studies [12, 13, 15]. Therefore, ultra-high thermal treatment (HT) at 2500 °C was carried out for the as-received nanomodifiers in a Thermal Technology HP50-7010 furnace in helium atmosphere prior to compounding [16].

3.2.2 Processing

As documented in Appendix A, high-shear mixing geometries (twin-screw extrusion) and long mixing times reduced the electrical network in 10 vol% PR-19 HT composites due to excessive mixing, which decreased the cluster-cluster electrical interconnection. In contrast, higher levels of conductivity and EM SE were attained by using softer mixing conditions (Brabender-type batch mixing) for the same concentration. Therefore, in this chapter, the nanocomposites were prepared by an optimized soft melt-mixing of LLDPE with 10 vol% of each of the four types of modifiers in a Haake Rheomix 600 batch mixer (BM) at 190°C and 20 rpm for 2 min. The composites were processed by thermal compaction at 190°C into circular sheets about 2.5-3.0 mm thick

and 133 mm diameter utilizing a Carver laboratory press. Two specimens were independently mixed and compacted per concentration (true replicates, n = 2).

3.2.3 Carbon modifier characterization

Scanning electron microscopy (SEM Hitachi S-4800) was conducted on the heat-treated modifiers. At least 10 different micrographs at different levels of magnification were captured per modifier type. From such high-magnification SEM micrographs, the length and diameter measurements of the modifiers were carried out using image analysis (ImagePro®). For each modifier type, a set of at least 150 representative imaged modifiers were measured.

Raman spectroscopy was conducted for the modifiers to analyze the disordered (D) and graphitic (G) bands observed in carbon materials at 1315 cm^{-1} and 1580 cm^{-1}, respectively. A Renishaw micro-Raman spectroscope equipped with a 785 nm wavelength diode laser was used. The WiRE software (version 3.2) was used to analyze the peaks to determine the I_D/I_G Raman area ratio [12]. A replication of 8 was used (n = 8).

Wide-angle X-ray diffraction (Rigaku-MSC, Houston, TX) was also conducted on the heat-treated carbon modifiers using Cu target Kα radiation with a wavelength of 1.5406 Å [12]. The spectra were analyzed using Polar software version 2.6.7 from Stonybrook Technology and Applied Research (STAR). X-ray diffraction (XRD) was

also conducted on the modifier using a Rigaku Ultima IV X-ray diffractometer to corroborate the 2θ angle values. A Bragg's angle sweep from 20° to 30° was used at a rate of 0.75°/min for all measurements, using also Cu target Kα radiation with a wavelength of 1.5406 Å. The Ultima IV X-ray source was operated at 40 kV and 44 mA. In addition, a small quantity of NIST-calibration grade silicon was added to the samples for accurate determination of 2θ angles of various peaks. A replication of 3 was used for all XRD experiments (n = 3)

The bulk electrical resistivity (BER) of the pure modifiers was measured using a Keithley 196 System digital multi-meter (DMM) while compressing the modifiers in an insulating fixture. The bulk electrical resistivity of the modifiers was computed from the measured resistance and sample geometry at a compaction stress of 50 MPa [17].

The bulk thermal diffusivity of the nanomodifiers was measured using a NETZSCH Laser Flash Analyzer LFA 447 (ASTM E1461). Compacted pellets of 2 mm thickness and 12.7 mm diameter made out of the nanomodifiers were prepared for the diffusivity analysis. The bulk thermal conductivity was calculated from the bulk thermal diffusivity, bulk density measurements and the heat capacity obtained from a simple mixing rule for the carbon modifiers and air. Two true pellet replicates (n = 2) were made for each nanomodifier.

3.2.4 Composites characterization

The morphology of the resulting nanocomposites was assessed by inspection of the cross-section of the cryo-fracturated nanocomposites using scanning electron microscopy (Hitachi S-4800, Hitachi SU-6600). For each type of nanocomposite, five different macroscopic locations were investigated. For each location, five different spots were imaged. After a soft dilution of the 10 vol% composites with LLDPE to 1 vol%, carried out in the batch mixer at 20 rpm, 190°C for 2 min, the composites became transparent enough to conduct transmission optical microscopy (OM) using a BX60 Olympus Optical Microscope. Seven different locations on the surface of ~100-μm thick composite films were inspected for each composite type. For each location, two different magnifications were imaged (5X: nominally 4 mm^2 of inspected area, and 10X: nominally 1 mm^2 of inspected area). ImagePro® image analysis software was used to measure the average diameter and area of the clusters in an attempt to characterize their dispersion level.

The DC in-plane volume electrical conductivity, σ (S/m), of the nanocomposites was measured using a Keithley 6517B High Resistance Meter (current range: 1 pA - 20 mA) connected to a Keithley 8002A Resistivity Test Fixture modified with external electrodes (ASTM D257). The measurements were performed with help of the Keithley 6524 software by which a DC voltage of ± 5V was applied across the highly conductive composite samples and ± 50V across the less conductive samples. The relative humidity and temperature of the experimental area were monitored using a 6517-RH humidity

probe and a 6517-TP thermocouple, respectively. The conductivity was obtained from resistance measurements of die-cut specimens that were 12.5 mm wide, 2.5 mm thick and with lengths of about 20 mm. Silver paint was applied on the surfaces at each end of the samples and their in-plane resistance was measured. From the sample geometry and the resistance measurements, the conductivity was computed from four replicates (n = 4). The measurements were performed on a 6-mm thick Teflon® sheet to insulate the area for accurate measurements. Documented details of the in-plane conductivity measurements are displayed in Appendix B.

The NETZSCH Laser Flash Analyzer LFA 447 (ASTM E1461) was also use to measure the through-plane thermal diffusivity of the composites. Four square specimens of 10 mm x 10 mm and about 0.5 mm thick were cut per composite type (n = 4). From mixing rules the heat capacity and density of the composites were calculated, enabling the estimation of their composite thermal conductivity.

The complex electrical permittivity (real ε' and imaginary ε'') of the nanocomposites, in their sheet form (2.5 mm thick), was measured utilizing an Agilent 4291B RF Impedance/Material Analyzer and an Agilent 16453A Dielectric Material Test Fixture. Prior to the measurements, the analyzer was calibrated utilizing an Agilent calibration kit (short (0 Ω), open (0 S), load (50 Ω)). Short/open/load fixture compensation was also applied to increase the accuracy of the measurements. The analysis frequency range was 30 MHz to 1.5 GHz.

The static decay time was measured using an Electro-Tech Systems, Inc. 406D Static-Decay Meter that complies with the Federal Test Method 101D, Method 4046 and Military Standard Mil-B-81705C. This standard requires that 99% of the initial induced charge be dissipated is less than 2 seconds for qualifying material per Mil-B-81705C. The Static-Decay Meter was calibrated by the ESD Testing Laboratory of Electro-Tech Systems, Inc. (Glenside PA) prior to the measurements. The relative humidity of the measuring area was monitored at about 50% and temperature of 25°C.

An Electro-Metrics EM-2107A coaxial transmission line test fixture was used to apply a far-field electromagnetic wave to the nanocomposite specimens (ASTM D4935). The EM-2107A test fixture was connected through coaxial cables to an Agilent Technologies N5230A PNA Series Network Analyzer. The EM SE was determined as ten times the negative logarithmic ratio of the measured transmitted power with the material present (load specimen), $P_{T,W}$, to the transmitted power without the material present (reference specimen), $P_{T,WO}$. In Appendix B, this ratio is equivalently defined as the corrected transmittance, T, expressed in dB. Thus, each circular nanocomposite specimen was aligned between the test fixtures and measured at frequencies from 30 MHz to 1.5 GHz. Two true replicates were tested (n = 2). The sample diameter was 133 mm, whereas the thickness was 2.5 mm.

Tensile tests were carried out for the nanocomposites using the ASTM D638 Type V technique at room temperature, which requires dogbone-shaped specimens of 25 mm of gauge-length and 3 mm of width. The specimens were of 1 mm in thickness and were

die-cut into the ASTM dogbone shape. An ATS Universal 900 tensile tester at across-head speed of 25 mm/min was used to test six replicates per nanocomposite type.

3.3 Results and Discussion

3.3.1 Carbon modifiers morphology and properties

Figure 3.1 contains representative SEM micrographs displaying the morphologies of the four different heat-treated carbon modifiers used in this chapter for the preparation of the composites. P-55 CF, PR-19 HT and MWNT HT are straight-shaped fibers, but P-55 CF have a diameter about two orders of magnitude greater than that of PR-19 HT, and PR-19 HT possess a diameter one about one order of magnitude larger than that of MWNT HT. HCNT HTs have a similar diameter to that of PR-19 HT; however, a predominantly helically coiled morphology is a distinctive feature of HCNT HT. The as-received HCNT displayed a larger helical content, which was reduced by the heat treatment.

Figure 3.2 contains histograms for the diameter and length distributions of the modifiers obtained from image analysis of their SEM micrographs. PR-19 HT CNFs have a diameter of 119±8 nm and a length of 10±2 μm, whereas MWNTs HT have a diameter of 42±3 nm and length of 6±1 μm (i.e., average ± 95% confidence intervals). HCNTs HT have a nominal diameter of 210±15 nm and a length of 8.5±2.5 μm. P-55 CFs have an average diameter of about 10 μm and lengths of about 100-500 μm. Thus,

the average aspect ratios for the modifiers are about 86, 146, 41 and 30 for the PR-19 HT, MWNT HT, HCNT HT and P-55 CF, respectively.

Figure 3.3 displays representative SEM micrographs at low magnification for the heat-treated carbon nanomodifiers showing the initial level of clustering of the modifiers before melt-mixing. Clusters as large as 100 μm were observed for PR-19 HT, whereas the HCNT HT displayed smaller cluster size than did other nanomodifiers.

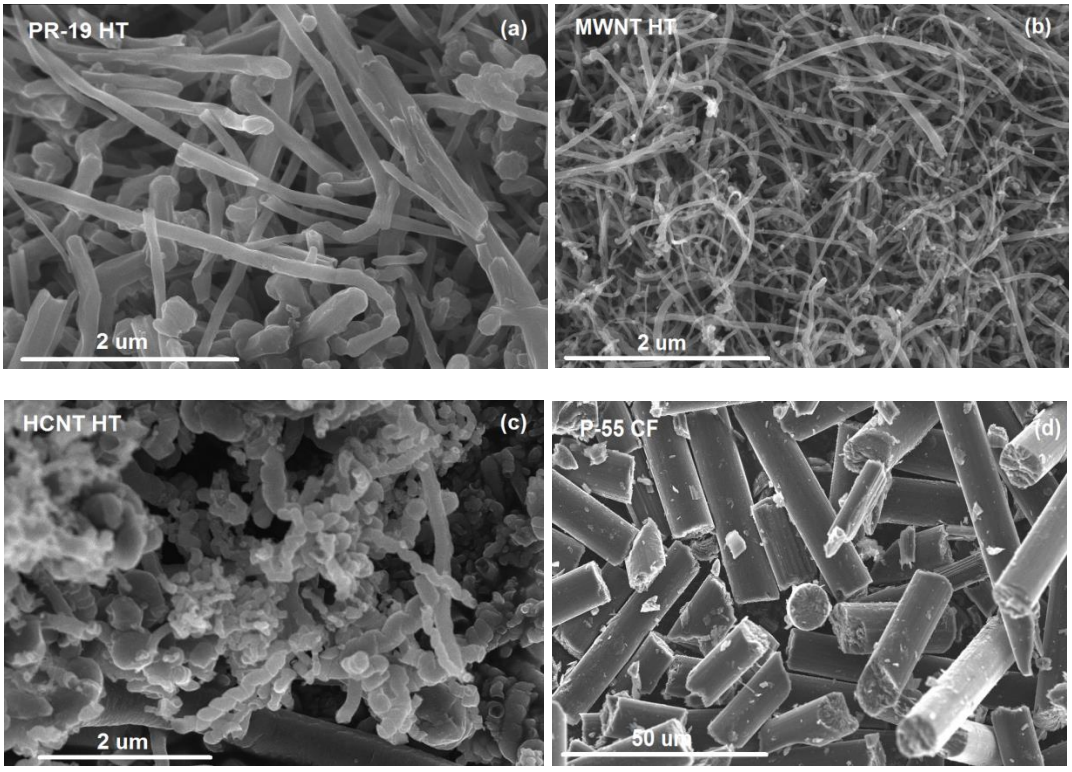

Figure 3.1. Representative scanning electron micrographs (SEM) of the heat-treated carbon modifiers used to prepare the composites.

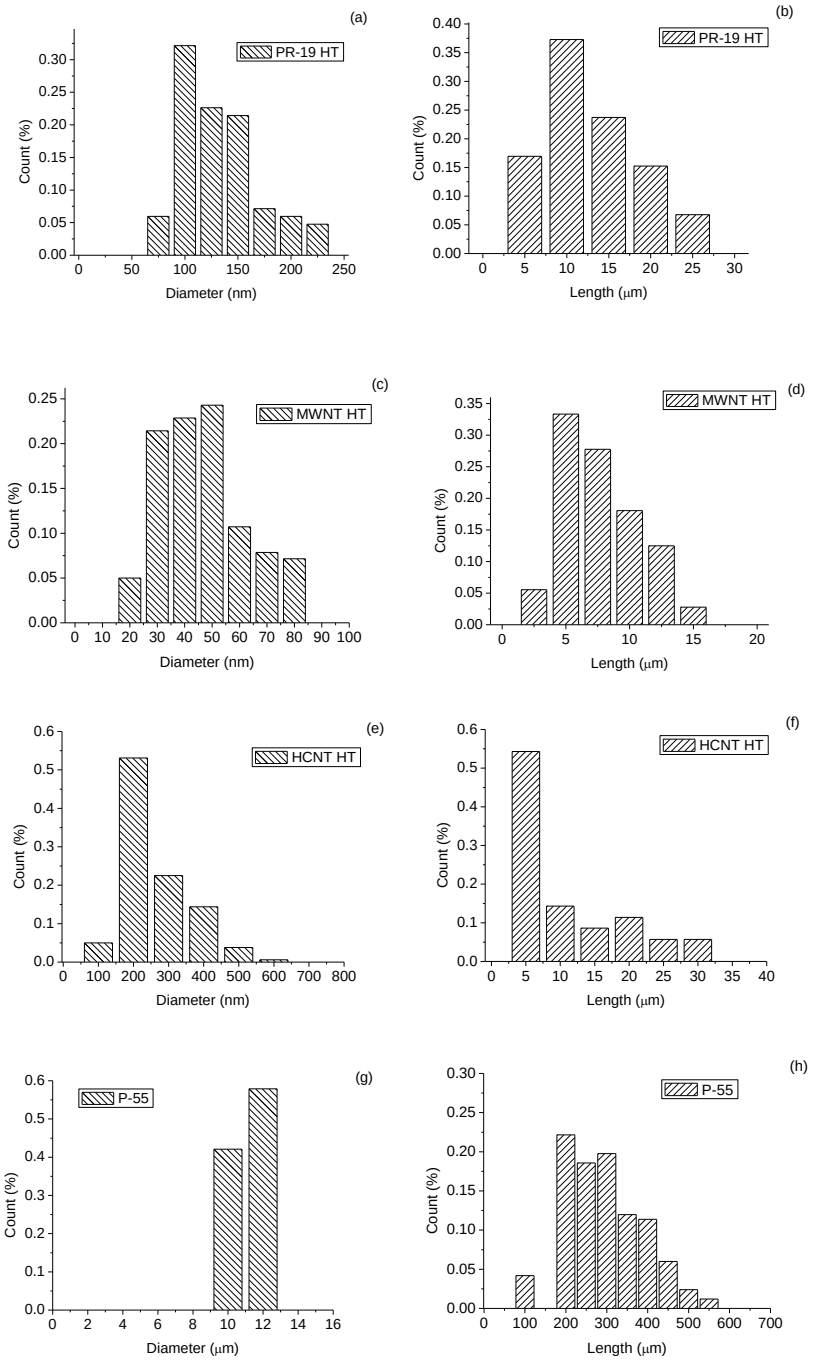

Figure 3.2. Results of the dimensional analysis of the carbon modifiers presented as histograms for the diameter and length distributions for (a, b) PR-19 HT, (c, d) MWNT HT, (e, f) HCNT HT and (g, h) P-55 CF.

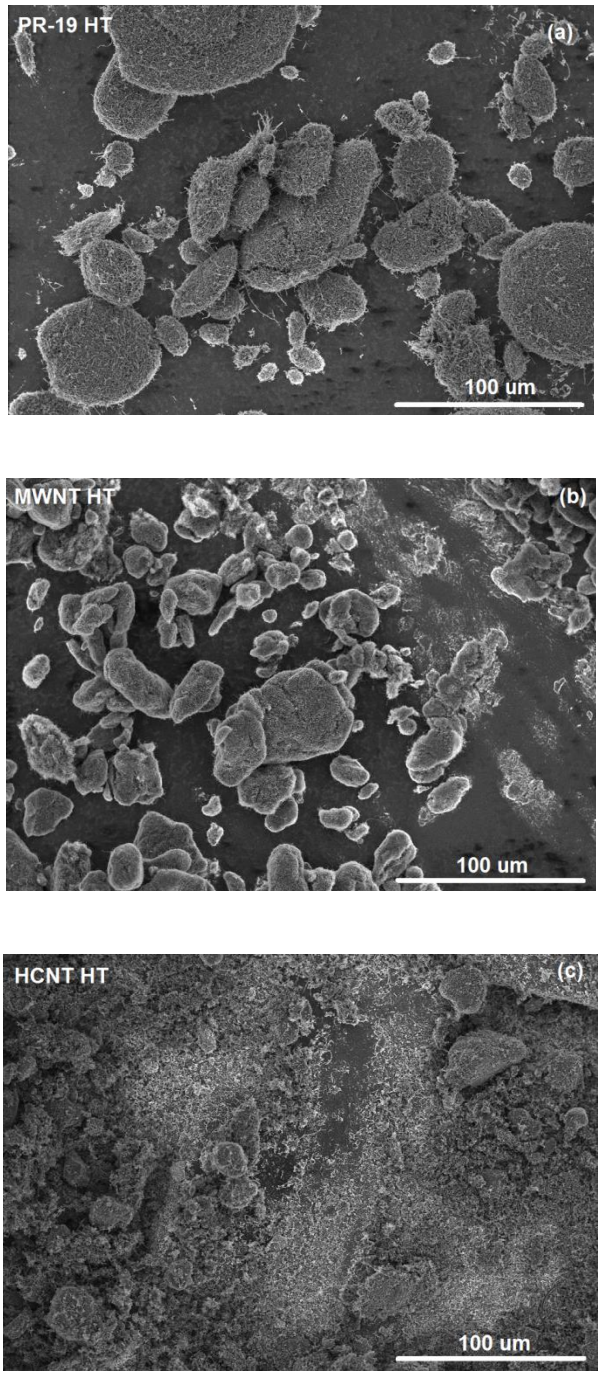

Figure 3.3. Representative low-magnification scanning electron micrographs (SEM) of the heat-treated carbon nanomodifiers forming initial clusters. a) PR-19 HT, b) MWNT HT, c) HCNT HT.

Figure 3.4 exhibits the Raman spectra for the four types of carbon modifiers. The Raman I_D/I_G ratios obtained from the relative areas under the D and G bands for the PR-19 HT, MWNT HT and HCNT HT nanomodifiers were 0.96±0.04 and 0.78±0.11 and 1.68±0.46, respectively. HCNT HT displayed a slightly higher ratio than that of the other nanomodifiers. However, due to the large variability in I_D/I_G ratio of HCNT HT, these ratios basically fall in the same category (I_D/I_G ~ 1). Only P-55 had an I_D/I_G ratio of 2.92±0.08, which was significantly higher than that of the nanomodifiers. This indicates that the nanomodifiers have a similar level of graphitic crystallinity, whilst P-55 CF displayed a significant higher level of disorder content (i.e., lower crystallinity).

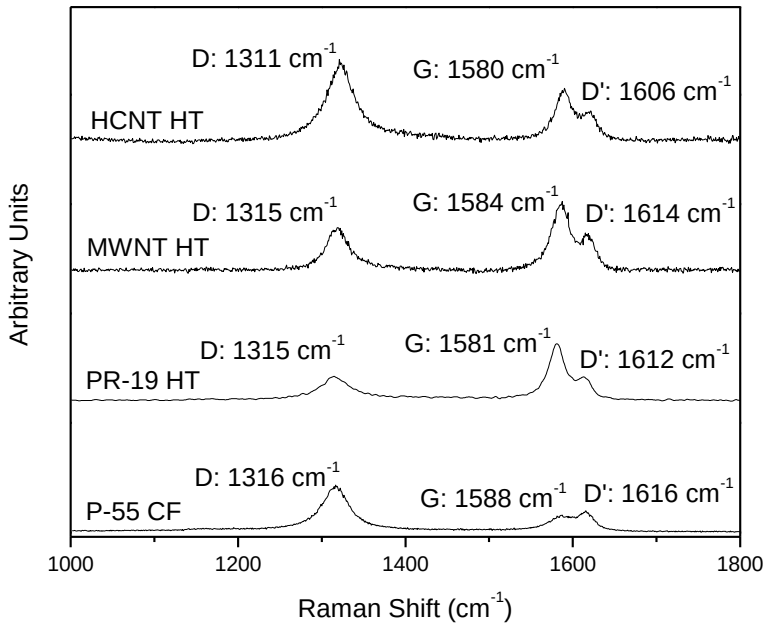

Figure 3.4. Raman spectra of the heat-treated carbon modifiers. The spectra have been vertically shifted for clarity.

Similar deductions can be drawn from the Bragg's angle of the graphitic (002) peak obtained from wide angle X-ray diffraction of the modifiers. **Figure 3.4** confirms that the 2θ positions of the nanomodifiers are around 26.2° (graphitization level at about 50%), which are consistent with the Raman results. P-55 carbon fibers displayed a slightly lower 2θ position at 26.01° (graphitization level at about 20%), which corroborates their lower crystallinity level as compared with that of the rest of nanomodifiers. This is also consistent with the Raman results.

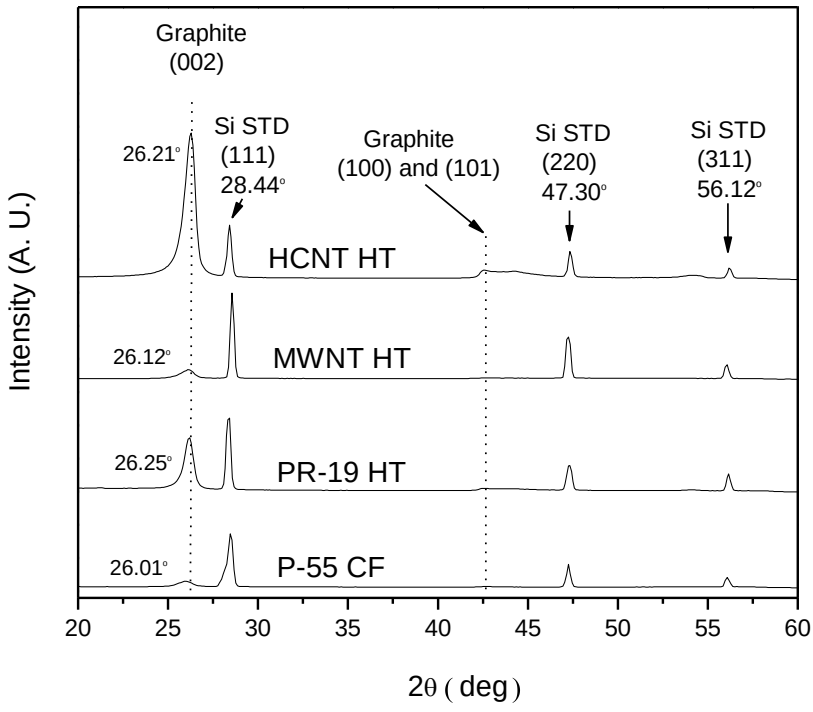

Figure 3.5. Wide angle X-ray diffractograms of the heat-treated carbon modifiers. A small quantity of NIST-calibration grade silicon was added to the samples for accurate determination of 2θ angles of various peaks.

The intrinsic transport properties of the modifiers correlate very well with the graphitic content of the modifiers. Thus, the electrical resistivity of the modifiers in bulk was of 0.031±0.010 Ω·cm, 0.028±0.015 Ω·cm, 0.057±0.014 Ω·cm and 0.116±0.036 Ω·cm for the PR-19 HT, MWNT HT, HCNT HT and P-55 CF, respectively. Likewise, the bulk thermal conductivity of the nanomodifiers was of 0.295±0.010 W/m.K for PR-19 HT, 0.473±0.007 W/m.K for MWNT HT and only 0.155±0.018 W/m.K for HCNT HT. These results indicate that differences in the crystallinity of the modifiers influence their transport properties. Nonetheless, all the transport properties of these modifiers are of the same order of magnitude.

3.3.2 Composite morphology

Figure 3.6 displays representative SEM micrographs for the composites at 10 vol%. The PR-19 HT-, MWNT HT-, and P-55-based composites appear uniformly mixed and no significant clusters can be observed. In contrast, HCNT HT-based composites developed several HCNT HT clusters as large as 100 μm that can be observed by SEM. In fact, the cluster size developed in the HCNT HT composites is comparable to the size of the HCNT HT agglomerates before melt-mixing (i.e., < 100 μm) as observed in **Figure 3.3 (c)**. This is likely a consequence of the helical morphology of the HCNT HT that resulted in more entanglements among themselves, which hinders modifier micro-dispersion and led to a segregated microstructure with a similar cluster size prior and after mixing.

Figure 3.7 shows the optical micrographs (OM) of the diluted composites at 1 vol%. In contrast to the SEM micrographs, optical microscopy, that covers a much larger inspected area (i.e., larger length-scale), displayed clusters of nanomodifiers for all three types of nanocomposites. Only a few clusters were observed for the diluted PR-19 HT- and MWNT HT-nanocomposites, although some were fairly large (~300 μm). In contrast, in the diluted HCNT HT nanocomposites, a larger number of relatively smaller clusters can be observed. These microstructural differences will play a major role in determining the electrical properties of the composites as seen further in this chapter. Moreover, the diluted P-55 CF composites displayed a random in-plane distribution of the fibers, but there are still regions in which higher concentrations of CF are observed. Thus, the microstructural differences found between the two microscopy length-scales (SEM vs. OM) indicate that dispersion assessment must be done at different magnification levels for an appropriate characterization of the dispersed phase.

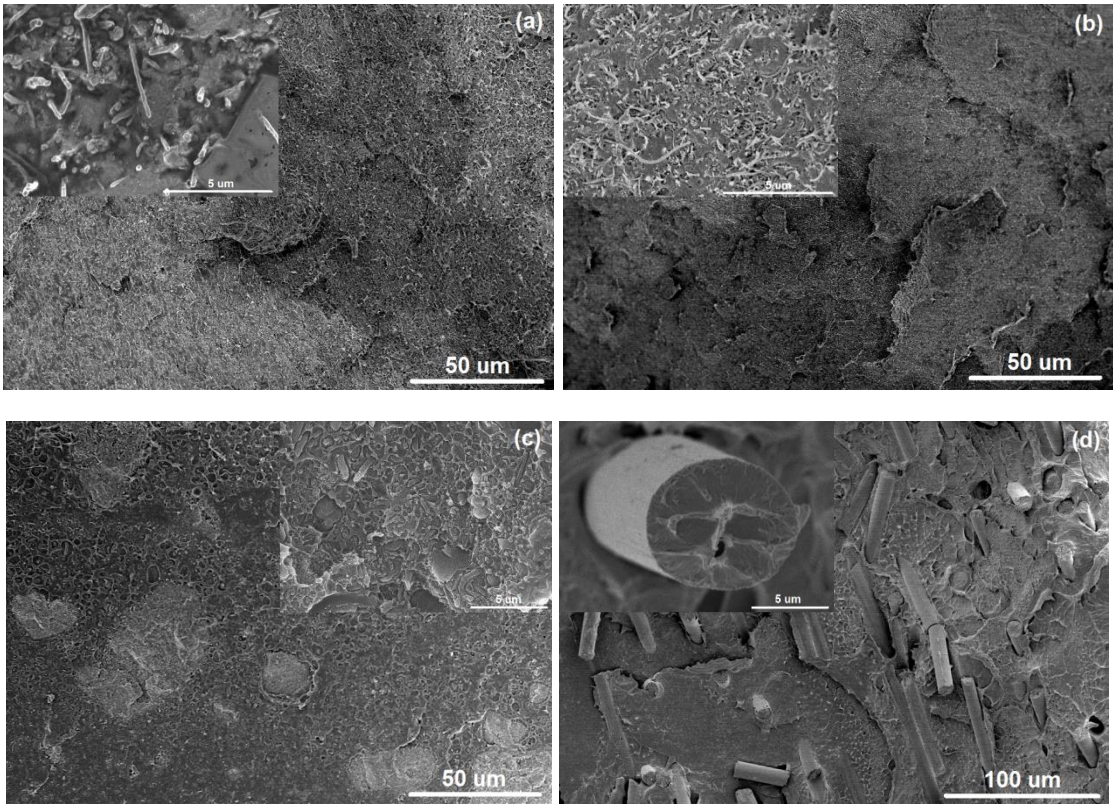

Figure 3.6. Representative scanning electron micrographs (SEM) of the cross-section of the composites at 10 vol% (a) PR-19 HT, (b) MWNT HT (c) HCNT HT and (d) P-55 CF. Insets display the microstructure at higher magnification.

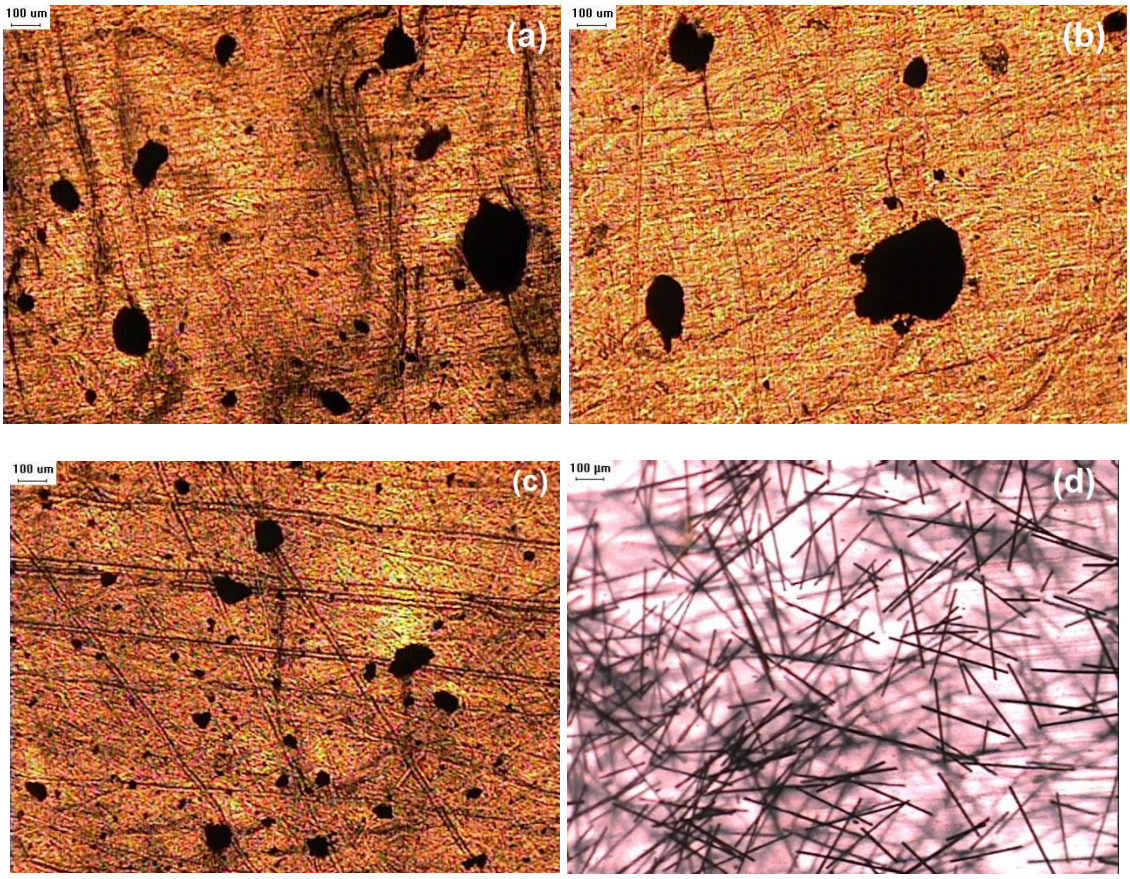

Figure 3.7. Representative optical micrographs of the surface of the diluted composites at 1 vol%, (a) PR-19 HT, (b) MWNT HT (c) HCNT HT and (d) P-55 CF.

Figure 3.8 displays the corresponding average cluster size distribution of the nanomodifiers in the 1-vol% diluted composite films obtained by image analysis of their optical micrographs. The clusters in the PR-19 HT diluted composites had a diameter of 20.7±15.4 µm. For the MWNT HT diluted composite films, a diameter of 21.5±12.9 µm was measured. The HCNT HT dilute nanocomposites displayed an average diameter of 16.9±6.3 µm. These values are consistent with the visual assessment previously made.

Although, the coiled morphology of the HCNT HT favors clustering, the relatively smaller average cluster size in HCNT HT composites may be a consequence of the lower aspect ratio of the HCNT HT.

A measure of the non-disperse phase can be obtained with the ratio of the total cluster area, A_C, to the total inspected area, A_T [19]. This ratio is proportional to the volume fraction of the clusters in the composite [19]. Thus, PR-19 HT, MWNT HT and HCNT HT diluted nanocomposites exhibited ratio values of A_C/A_T of 0.379±0.075, 0.378±0.042 and 0.207±0.064, respectively. Thus, even though the SEM micrographs for the HCNT HT nanocomposites at 10 vol% displayed clusters, their predominant cluster size and cluster area ratio were lower than those of the PR-19 HT and MWNT HT nanocomposites. These results quantitatively corroborate that a higher number of relatively smaller isolated clusters are present in the HCNT HT nanocomposites. Consequently, the smaller HCNT HT cluster size and the segregated microstructure thus attained hinder electrical interconnection at the micro-scale. This is not the case for the other nanomodifiers, whose larger aspect ratios and cluster sizes led to higher levels of inter-cluster connection.

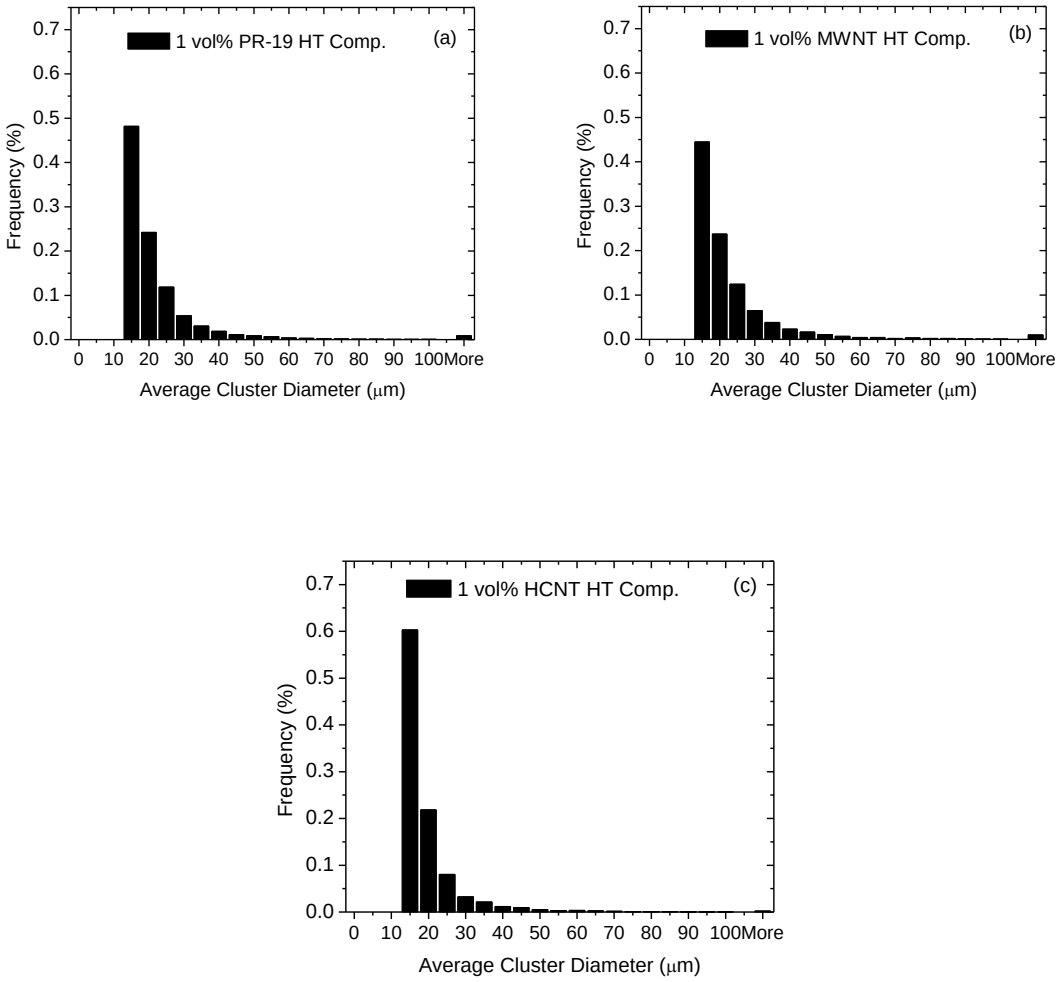

Figure 3.8. Cluster size distributions in 1 vol% diluted nanocomposites. (a) PR-19 HT comp., (b) MWNT HT comp. and (c) HCNT HT comp.

3.3.3 Composite transport properties

For polyolefin matrix nanocomposites, electrical percolation thresholds ranging from 2.5 to 7.5 vol% have been reported for CNFs and CNTs in literature studies [2, 16, 20]. However, even though at the percolation threshold (e.g., 10^{-5} to 10^{-2} S/m) the conductivity of the composite is several orders higher than that of the pure resin (e.g., 10^{-17} to 10^{-15} S/m), it is insufficient for shielding purposes. Therefore, for obtaining significant shielding effectiveness, it is necessary to increase loading levels beyond the percolation threshold. Because of this, and based on the results of Chapter 2, the batch-mixed formulation of 10 vol% is better suited for a systematic evaluation of the shielding properties.

Table 3.1 is a summary of the transport properties of the modifiers and their composites. The DC in-plane electrical conductivity σ of the 10 vol% nanocomposites was measured at $33.5\pm5.6\text{x}10^{0}$ S/m, $20.4\pm3.3\text{x}10^{0}$ S/m, $3.7\pm1.6\text{x}10^{-3}$ S/m and $5.0\pm1.8\text{x}10^{0}$ S/m (n = 4 in all cases) for the PR-19 HT, MWNT HT, HCNT HT and P-55 composites, respectively. The composites were electrically percolated systems when compared with a conductivity of $7.0\pm1.1\text{x}10^{-15}$ S/m for pure LLDPE, which is 15 orders of magnitude lower than that of the composites. Similarly, the through-plane thermal conductivity of the composites (also shown in **Table 3.1**) was 0.855±0.029, 1.022±0.023, 0.555±0.003, and 0.562±0.009 W/m·K for the PR-19 HT, MWNT HT, HCNT HT and P-55 composites, respectively.

Since all four types of modifiers have similar transport properties, and the processing conditions and concentration have been kept equal for the same polymeric matrix, the composite properties are solely dependent on the morphological features of the modifiers. Thus, the MWNT HT with the highest aspect ratio (L/D) led to composites with the highest conductivities; whereas HCNT HT, with a low aspect ratio and a helical morphology, prevented a good distribution/segregation within the matrix and led to the lowest conductivities. The PR-19 HT and P-55 CF conductivities fall in between these two extremes as do their aspect ratios.

Table 3.1. Intrinsic properties of four types of modifiers as compared with the conductivity of their batch-mixed composites at 10 vol% modifier content. Ranges represent 95% confidence intervals.

Modifier	**Raman I_D/I_G ratio**	**Bragg's angle (deg)**	**Bulk electrical resistivity (Ω·cm)**	**Bulk thermal conductivity (W/m.K)**	**Aspect ratio (L/D)**	**In-plane electrical conductivity (S/m) Composites 10 vol%**	**Through-plane thermal conductivity (W/m.K) Composites 10 vol%**
PR-19 HT	0.96±0.04	26.25	0.031±0.010	0.295±0.010	63-108	$20.4\pm3.3\times10^{0}$	0.855±0.029
MWNT HT	0.78±0.11	26.12	0.028±0.015	0.473±0.007	111-180	$33.5\pm5.6\times10^{0}$	1.022±0.023
HCNT HT	1.68±0.46	26.21	0.057±0.014	0.155±0.018	26-56	$3.7\pm1.6\times10^{-3}$	0.555±0.003
P-55	2.92±0.08	26.01	0.116±0.036	-	24-35	$5.0\pm1.8\times10^{0}$	0.562±0.009

Another transport property of relevance is the complex electrical permittivity of the nanocomposites ($\varepsilon = \varepsilon' - j\varepsilon''$) displayed in **Figure 3.9** from 30 MHz to 1.5 GHz. $\varepsilon'/\varepsilon_0$ represents the dimensionless real relative permittivity or dielectric energy storage, and $\varepsilon''/\varepsilon_0$ the dimensionless imaginary relative permittivity or polarization loss. The permittivity of vacuum ε_0, is 8.85418x10^{-12} F/m. The real and imaginary permittivity of the nanocomposites displayed a generally decreasing behavior with respect to frequency. The MWNT HT nanocomposites exhibited an overall permittivity of (175±60)-(93±34)j at 100 MHz, decreasing to (15±11)-(21±3)j at 1.5 GHz. PR-19 HT nanocomposites permittivity decreased from (100±65)-(63±46)j at 100 MHz to (17±7)-(18±12)j at 1.5 GHz (n = 4 in both cases). In contrast, the permittivity of HCNT HT and P-55 composites was less frequency dependent at about (4±1)-(0.05±0.03)j and (12±2)-(3±1)j at 1.5 GHz, respectively. Once again, the composites made out of modifiers with larger aspect ratios displayed higher values of permittivity. Particularly low was the permittivity of the HCNT HT nanocomposites, which was only slightly higher than that of the pure LLDPE ($\varepsilon/\varepsilon_0 \approx 2.3$). Such a low permittivity also reflects the poor electrical interconnectivity between the HCNT HT clusters.

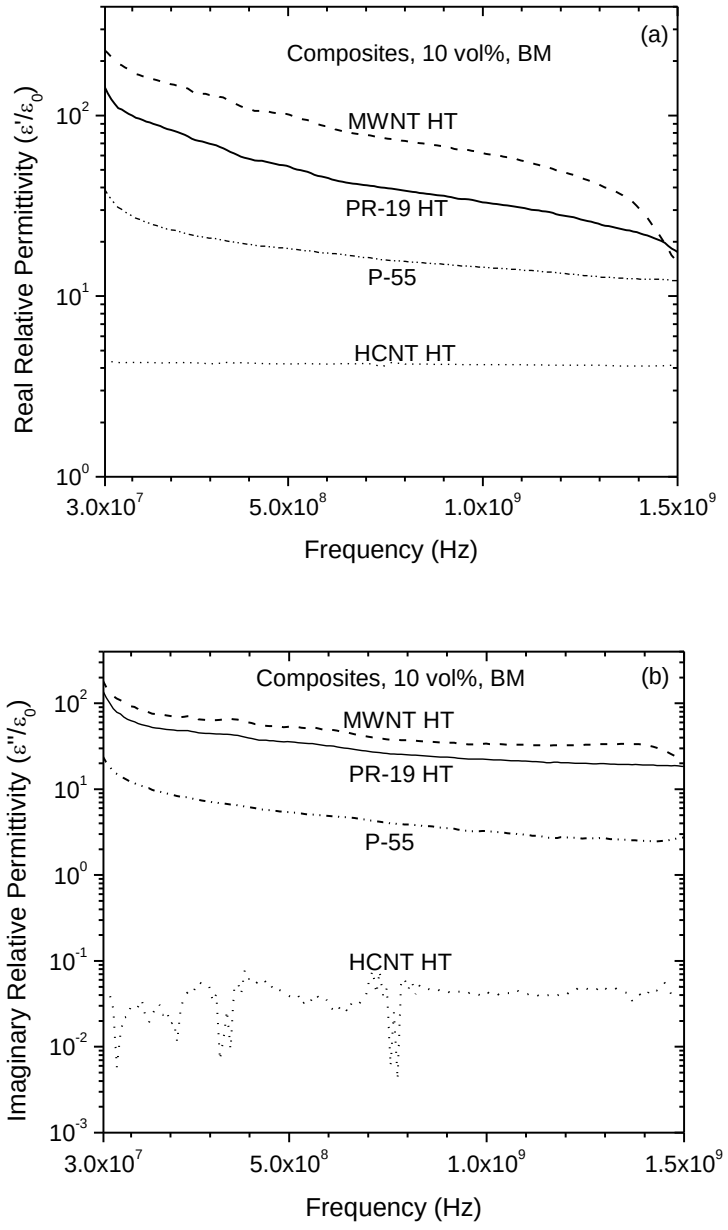

Figure 3.9. Relative (a) real and (b) imaginary electrical permittivity of representative composites.

3.3.4 Electrostatic dissipation and electromagnetic shielding

The electrostatic discharge (ESD) characteristic of the nanocomposites in terms of the decay time for each nanocomposite type is displayed in **Table 3.2** (1 % of cut-off). At 10 vol%, all types of composites were ESD dissipative and complied with the Mil-B-81705C requirements since they all were in the percolated regime. It is known that the electrostatic decay time increases as the conductivity of the material decreases [18, 21]. Only, HCNT HT composites displayed, a slightly higher, but still dissipative, decay time of 1.5 s, which is consistent with its low electrical conductivity of only ~0.004 S/m.

Table 3.2. Static decay-times for electrostatic dissipation (ESD) of the composites, measured at 1 % cut-off and 50 % relative humidity.

10 vol% Composites	**Decay time*** **(sec)**
PR-19 HT	0.01
MWNT HT	0.01
HCNT HT	1.50
P-55	0.01

*1% cut-off

Figure 3.10 displays the electromagnetic shielding effectiveness (EM SE) of the composites. PR-19 HT nanocomposites displayed 24.7 dB of shielding, and MWNT HT nanocomposites a slightly larger value of 25.3 dB (at 1.5 GHz). P-55 composites exhibited 12.2 dB, whereas the lowest value of the set was of only 0.7 dB for the HCNT HT composites at 1.5 GHz. These results are consistent with the electrical conductivity and permittivity measurements as the greater the EM SE, the higher the "lossy" properties of the composite (i.e., electrical conductivity and imaginary permittivity). **Figure 3.11** correlates the EM SE and the in-plane conductivity of the composites. A consistent increasing trend between the in-plane conductivity and the EM SE of the composites can be noted. This confirms the dependency of the EM SE of a material on its electrical conductivity.

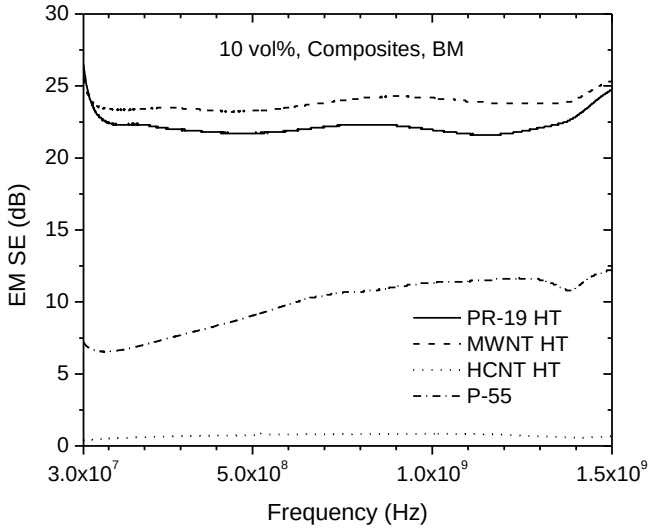

Figure 3.10. Electromagnetic shielding effectiveness (EM SE) of representative composites over the frequency range of 30 MHz to 1.5 GHz, at 10 vol%.

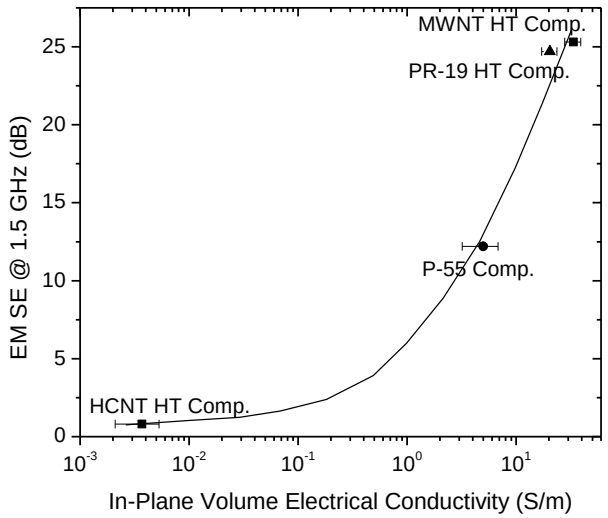

Figure 3.11. Plot showing a positive correlation between the EM SE @ 1.5 GHz and the corresponding in-plane electrical conductivity of the different composites. Solid line represents a typical trend.

3.3.5 Mechanical properties

Table 3.3 displays the tensile properties of the different composites prepared in this study. At 10 vol%, PR-19 HT and MWNT HT nanocomposites displayed similar values for tensile modulus, strength, and ductility (measured as strain-to-failure). In contrast, HCNT HT composites behaved more flexible and more ductile that the other nanocomposites, while P-55 composites were much stiffer and less ductile than others. The higher ductility of the HCNT HT composites is brought about by the helical shape of the nanomodifier. This has been proven by Lee et al. when studying composites made of

similar modifier morphologies to that of the HCNT HT [22]. In comparison, pure LLDPE has a modulus of 325±85 MPa, strength of 30±5 MPa and strain-to failure of 685±105% (n=6). Although the nanocomposites were generally less flexible as compared to the pure LLDPE, they still retained a fairly high strain-to-failure of about 165%, compared to about only 30% displayed by the P-55 composites. This reduction in strength and ductility is consistent with that reported in other nanocomposites prior literature studies [19, 23]

Table 3.3. Tensile properties for composites at 10 vol% modifier content. Ranges represent 95% confidence intervals.

	PR-19 HT	**MWNT HT**	**HCNT HT**	**P-55**
Apparent Modulus (MPa)	683±105	696±110	443±58	1079±88
Yield Stress (MPa)	16.5±1.8	18.3±1.8	13.3±0.3	20.0±1.5
Tensile Strength (MPa)	16.0±2.5	17.7±1.6	14.8±1.7	8.0±1.4
Elongation-at-break (%)	128±49	114±43	254±62	32±8

3.4 Conclusions

The microstructure of the composites was found to directly depend on the morphology of the carbon modifiers, which leads to the electrical network that the modifiers form within the matrix. The EM SE of the composites also exhibited a direct dependence on the modifier morphology. As a result, MWHT HT, whose aspect ratio was the highest of the studied set, displayed the largest conductivity, permittivity and shielding effectiveness (~24 dB) in its composite form. In contrast, the HCNT HT, due to their coiled shape and low aspect ratio, led to non-percolating clusters in the composites, which resulted in poor EM SE (<1 dB). Nevertheless, HCNT HT composites exhibited the highest ductility and flexibility of the studied set of composites, which is owed to the mechanical matrix-modifier interlocking provided by their helical morphology. PR-19 HT and P-55 CF, both with intermediate aspect ratios and straight-shape morphologies, led to composite properties that fell between the two extremes. Moreover, the larger dimensions of the P-55 CF (diameter 100 times larger than nanomodifiers) provided composites with very little ductility and poor flexibility when compared to those of the nanocomposites.

Because the focus of this study is to mainly improve the electrical properties of the composites, HCNT HT will be discarded due to their poor shielding performance of their composites. Thus, in the following chapters, emphasis will be placed on PR-19 HT and MWNT HT as nano-modifiers for composites with enhanced shielding.

3.5 References

1. Al-Saleh MH, Sundararaj U. Electrically conductive carbon nanofiber/polyethylene composite: effect of melt mixing conditions. Polym Adv Technol 2011;22:246-253.

2. Al-Saleh MH, Sundararaj U. Electromagnetic interference shielding mechanisms of CNT/polymer composites. Carbon 2009;47:1738-1746.

3. Gelves G, Lin B, Sundararaj U, Haber J. Low Electrical Percolation Threshold of Silver and Copper Nanowires in Polystyrene Composites. Adv Funct Mater 2006;16:2423-2430.

4. Al-Saleh MH, Gelves GA, Sundararaj U. Copper nanowire/polystyrene nanocomposites: Lower percolation threshold and higher EMI shielding. Composites Part A: App Sci Manuf 2011;42:92-97.

5. King JA, Morrison FA, Keith JM, Miller MG, Smith RC, Cruz M, Neuhalfen AM, Barton RL. Electrical Conductivity and Rheology of Carbon-Filled Liquid Crystal Composites. J App Polym Sci 2006;101:2680-2688.

6. Nanni F, Valentini M. Electromagnetic properties of polymer-carbon nanotube composites. In: McNally T, Pötschke P, editors. Polymer-carbon nanotube composites, Preparation, properties and applications. Cambridge, UK: Woodhead Publishing, 2011, pp. 329-346.

7. Dani A, Ogale AA. Electrical Percolation Behavior of Short-fiber Composites: Experimental Characterization and Modeling. Compos Sci Technol 1996;56:911-920.

8. Dani A, Ogale AA. Percolation in Short-fiber Composites: Cluster Statistics and Critical Exponents. Compos Sci Technol 1997:57:1355-1361.

9. Villacorta BS, Ogale AA. Effect of Ultra-High Thermal Treatment of Carbon Nanofibers on EMI SE of LLDPE Nanocomposites. SPE ANTEC 2011, 2011:11; 0093.

10. Janda NB, Keith JM, King JA, Perger WF, Oxby TJ. Shielding-Effectiveness Modeling of Carbon-Fiber/Nylon-6,6 Composites. J Appl Polym Sci 2005;96:62-69.

11. Ling Q, Sun J, Zhao Q, Zhou Q. Microwave absorbing properties of linear low density polyethylene/ethylene–octene copolymer composites filled with short carbon fiber. Mater Sci Eng B 2009;162:162-166.

12. Lee S, Kim T, Ogale AA, Kim M. Surface and structure modification of carbon nanofibers. Synth Met 2007;157:644-650.

13. Lee S, Kim M, Ogale AA. Influence of Carbon Nanofiber Structure on Properties of Linear Low Density Polyethylene Composites. Polym Eng Sci 2010;50:93-99.

14. Cheap Tubes Inc., http:// http://www.cheaptubesinc.com/ as viewed 30 October 2013.

15. Villacorta BS, Ogale AA, Hubing TH. Effect of Heat Treatment of Carbon Nanofibers on the Electromagnetic Shielding Effectiveness of Linear Low Density Polyethylene Nanocomposites. Polym Eng Sci 2013;53:417-423.

16. Lee S, Da S, Ogale AA, Kim M. Effect of heat treatment of carbon nanofibers on polypropylene nanocomposites. J Phys Chem Solids 2008;69:1407-1410.

17. Singjai P, Changsarn S, Thongtem S. Electrical resistivity of bulk multi-walled carbon nanotubes synthesized by an infusion chemical vapor deposition method. Mater Sci Eng A 2007;443:42-46.

18. Pratt TH. Electrostatic Ignitions of Fires and Explosions. New York: American Institute of Chemical Engineers, 2000.

19. Kasaliwal GR, Villmow T, Pegel S, Potschke P. Influence of material and processing parameters on carbon nanotube dispersion in polymer melts. In: McNally T, Pötschke P, editors. Polymer-carbon nanotube composites, Preparation, properties and applications. Cambridge, UK: Woodhead Publishing, 2011, pp. 92-132.

20. Morcon M, Simon G. Polyolefin-carbon nanotube composites. In: McNally T, Pötschke P, editors. Polymer-carbon nanotube composites, Preparation, properties and applications. Cambridge, UK: Woodhead Publishing, 2011, pp. 511-544.

21. Voldman SH. ESD: Physics and Devices. Vermont: John Wiley & Sons, Ltd, 2004.

22. Lee S, Kim M-S, Ogale AA. Influence of Carbon Nanofiber Structure on Properties of Linear Low Density Polyethylene Composites. Polym Eng Sci 2010;50:93–99.

23. Goh, S.H. Mechanical properties of polymer-grafted carbon nanotube composites. In: McNally T, Pötschke P, editors. Polymer-carbon nanotube composites, Preparation, properties and applications. Cambridge, UK: Woodhead Publishing, 2011, pp. 347-375.

CHAPTER 4

INFLUENCE OF COMPOSITE ELECTRICAL PROPERTIES ON THE ELECTROMAGNETIC SHIELDING CHARACTERISTICS OF POLYETHYLENE-CARBON NANOMODIFIER COMPOSITES

4.1. Introduction

In previous chapters, the influence of the level of graphitic crystallinity (Chapter 2) and modifier morphology (Chapter 3) on the electromagnetic shielding effectiveness (EM SE) of carbon modifier-based polymer nanocomposites for low to intermediate volume fractions was reported [1-17]. However, the higher concentrations of graphitic nanoforms in ductile semicrystalline matrices (to obtain higher EM SE) have not been fully studied yet.

With regards to the theoretical predictions of the EM SE of the composites, several literature studies have accounted for departure from the purely conductive regime [3, 4, 14 and 16]. However, for moderately conductive materials (10^{-6} S/m $<$ conductivity $<$ 10^{3} S/m) [18], the role that the DC electrical conductivity and AC electrical permittivity play on the experimental EM SE has not been systematically reported in literature studies. Therefore, the major objectives of this chapter were: (i) to incorporate heat-treated carbon-based nanofibers and nanotubes (PR-19 CNF and MWNT) in LLDPE matrix at moderate-to-high nanomodifier contents (10 and 40 vol%)

to study their EM SE characteristics at VHF-UHF frequencies ranging from 30 MHz to 1.5 GHz; and (ii) to establish quantitative relationships for the shielding of electromagnetic plane-waves resulting from the moderate effective conductivity of nanocomposites. The results presented in this chapter have been published as "Influence of Composite Electrical Properties on the VHF-UHF Electromagnetic Shielding Characteristics of Polyethylene-Carbon Nanoparticle Composites" [19].

4.2. Experimental

4.2.1. Materials

The matrix polymer used throughout this chapter was also poly(ethylene-co-1-octene), (Dowlex™ 2045), a film grade linear low density polyethylene (LLDPE). It has a density of 0.920 g/cm^3, DSC melting point of 122ºC, and melt flow index of 1 g/10 min (190°C/2.16 kg, ASTM D1238). Carbon nanofibers, Pyrograf® III PR-19 (Applied Science Inc.), and multi-walled carbon nanotubes (MWNT) from CheapTubes Inc., were used as nanomodifiers. To compare the performance of nanocomposites with traditional carbon fiber composites, chopped mesophase pitch-based carbon fibers (Cytec Thornel® P-55 length: 0-2 mm, diameter ~10 μm) were also used as control specimens.

Ultra-high temperature heat treatment (HT) at 2500°C was also carried out for the as-received nanomodifiers prior to compounding [17]. The heat-treated (HT) PR-19 HT nanofibers have a diameter of 119±8 nm and a length of 10±2 μm, whereas MWNTs HT

have a diameter of 42±3 nm and length of 6±1 μm for an aspect ratio (L/D) of about 85 and 145, respectively [15].

4.2.2 Processing

To melt-mix LLDPE with all three types of modifiers, a Haake Rheomix 600 batch mixer (BM) was used at 190°C and 20 rpm for 2 min for concentrations of 10 vol% (~20 wt%) and 40 vol% (~60 wt%). These conditions were chosen after determining that they provide a more optimal EM SE performance exhibited by composites made out of PR-19 HT CNF melt-mixed with LLDPE at such conditions. Details of processing conditions are documented in Appendix A. The composites were processed by thermal compaction at 190°C into circular sheets about 2.5-3.0 mm thick and 133 mm diameter utilizing a Carver laboratory press. Two specimens were independently mixed and compacted per concentration (true replicates, n = 2).

4.2.3 Rheology

To assess the processability of the nanocomposites, shear viscosity measurements were conducted at 190ºC, the processing temperature used for obtaining all samples in this study. For low shear rates (0.1-10 s^{-1}), a TA Instruments Advanced Rheometric Expansion System (ARES) was used in conjunction with a 25-mm cone-and-plate geometry (0.1 rad cone angle), whereas for apparent shear rates from 30 to 10,000 s^{-1}, a

Rheometric Scientific, Inc. ACER 2000 capillary rheometer with an 1-mm diameter die (L/D = 30) was used.

4.2.4 Microstructural characterization

The microstructure of the composites was assessed by inspection of the cross-section of the cryo-fracturated composites (Hitachi S-4800, SEM). For each type of composite, three different macroscopic locations were investigated by SEM. In addition, thin films of ~100 μm in thickness were produced out of 1 vol% nanocomposites obtained by melt-diluting the 40 vol% nanocomposites with pure LLDPE by the same soft mixing protocol. These thin films could be assessed by transmission optical microscopy (OM, Olympus BX60) over a large sample area (~1 x 10^6 μm^2) for agglomerates statistics. ImagePro® image analysis software was used to measure the average diameter and area of the clusters in an attempt to characterize their dispersion level. Twenty different OM micrographs of different portions of the composite films (nominally 2 mm x 2 mm) were analyzed per composite type.

To assess the overall orientation of modifiers in the processed composites, wide-angle X-ray diffraction (Rigaku-MSC, Houston, TX) was conducted on the composites. A Cu target Kα radiation with a wavelength of 1.5406 Å (n = 3). The spectra were analyzed using Polar software version 2.6.7 from Stonybrook Technology and Applied Research (STAR). The X-ray source was operated at 45 kV and 0.65 mA, and the sample exposure time was 30 min.

4.2.5 Electrical properties

The DC in-plane volume electrical conductivity, σ (S/m), of the composites was measured using a Keithley 6517B High Resistance Meter connected to a Keithley 8002A Resistivity Test Fixture modified with external copper electrodes (ASTM D257). The conductivity was obtained from resistance measurements of die-cut specimens that were 12.5 mm wide, 2.5 mm thick and with lengths of ~ 20 mm. Silver paint was applied on the surfaces at each end of the samples and the in-plane resistance was measured. Likewise, the DC through-plane electrical conductivity was measured with the same meter, but using a Keithley 8009 Resistivity Test Fixture which sets the voltage across the thickness of the sample. The resistance measurements were performed using an alternating polarity DC voltage of ± 5V across the composites (n = 4).

The complex electrical permittivity of the composites was measured at 1 V_{rms} utilizing an Agilent 4291B RF Impedance/Material Analyzer. The Agilent 16453A Dielectric Material Test Fixture was connected to the impedance head and the measurements were carried out on 25 mm x 25 mm specimens (n = 4) with a thickness of ~2.5 mm. Prior to the measurements, the analyzer was calibrated utilizing an Agilent calibration kit. The analysis frequency range was 30 MHz to 1.5 GHz.

4.2.6 Electromagnetic shielding effectiveness (EM SE)

An Electro-Metrics EM-2107A coaxial test fixture was used to apply an electromagnetic plane-wave to the composite specimens (ASTM D4935). The electromagnetic shielding effectiveness (EM SE) was determined as ten times the negative logarithmic ratio of the measured transmitted power with the material present, $P_{T,W}$, to the transmitted power without the material present, $P_{T,WO}$ [ASTM D4935, 16, 17]. The accuracy of the fixture was checked by measuring a set of Mylar®-gold composite standard specimens. The EM-2107A test fixture was connected to an Agilent Technologies N5230A PNA Series Network Analyzer. For measuring EM SE, each circular composite specimen was aligned between the two halves of the test fixture and measured at frequencies from 30 MHz to 1.5 GHz. Two true replicates were tested (n = 2). The sample diameter was 133 mm, with a thickness of ~2.5-3.0 mm. To determine the shielding components for the nanocomposites, the scattering parameters, S_{11} and, S_{21} were measured for the load and reference specimens, as detailed in Appendix B [17].

4.3 Results and Discussion

4.3.1 Composite morphology

Figure 4.1 displays representative optical micrographs (OM) of the 1 vol% diluted composite films and their corresponding cluster size distributions. The PR-19 HT and MWNT HT diluted nanocomposites had similar average cluster diameters of

22.0±15.4 μm and 20.6±16.2 μm, respectively. Based on the resolution of OM, clusters smaller than 1 μm are considered as the dispersed phase [20, 21]. A quantitative measure of the relative non-dispersed phase has been established in prior literature studies [21] as the ratio of the total cluster area, A_C, to the total inspected area, A_{Tot}. For PR-19 HT and MWNT HT diluted nanocomposites, A_C/A_{Tot} ratios were 0.433±0.033 and 0.428±0.032, respectively. These values indicate that in both nanocomposites a similar dispersion level was reached. In our previous study, optical micrographs of ~10 μm thin nanocomposite films, made of the same nanomodifier types, identified cluster sizes under 50 μm, which is about the same size of the clusters before melt-mixing [15].

Representative SEM micrographs of the cross-section of the nanocomposites are presented in **Figure 4.2**. In contrast to OM, scanning electron microscopy revealed no major clusters. This level of dispersion is consistent with microstructure observations made in other literature studies in which the localized microstructure displays no clusters, but in a larger length-scale, such that provided by optical microscopy, the composites exhibit identifiable percolating clusters [20, 22]

Figures 4.3 (a)-(d) display representative wide-angle x-ray diffractograms (2θ plots) of the composites and the corresponding azimuthal scans. In the composites, the graphitic peak associated with (002) layer planes of carbon modifiers appears at approximately 26°, whereas the (110) and (200) peaks corresponding to the orthorhombic crystallites of the LLDPE matrix appear at about 21.4° and 23.7°, respectively. Consistent with the composition, the relative intensity of the graphitic peak is higher in

the composites at 40 vol% carbon modifier, whereas the (110) peak for polyethylene is stronger for the composites containing larger content of PE (i.e., only 10 vol% carbon modifier). It is also evident from the azimuthal distribution of the graphitic (002) peak that there is no preferred angle of orientation for any of the carbon modifiers in the composites. Thus, a predominantly random orientation of the modifiers was observed in the plane.

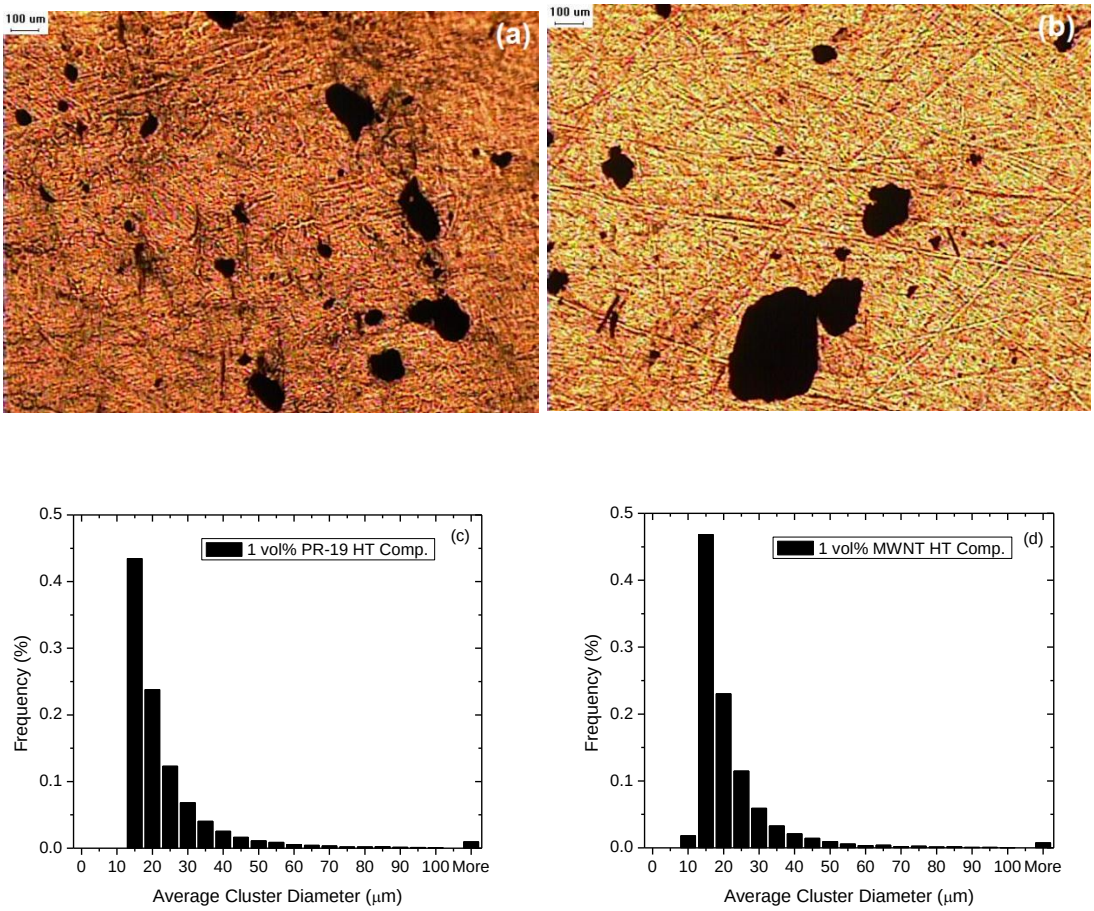

Figure 4.1. Representative transmission optical micrographs of 100-μm thick nanocomposite films at 1 vol% diluted from the nanocomposites at 40 vol%, and their respective average cluster diameter distributions obtained by image analysis. (a, c) PR-19 HT nanocomposites and (b, d) MWNT HT nanocomposites.

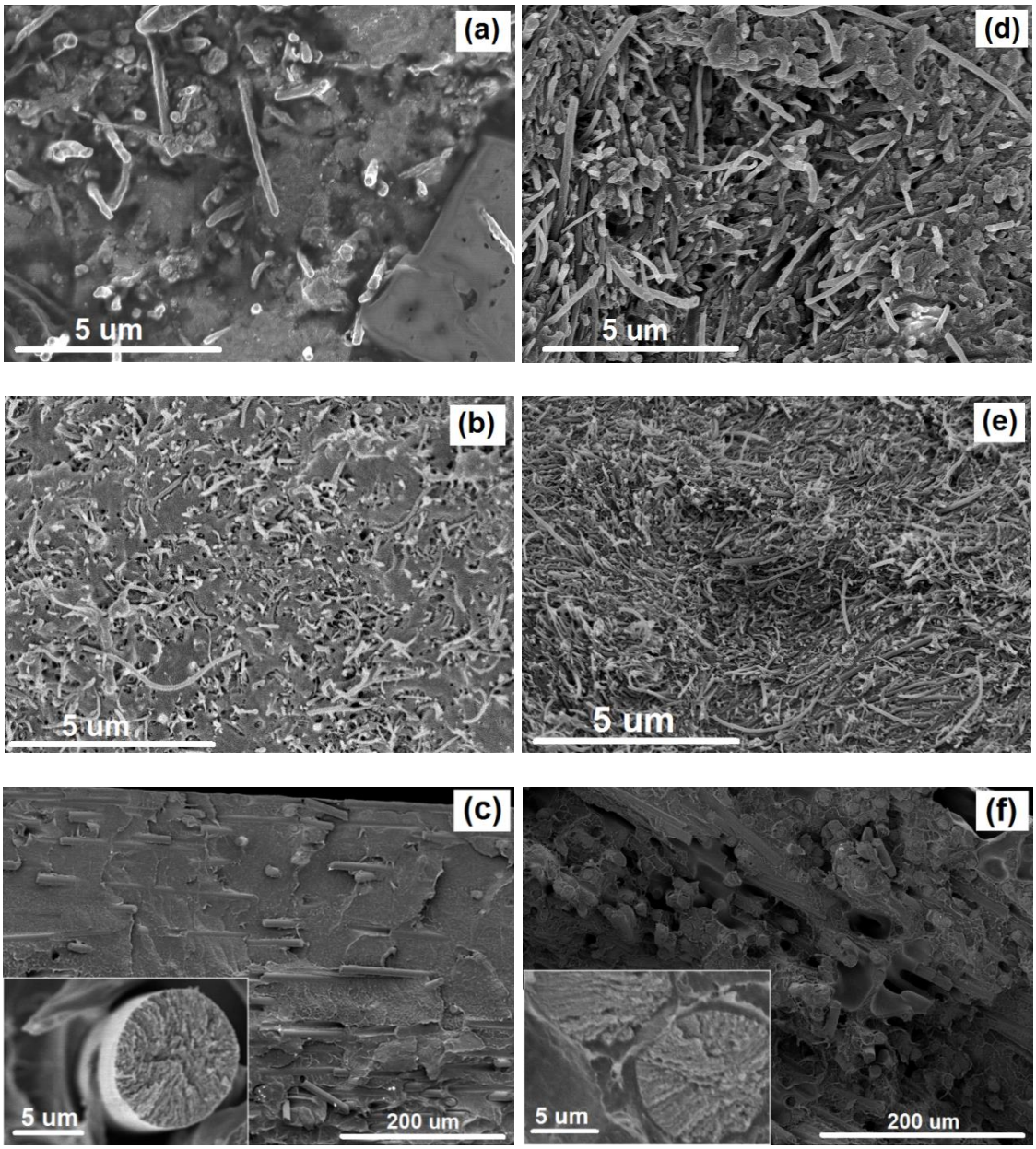

Figure 4.2. Representative scanning electron micrographs (SEM) of composites at 10 vol% (a) PR-19 HT, (b) MWNT HT (c) P-55, and of those at 40 vol% (d) PR-19 HT, (e) MWNT HT (f) P-55. Insets display the microstructure at higher magnification.

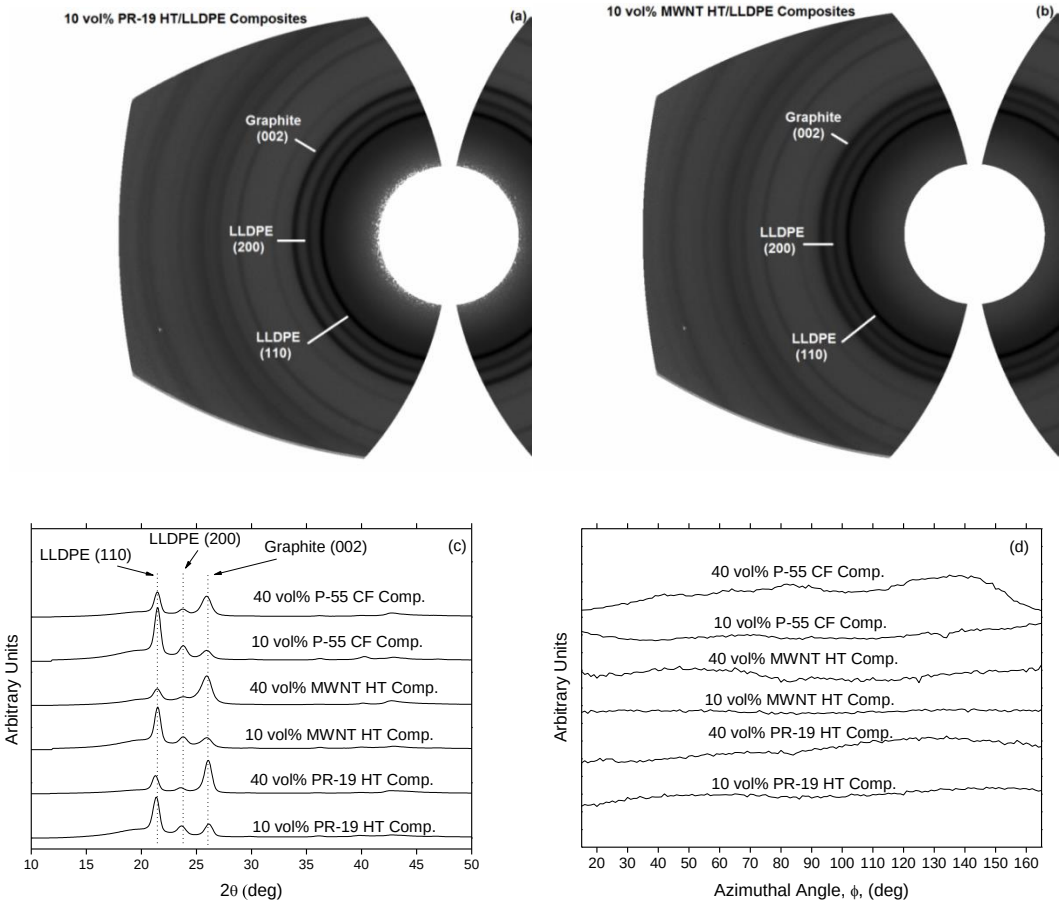

Figure 4.3. Representative wide-angle X-ray diffractograms of (a) the PR-19 HT and (b) MWNT HT nanocomposites at 10 vol%. X-ray diffractograms of the composites as function of (c) the 2θ and (d) azimuthal, ϕ, angles. Curves were shifted vertically along intensity axis to avoid overlap.

4.3.2 Nanocomposite rheology

Figure 4.4 contains the viscosity measurements of the nanocomposites as a function of the true shear rates corrected by the Weissenberg-Rabinowitsch equation, together with the shear viscosity of the pure LLDPE [23]. The measurements conducted by rotational shear viscosity at 190°C at a shear rate of 1 s^{-1} exhibited a steady shear viscosity of 7268±255 Pa.s for pure LLDPE, and 17248±1031 Pa.s and 18405±832 Pa.s, for PR-19 HT- and MWNT HT-based nanocomposites, respectively. This means that the viscosity of these composite formulations is about 2.5 times higher than that of its pure matrix at 1 s^{-1}. Nonetheless, the capillary rheological measurements confirm that, at an apparent shear rate of 10^4 s^{-1}, the LLDPE viscosity was 33 Pa.s, whereas that of the PR-19 HT- and MWNT HT-based nanocomposites was only about 36 Pa.s. These results confirm that at 10 vol%, the nanocomposites are processable because typical polymer processing operations such as extrusion and injection molding are feasible at such viscosity levels.

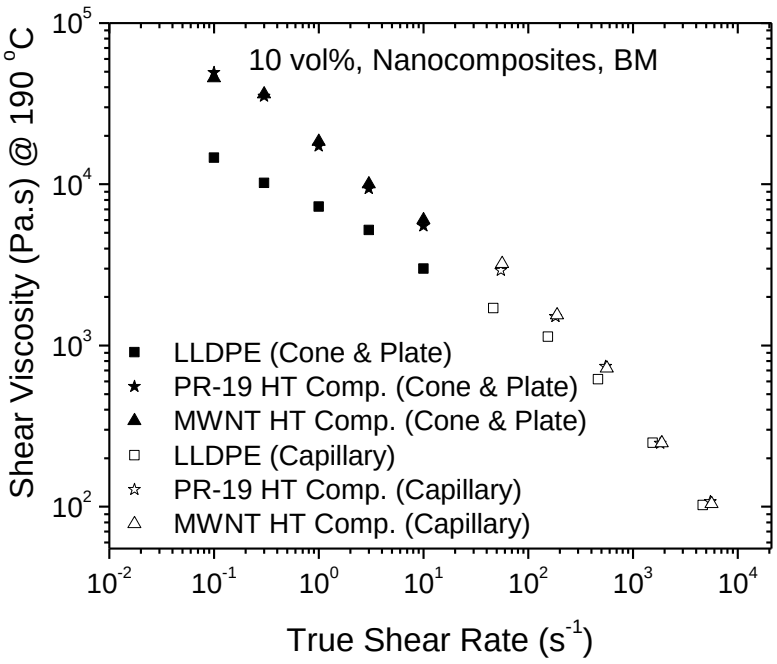

Figure 4.4. Steady shear viscosity of nanocomposites (BM, 10 vol%, 190°C and 20 rpm for 2 min) at 190°C.

4.3.3 Composite electrical properties

Table 4.1 summarizes the DC in-plane and through-plane conductivities of the different composites (replicates, n = 4 in all cases). At 40 vol%, the nanocomposites displayed in-plane DC conductivity much greater than that at 10 vol%; the in-plane values were an order of magnitude higher, whereas the through-plane values were larger by a factor of 2-3. The through-plane conductivity values were significantly smaller than those of their corresponding in-plane values (about 3 orders of magnitude), which means

that the composites displayed anisotropic conductivity. The composites were electrically percolated systems when compared with a conductivity of $7.0\pm1.1\text{x}10^{-15}$ S/m for pure LLDPE, which is 15 orders of magnitude lower than that of the composites.

At the percolation threshold (e.g., 10^{-5} to 10^{-2} S/m), although the conductivity of the composite is much higher than that of the pure matrix (e.g., 10^{-17} to 10^{-15} S/m), it is typically not high enough for electromagnetic shielding purposes. Therefore, to attain EM SE, it is necessary to increase filler concentrations significantly beyond the percolation threshold. Unfortunately, the higher concentrations are often limited to such levels where the processability and mechanical properties can still be retained. Thus, the selection of 10 vol% modifier content used in this study was based on the Chapter 2, whereas the 40 vol% was chosen for exploring the upper, practical limits of shielding performance.

Table 4.1. DC in-plane and through-plane volume conductivity of composites at 25°C and ~ 50 % relative humidity. Ranges represent 95% confidence intervals.

Modifier	**DC in-plane volume conductivity (S/m)**		**DC through-plane volume conductivity (S/m)**	
	10 vol%	**40 vol%**	**10 vol%**	**40 vol%**
PR-19 HT	20.4±3.3	344.8±81.3	$1.0\pm0.9\text{x}10^{-3}$	**$3.3\pm0.2\text{x}10^{-3}$**
MWNT HT	33.5±5.6	250.0±59.9	$1.2\pm0.5\text{x}10^{-3}$	**$2.0\pm0.4\text{x}10^{-3}$**
P-55	5.0±1.8	6.9±1.5	$2.1\pm1.9\text{x}10^{-4}$	**$4.7\pm3.3\text{x}10^{-4}$**

The complex electrical permittivity of the nanocomposites ($\varepsilon = \varepsilon' - j\varepsilon''$) is displayed in **Figure 4.5**, where $\varepsilon'/\varepsilon_0$ represents the real relative permittivity (or dielectric storage), and $\varepsilon''/\varepsilon_0$ the imaginary relative permittivity (or dielectric loss). The permittivity of vacuum ε_0 is set at 8.85418×10^{-12} F/m. The real and imaginary permittivity of the nanocomposites displayed a generally decreasing behavior with respect to frequency. At 10 vol%, the permittivity of PR-19 HT nanocomposites decreased an order of magnitude from 100 MHz to 1.5 GHz. The MWNT HT nanocomposites exhibited an overall permittivity of (175±60)-(93±34)j at 100 MHz, decreasing ten-fold at 1.5 GHz. In contrast, the permittivity of P-55 composites showed less frequency dependency. Likewise, for the composites at 40 vol%, the permittivity of PR-19 HT composites rapidly decreased from (504±155)-(4755±1200)j at 100 MHz to only (6±1)-(13±2)j at 1.5 GHz, and for the MWNT HT nanocomposites from (135±44)-(2595±800)j at 100 MHz to (7±2)-(15±6)j at 1.5 GHz. However, once again, the P-55 composites were relatively less frequency dependent at about (80±25)-(76±32)j. Thus, the most conductive composites also displayed the highest dielectric losses. This is important because the DC as well as the AC "lossy" effects contribute to the entropic characteristics of the material such as its electromagnetic shielding.

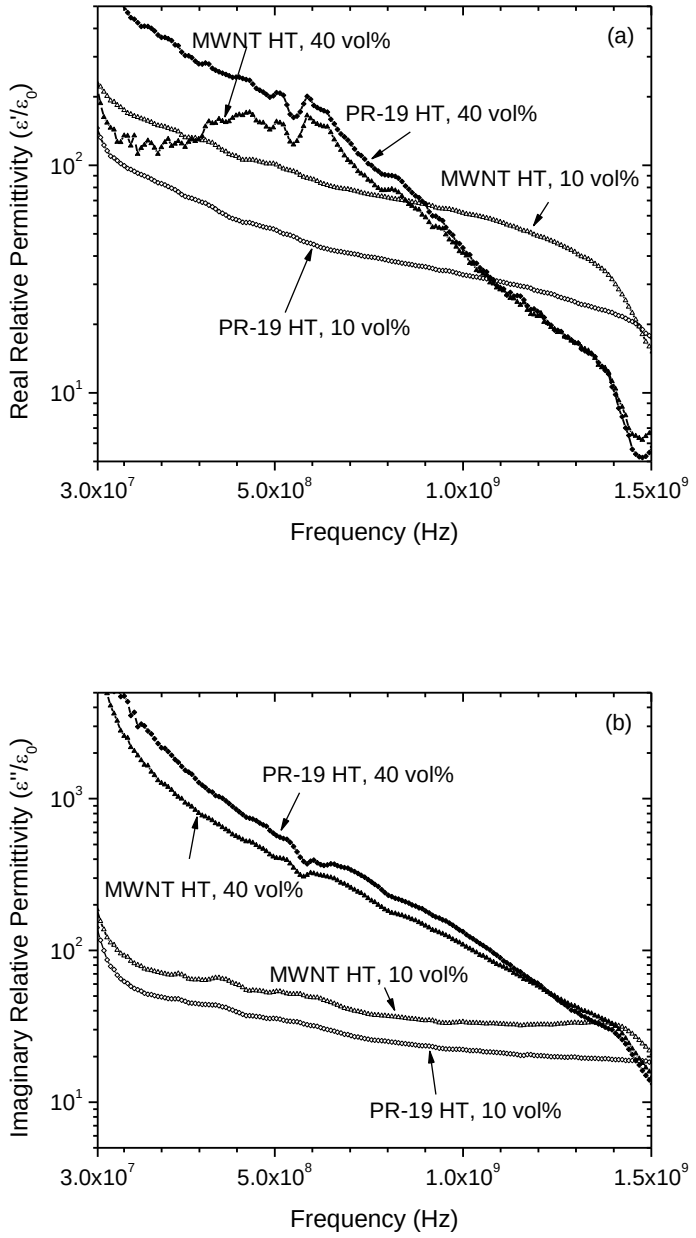

Figure 4.5. Representative spectra of the AC permittivity of nanocomposites: (a) real relative permittivity of nanocomposites at 10 vol% and 40 vol%, and (b) imaginary relative permittivity at 10 vol% and 40 vol%.

4.3.4 Electromagnetic shielding effectiveness (EM SE)

Figure 4.6 displays the EM SE for (a) 10 vol% and (b) 40 vol% composites. At 10 vol%, PR-19 HT nanocomposites displayed 24.7±0.3 dB of total shielding at 1.5 GHz, whereas MWNT HT nanocomposites displayed a slightly larger value of 25.3±0.2 dB. In contrast, P-55 composites provided only 12.2±0.1 dB of shielding. At 40 vol%, PR-19 HT, MWNT HT and P-55 composites displayed EM SE values of 68.2±0.8, 55.2±1.1 and 16.4±0.4 dB, respectively. These EM SE results are consistent with their corresponding conductivity and permittivity measurements; the composites that displayed the highest EM SE were those with the highest dielectric loss and conductivity.

The absorptive and reflective shielding components of the composites obtained from the EM SE measurements are displayed in **Figure 4.7**. The reflective components of both 10 vol% nanocomposites were about 7 dB, whereas the absorptive components were approximately 15 dB. For P-55 composites, the absorptive component is significantly lower (than that of its nanocounterparts) and comparable to the reflective one (about 5-6 dB). At 40 vol%, nanocomposites had a reflective component of ~10 dB and absorption of ~40 dB; P-55 composites had a reflection of ~7 dB and absorption of ~8 dB. Thus, for all nanocomposites, the absorptive component was dominant.

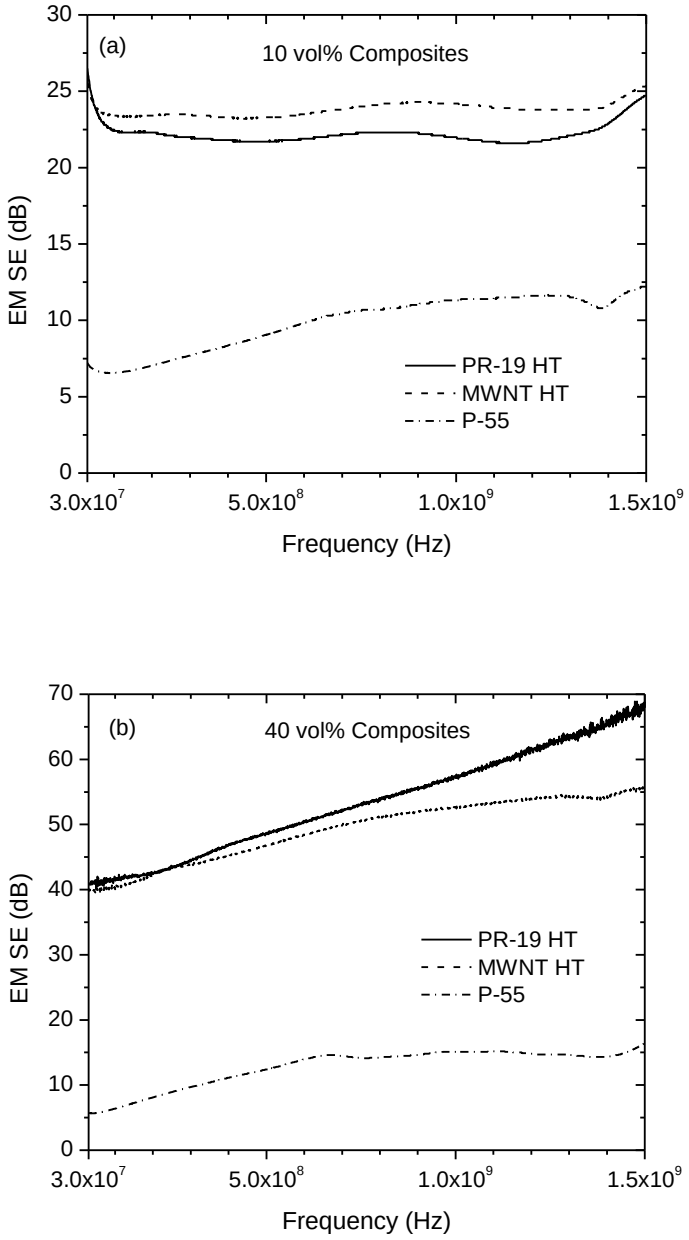

Figure 4.6. Electromagnetic shielding effectiveness (EM SE) of representative (a) 10 vol% and (b) 40 vol% composites, over the frequency range of 30 MHz to 1.5 GHz.

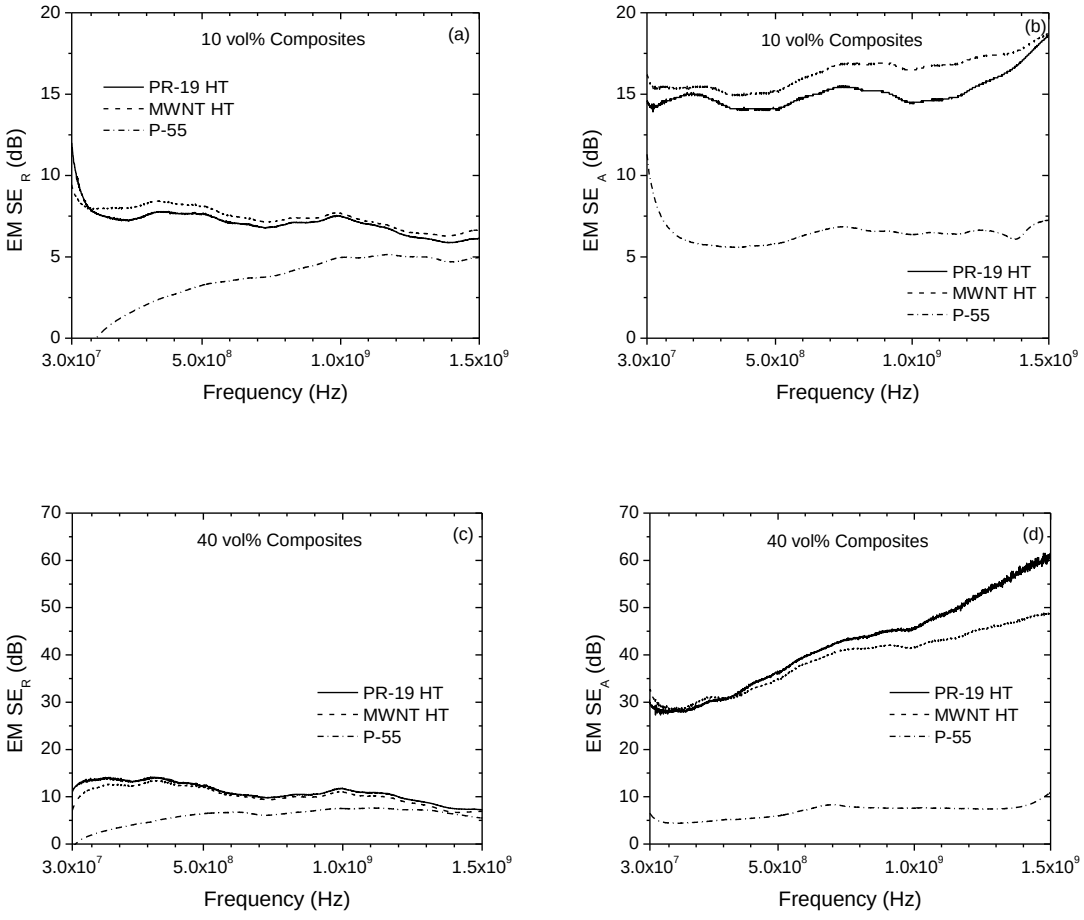

Figure 4.7. Measured reflective (EM SE_R) and absorptive (EM SE_A) components of shielding for (a, b) 10 vol% and (c, d) 40 vol% composites.

4.3.5 Prediction of the electromagnetic shielding

The plane wave EM SE provided by polymer nanocomposites cannot be accurately predicted from the assumption that the material is purely conductive or purely dielectric. For non-magnetic, linear, isotropic, materials of intermediate conductivity, one must account for the fact that the AC electrical transport has two components: (1) the free electron/hole transport brought about by the conductivity, $\sigma = \sigma' - j\sigma''$, which is the predominant component, and (2) the bound electron dielectric displacement implied in the permittivity, $\varepsilon = \varepsilon' - j\varepsilon''$ [2]. The real component of permittivity, ε', is related to the level of polarization that the applied electric field confers to the molecules and atoms, whereas the imaginary component, ε'', to losses associated with the dielectric damping that the bound electrons in the dipoles undergo due to the varying electric field at an angular frequency, ω [24]. Hence, the current density, J, set by an electric field, E, will be $J = j\omega\left(\varepsilon' - j\varepsilon'' - j\frac{\sigma'}{\omega} + \frac{\sigma''}{\omega}\right)E$ [2]. However, the imaginary conductivity, σ'', is negligible up to the microwave range (freq. < 300 GHz), which makes $\sigma' = \sigma_{DC} = \sigma$ [2]. Thus, $J = j\omega\left(\varepsilon' - j\left(\varepsilon'' + \frac{\sigma}{\omega}\right)\right)E$, where the term $\left(\varepsilon'' + \frac{\sigma}{\omega}\right)$ scales with that of the "effective conductivity", $(\sigma + \omega\varepsilon'')$, which combines the conductive and dielectric losses [25]. Moreover, the intrinsic impedance, η, and propagation constant, γ, of an electromagnetic wave are determined by the material properties through which it travels. Thus,

$$\eta = \sqrt{\frac{\mu}{\varepsilon' - \left(\varepsilon'' + \frac{\sigma}{\omega}\right)j}} \tag{4.1}$$

$$\gamma = \alpha + j\beta \tag{4.2}$$

where α and β are defined as the attenuation and phase constants, respectively [1]. For non-magnetic materials, the magnetic permeability, μ, is that of the vacuum at $\mu = \mu_0 =$ 4π x 10^{-7} H/m. For a generally lossy medium, the attenuation constant can be analytically derived [26]:

$$\alpha = \omega \sqrt{\frac{\mu\varepsilon'}{2}\left(\sqrt{1 + \left[\frac{\left(\frac{\sigma}{\omega} + \varepsilon''\right)}{\varepsilon'}\right]^2} - 1\right)} \tag{4.3}$$

Figure 4.8 is a schematic representation of how the plane wave, in terms of electric field, interacts with an isotropic conductive medium with finite thickness, t. The incident field, E_o, travels in air in which the intrinsic impedance is basically that of vacuum $\eta_o = 120\pi\ \Omega$. When the field strikes the surface, the first reflection, E_{R_1}, occurs due to the mismatch in impedance, because the wave impedance becomes η. Part of this field is transmitted through the thickness of the specimen, t, and as it travels, it is attenuated, $e^{-\gamma t}$ [1]. When the field reaches the second surface, a similar phenomenon takes place, leading to the transmitted field, E_{T_1}. The part that is reflected back into the material experiences a series of subsequent partial reflections and transmissions while being attenuated along the path, and constitutes the multiple reflection loss [1]. Thus, the total transmitted field, E_T, and total reflected field, E_R, are:

$$E_T = \sum_{i=1}^{\infty} E_{T_i} = \frac{E_{T_1}}{1-\left(\Gamma_\eta e^{-\gamma t}\right)^2} = \frac{E_o T_\eta\, e^{-\gamma t} T_{\eta_o}}{1-\left(\Gamma_\eta e^{-\gamma t}\right)^2} \tag{4.4}$$

$$E_R = \sum_{i=1}^{\infty} E_{R_i} = E_{R_1} + \frac{E_{R_2}}{1-(\Gamma_\eta e^{-\gamma t})^2} = E_o\Gamma_{\eta_o} + \frac{E_o T_\eta\, e^{-\gamma t}\Gamma_\eta e^{-\gamma t} T_{\eta_o}}{1-(\Gamma_\eta e^{-\gamma t})^2} \qquad (4.5)$$

where, $T_\eta = \frac{2\eta}{\eta_o+\eta}$ and $\Gamma_\eta = \frac{\eta-\eta_o}{\eta+\eta_o}$ are respectively the transmission and reflection coefficients for the plane wave traveling in the vacuum η_o and striking on a surface of impedance η; whilst, $T_{\eta_o} = \frac{2\eta_o}{\eta_o+\eta}$ and $\Gamma_{\eta_o} = \frac{\eta_o-\eta}{\eta_o+\eta}$ are respectively the transmission and reflection coefficients for the plane wave traveling in the material medium of impedance η and re-entering a vacuum η_o [1].

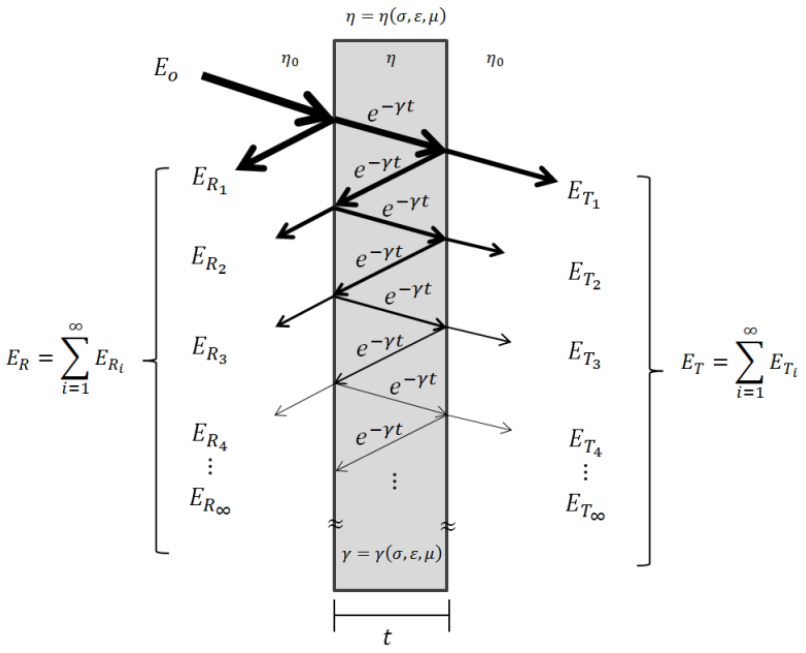

Figure 4.8. Schematic representation of the shielding mechanisms in terms of the electric field E in a generally lossy isotropic specimen. For the sake of clarity, the incident plane wave, which propogates perpendicular to the sample surface, has been depicted with oblique incidence, so that the multiple reflections can be readily represented.

The wave power density is proportional to the square of the electric field, i.e., $P \propto E^2$ [1]. The transmittance, T, and reflectance, R, are defined as the ratio of the transmitted power density, P_T, and reflected power density, P_R, to that of the incident power density, P_o [1, 17]:

$$T = \left|\frac{P_T}{P_0}\right| = \left|\frac{E_T}{E_0}\right|^2 \tag{4.6}$$

$$R = \left|\frac{P_R}{P_0}\right| = \left|\frac{E_R}{E_0}\right|^2 \tag{4.7}$$

Then, dividing equations (4.4) and (4.5) by the incident electric field E_o and using the transmission and reflection coefficient substitutions:

$$\frac{E_T}{E_o} = \frac{T_\eta\, e^{-\gamma t} T_{\eta_o}}{1-\left(\Gamma_\eta e^{-\gamma t}\right)^2} = \frac{\frac{2\eta}{\eta_o+\eta}\, e^{-\gamma t} \frac{2\eta_o}{\eta_o+\eta}}{1-\left(\frac{\eta-\eta_o}{\eta+\eta_o}\right)^2 e^{-2\gamma t}} \tag{4.8}$$

$$\frac{E_R}{E_o} = \Gamma_{\eta_o} + \frac{T_\eta\, e^{-\gamma t} \Gamma_\eta e^{-\gamma t} T_{\eta_o}}{1-\left(\Gamma_\eta e^{-\gamma t}\right)^2} = \frac{\eta_o-\eta}{\eta_o+\eta} + \frac{\frac{2\eta}{\eta_o+\eta} e^{-\gamma t} \frac{\eta-\eta_o}{\eta+\eta_o} e^{-\gamma t} \frac{2\eta_o}{\eta_o+\eta}}{1-\left(\frac{\eta-\eta_o}{\eta+\eta_o}\right)^2 e^{-2\gamma t}} \tag{4.9}$$

Based on the definitions of total shielding $EM\ SE_{dB} = -10 \log T$ and reflective shielding $EM\ SE_{R,\,dB} = -10 \log(1 - R)$, the following expressions are obtained for the total and reflective shielding effectiveness:

$$EM\ SE_{dB} = -10 \log \left| \left\{ \frac{\frac{4\eta\eta_o}{(\eta_o+\eta)^2} e^{-\gamma t}}{1-\left(\frac{\eta-\eta_o}{\eta+\eta_o}\right)^2 e^{-2\gamma t}} \right\}^2 \right| \tag{4.10}$$

$$EM\ SE_{R,\,dB} = -10\log\left|1-\left\{\frac{\eta_o-\eta}{\eta_o+\eta}+\frac{\frac{4\eta\eta_o}{(\eta_o+\eta)^2}e^{-2\gamma t}\frac{\eta-\eta_o}{\eta+\eta_o}}{1-\left(\frac{\eta-\eta_o}{\eta+\eta_o}\right)^2 e^{-2\gamma t}}\right\}^2\right| \tag{4.11}$$

The absorptive component of shielding is readily obtained as $EM\ SE_{A,\,dB} = EM\ SE_{dB} - EM\ SE_{R,\,dB}$. Moreover, since only magnitudes are needed in these calculations, and $|e^{Z}| = |e^{a+bj}| = |e^{a}e^{bj}| = e^{a}$, the terms $|e^{-2\gamma t}|$ and $|e^{-\gamma t}|$ can be substituted by $|e^{-2\alpha t}|$ and $|e^{-\alpha t}|$, respectively. Therefore, equations (4.10) and (4.11) along with the intrinsic impedance η (eqn. 4.1) and attenuation constant α (eqn. 4.3) expressions can be used to estimate the shielding of an intermediately lossy and isotropic material of thickness, t, by knowing only its electrical conductivity, σ, and complex permittivity, ε, over the frequency range of interest.

Even though the nanocomposites developed in this study have different in-plane and through-plane properties, they present fairly isotropic properties in the plane due to a random orientation of the nanomodifiers. In addition, because the in-plane conductivity is the one that interacts with the electromagnetic plane-wave, they can be modeled as 2-D quasi-isotropic materials [27]. Thus, the theoretical background previously discussed for lossy isotropic materials can be used to estimate the shielding of nanocomposites from their in-plane composite electrical properties.

Figure 4.9 displays the experimental EM SE and EM SE_R of the nanocomposites at 10 vol% as compared with the predictions based on equations (4.1), (4.3), (4.10) and (4.11). The inputs for the model are the previously reported average in-plane

conductivity, permittivity and thickness of the nanocomposite specimens. Thus, at 1 GHz, EM SE values of 22.0±2.2 dB and 24.2±2.3 dB were measured for PR-19 HT and MWNT HT nanocomposites at 10 vol%. The corresponding predicted values were consistent with the measured ones. Similarly, the reflective components of shielding were respectively about 7.5 dB and 7.7 dB for PR-19 HT and MWNT HT nanocomposites at 1 GHz, as compared with estimated values of 6.2 dB for PR-19 HT and 7.2 dB for MWNT HT nanocomposites. Interestingly, when using the through-plane conductivity as input in the modeling equations, EM SE values of only 2.9 dB and 3.5 dB are predicted for PR-19 HT and MWNT HT nanocomposites, respectively. This demonstrates that, due to the plane-wave propagation of the electric field, the conductivity that interacts with such a field is that parallel to the plane (i.e., in-plane).

Figure 4.10 compares the experimental vs. the predicted EM SE and EM SE_R values for the nanocomposites at 40 vol%. EM SE values of 58.0±4.8 dB and 53.4±3.5 dB were respectively measured for PR-19 HT and MWNT HT nanocomposites at 1 GHz. The predicted values were 57.2 dB and 52.3 dB, respectively. PR-19 HT nanocomposites displayed a predicted EM SE_R value of 12.8 dB, which is consistent with the actual EM SE_R. For 40 vol% MWNT HT nanocomposites, values of reflective EM SE of 10.6±4.7 dB and 12.3 dB were obtained experimentally and theoretically. Thus, based on independent measurements of in-plane conductivity and permittivity, the predicted EM SE values and shielding components were consistent with the experimental values.

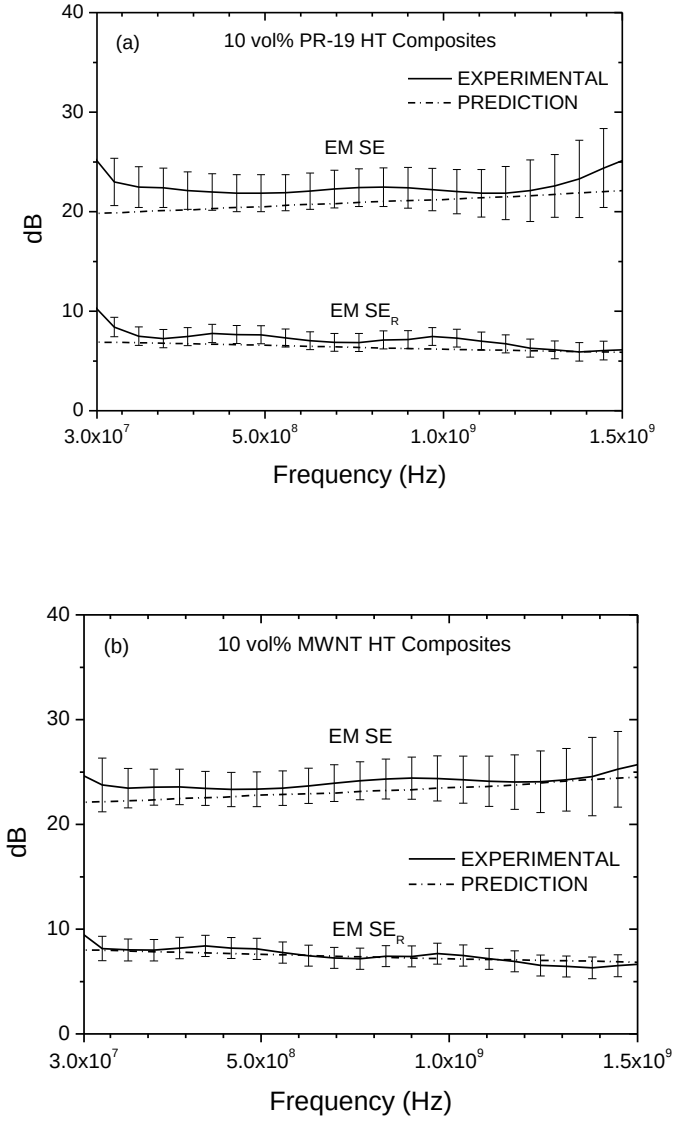

Figure 4.9. Comparison of the experimental total and reflective EM SE vs. the theoretical prediction from the experimental electrical transport properties of the 10 vol% a) PR-19 HT and b) MWNT HT nanocomposites. Error bars calculated based on two true replicates.

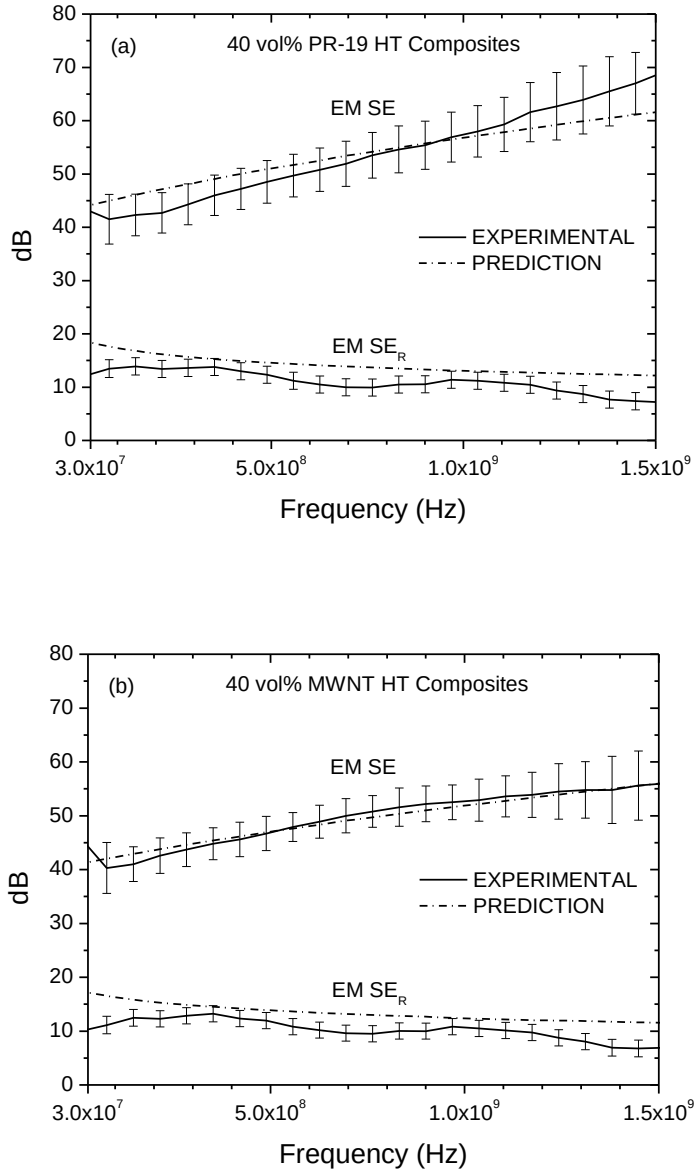

Figure 4.10. Comparison of the experimental total and reflective EM SE vs. the theoretical prediction from the experimental electrical transport properties of the 40 vol% a) PR-19 HT and b) MWNT HT nanocomposites. Error bars calculated based on two true replicates

Finally, the tensile properties of the nanocomposites were assessed using the ASTM D638 Type V technique (die-cut, dogbone-shaped specimens of 25 mm gauge-length, 3 mm width and 1 mm thickness) in an ATS Universal 900 tensile tester at a cross-head speed of 25 mm/min. At 40 vol%, PR-19 HT modified nanocomposites displayed a tensile modulus of 1,256±101 MPa, tensile strength of 3.5±0.4 MPa and strain-to-failure of 1.5±0.3 % (n = 6 in all cases). Likewise, at 40 vol%, MWNT HT nanocomposites displayed a tensile modulus of 1,177±95 MPa, strength of 4.1±0.7 MPa and strain-to-failure of 2.0±0.4 % (n = 6). In comparison, pure LLDPE has a modulus of 325±85 MPa, strength of 30±5 MPa, and strain-to failure of 685±105% (n = 6). As expected in a highly concentrated dispersion of percolated solids in a composite, the modulus increased by about 400%, but the strength decreased by about 87 % and the ductility was reduced by over 99% of that of the LLDPE matrix. At an intermediate concentration of 10 vol%, PR-19 HT nanocomposites exhibited intermediate properties: a modulus of 683±105 MPa, strength of 16.0±2.5 MPa and strain-to-failure of 128±49 % (n = 6). Similarly, at 10 vol%, MWNT HT nanocomposites possessed a modulus of 696±110 MPa, strength of 17.7±1.6 MPa and strain-to-failure of 114±43 % (n = 6). Thus, as compared with pure LLDPE, the overall modulus of the 10 vol% nanocomposites was about twice, and they retained about 50 % and 20% of the LLDPE strength and ductility, respectively. These values, coupled with EM SE results presented earlier, represent a fairly wide range of properties attainable within the conducting regime of carbon nanomodifier modified polyethylene composites.

4.4 Conclusions

Over a frequency range of 30 MHz to 1.5 GHz, LLDPE-based nanocomposites containing 10 vol% of in-plane randomly oriented carbon nanotubes/nanofibers exhibited shielding effectiveness values over 20 dB, whereas the very-highly filled 40 vol% nanocomposites displayed EM SE values as high as 68 dB and 55 dB for PR-19 HT and MWNT HT nanocomposites, respectively. Thus, graphitic nanomodifier-based LLDPE composites can provide an EM SE performance of up to 25 dB/mm. Both types of nanocomposites displayed a predominantly absorptive shielding component. In contrast, short-carbon-fiber composites showed significantly lower EM SE, and the reflective component was similar to absorption. Modeling of the shielding mechanisms in generally lossy materials was used to predict the EM SE and its components from the electrical and dielectric properties of the nanocomposites. For the studied frequency range, predictions were consistent with the experimental EM SE values. Both types of nanocomposites hold potential promise as alternative materials for electromagnetic shielding applications in the VHF and UHF bands.

4.5 References

1. Paul CR. Introduction to Electromagnetic Compatibility. United States of America: John Wiley & Sons, Inc., 1992.

2. Ramo S, Whinnery JR, Van Duzer T. Fields and Waves in Communication Electronics. United States of America: John Wiley & Sons, Inc., 1984.

3. Al-Saleh MH, Sundararaj U. Electrically conductive carbon nanofiber/polyethylene composite: effect of melt mixing conditions. Polym Adv Technol 2011;22:246-253.

4. Al-Saleh MH, Sundararaj U. Electromagnetic interference shielding mechanisms of CNT/polymer composites. Carbon 2009;47:1738-1746.

5. Nanni F, Valentini M. Electromagnetic properties of polymer-carbon nanotube composites. In: McNally T, Pötschke P, editors. Polymer-carbon nanotube composites, Preparation, properties and applications. Cambridge, UK: Woodhead Publishing, 2011, pp. 329-346.

6. Al-Saleh MH, Gelves GA, Sundararaj U. Copper nanowire/polystyrene nanocomposites: Lower percolation threshold and higher EMI shielding. Composites Part A 2011;42:92-97.

7. Lu G, Li X, Jiang H. Electrical and Shielding Properties of ABS Resin Filled with Nickel-coated Carbon Fibers. Compos Sci Technol 1996;56:193-200.

8. Wang SF, Ogale AA. Continuum space simulation and experimental characterization of electrical percolation behavior of particulate composites. Compos Sci Technol 1993;46:93-103.

9. Dani A, Ogale AA. Percolation in Short-fiber Composites: Cluster Statistics and Critical Exponents. Compos Sci Technol 1997; 57:1355-1361.

10. Xiao KQ, Zhang LC, Zarudi I. Mechanical and rheological properties of carbon nanotube reinforced polyethylene composites. Compos Sci Technol 2007;67:177-182.

11. Das NC, Khastgir D, Chaki TK, Chakraborty A. Electromagnetic interference shielding effectiveness of carbon black and carbon fibre filled EVA and NR based composites. Composites Part A 2000;31:1069–1081.

12. Zhou P, Yu W, Zhou C, Liu F, Hou L, Wang J. Morphology and Electrical Properties of Carbon Black Filled LLDPE/EMA Composites. J Appl Polym Sci 2007;103:487–492.

13. King JA, Johnson BA, Via MD, Ciarkowski CJ. Effects of carbon fillers in thermally conductive polypropylene based resins. Polym Compos 2010;31:497-506.

14. Yang S, Lozano K, Lomeli A, Foltz HD, Jones R. Electromagnetic interference shielding effectiveness of carbon nanofiber/LCP composites. Composites Part A 2005;36:691-697.

15. Villacorta BS, Ogale AA. Carbon Nanoparticle-based Flexible LLDPE Composites for Enhanced Electromagnetic Shielding Effectiveness. In: Haghi AK, Thomas S, Shanks R, Joy J, editors. Recent trends in micro and nanostructured polymer systems. Canada: Apple Academic Press, 2013.

16. Janda NB, Keith JM, King JA, Perger WF, Oxby TJ. Shielding-Effectiveness Modeling of Carbon-Fiber/Nylon-6,6 Composites. J Appl Polym Sci 2005;96:62-69.

17. Villacorta BS, Ogale AA, Hubing TH. Effect of Heat Treatment of Carbon Nanofibers on the Electromagnetic Shielding Effectiveness of Linear Low Density Polyethylene Nanocomposites. Polym Eng Sci 2013;53:417-423.

18. Callister WD, Rethwisch DG. Material Science and Engineering an Introduction. United States: John Wiley & Sons, Inc. Eighth Edition, 2010.

19. Villacorta BS, Hubing TH, Ogale AA. Influence of Composite Electrical Properties on the VHF-UHF Electromagnetic Shielding Characteristics of Polyethylene-Carbon Nanoparticle Composites. Compos Sci Technol DOI: 10.1016/j.compscitech.2013.10.003.

20. Pegel S, Villmow T, Potschke P. Quantification of dispersion and distribution of carbon nanotubes in polymer composites using microscopy techniques. In: McNally T, Pötschke P, editors. Polymer-carbon nanotube composites, Preparation, properties and applications. Cambridge, UK: Woodhead Publishing, 2011, pp. 265-294.

21. Kasaliwal GR, Villmow T, Pegel S, Potschke P. Influence of material and processing parameters on carbon nanotube dispersion in polymer melts. In: McNally T, Pötschke P, editors. Polymer-carbon nanotube composites, Preparation, properties and applications. Cambridge, UK: Woodhead Publishing, 2011, pp. 92-132.

22. Cardoso P, Silva J, Klosterman D, Covas JA, van Hattum FWJ, Simoes R, Lanceros-Mendez S. The role of disorder on the AC and DC electrical conductivity of vapour grown carbon nanofibre/epoxy composites. Compos Sci Technol 2012;72:243-247.

23. Makosco CW. Rheology: Principles, Measurements, and Applications. United States of America: Wiley-VCH, Inc., 1994.

24. Morcon M, Simon G. Polyolefin-carbon nanotube composites. In: McNally T, Pötschke P, editors. Polymer-carbon nanotube composites, Preparation, properties and applications. Cambridge, UK: Woodhead Publishing, 2011, pp. 511-544.

25. Pozar DM. Microwave engineering. United States of America: Addison-Wesley Publishing Company, Inc., 1990.

26. Villacorta BS, Hubing TH. Analysis of the Electromagnetic Shielding Mechanisms of Plane Waves in Generally Lossy Materials. Clemson Vehicular Electronics Laboratory Technical Report: CVEL-13-044, 2013.

27. Matumura K, Kagawa Y, Baba K. Light transmitting electromagnetic wave shielding composite materials using electromagnetic wave polarizing effect. J Appl Phys 2007;101:014912.

CHAPTER 5

EFFECT OF ELECTRICAL ANISOTROPY ON THE POLARIZED-WAVE ELECTROMAGNETIC SHIELDING OF CARBON NANOMODIFER-BASED LINEAR LOW DENSITY POLYETHYLENE COMPOSITES

5.1 Introduction

In prior Chapters 2-4, the effects of graphitic crystallinity and modifier morphology on the EM SE of LLDPE-based nanocomposites were studied for a large range of volume fractions of carbon nanomodifiers. In addition, modeling of the shielding mechanisms in generally lossy materials was conducted in Chapter 4 [8]. It was found that, when shielding an electromagnetic plane wave, the electric field interacts with the in-plane conductive and dielectric lossy properties of the material, and in particular with its in-plane conductivity [1-8]. Thus, this in-plane conductivity was found to be virtually brought about by the random in-plane orientation of the nanomodifiers in the nanocomposites, which indicates that modifier orientation is another important variable [8].

Many industrial polymer processing techniques such as cast-film, blown-film and injection molding induce different levels of modifier orientation in composites [9-11]. Due to the possibility of producing composites with very thin-walls, such as films and micro-injection molded parts (as thin as 25 μm), the study of the shielding performance

of composites made of oriented nanomodifiers (diameter < 0.5 μm) is relevant for thin applications [12]. The orientation effect of carbon-based conductive modifiers such as nanofibers, nanotubes and fibers in polymer composites on their electrical properties have been previously reported [9, 11, 13 and 14]. Modifier alignment produces an anisotropic electrical network in the composites, which typically reduce their EM SE [15]. However, when shielding polarized electromagnetic waves, the electrically anisotropic composites can also display anisotropic EM SE behavior, which may be attractive for novel filtering and compatibility applications such as mode-selective waveguide structures or antenna radomes. Therefore, the electromagnetic shielding effectiveness of polarized waves in the VHF-UHF frequency range by nanocomposites containing flow-induced carbon nanofibers/nanotubes (PR-19 CNF & MWNT) and LLDPE matrix is reported in this chapter. The results presented in this chapter have been submitted to Polymer Engineering and Science as "Polarized-wave Electromagnetic Shielding of Anisotropic Carbon Nanoparticle-based LLDPE Composites" [16].

5.2 Experimental

5.2.1. Materials

The matrix polymer used for the nanocomposites was again poly(ethylene-co-1-octene), (Dowlex^{TM} 2045), a film grade linear low density polyethylene (LLDPE). It has a density of 0.920 g/cm^3, DSC melting point of 122ºC, and melt flow index of 1 g/10 min (190°C/2.16 kg, ASTM D1238). Carbon nanofibers, Pyrograf$^{®}$ III PR-19 (Applied

Science Inc.), and multi-walled carbon nanotubes (MWNT) from CheapTubes Inc., were used as nanomodifiers. To evaluate the behavior of completely oriented materials, continuous carbon fiber composites (control specimens) were also made. Thus, precut unidirectional PAN-based carbon fiber plies (prepregs) were used to lay-up a three-ply unidirectional (0°) composite by the resin infusion method (24 hours of curing with vacuum) using EPON 828 resin from Miller-Stephenson Chemical Company Inc. and post-curing at 120 °C for 2 hours. The concentration of the unidirectional composites was gravimetrically determined at about 70 vol% and had a thickness of about 0.5 mm.

Ultra-high temperature heat treatment (HT) at 2500°C was carried out for the as-received nanomodifiers prior to compounding [6]. The heat-treated (HT) PR-19 HT nanofibers have a diameter of 119±8 nm and a length of 10±2 µm, whereas MWNTs HT have a diameter of 42±3 nm and length of 6±1 µm for an aspect ratio (L/D) of about 85 and 145, respectively [7].

5.2.2 Processing

A Haake Rheomix 600 batch mixer (BM) was used to melt-mix LLDPE with the nanomodifiers at 190°C and 20 rpm for 2 min at a concentration of 10 vol% (~20 wt%). To impart flow-induced orientation in the nanomodifiers, the resulting composites were post-processed in a DSM Xplore 15 cc twin-screw micro-compounder (DSM), in co-rotating mode, at 230°C and 100 rpm for 10 min and micro-filament composites of about 100 µm in diameter were spun through a 300-µm-holes spinneret. The resulting micro-

filaments were arranged into oriented strips and sintered at 115°C. The sintered strips were, in turn, compacted at 190°C into sheets about 1.0 mm thick and 180 mm x 180 mm utilizing a Carver laboratory press. Thus, a parallel assembly of the oriented strips produced oriented composite sheets, whereas randomly arranged micro-filaments produced unoriented composite sheets. Two specimens were independently mixed and compacted per composite type (true replicates, n = 2).

5.2.3 Microstructural characterization

The dispersion level of the modifiers in the oriented nanocomposites was assessed by inspection of optical micrographs (OM, Olympus BX60) of 1 vol% diluted nanocomposite films of 5-12 μm in thickness. For this purpose, the 10 vol% oriented nanocomposites were softly diluted by twin-screw extrusion (20 rpm, 190°C and 2 min) with pure LLDPE. ImagePro® image analysis software was used to measure the average diameter and area of the clusters to characterize the nanomodifier dispersion level. Ten different optical micrographs of different portions of the diluted composite films, each of a length-scale encompassing about 2 mm, were analyzed per composite type.

The microstructure of the oriented nanocomposites was assessed by inspection of the cross-sections of the cryo-fracturated composites sheets (Hitachi S-4800, SEM). Both cross-sections were inspected: perpendicular to the filament direction (transversal view) and along the filament direction (longitudinal view). For each type of composite, five

different macroscopic locations were investigated in each direction. At least 4 micrographs were taken per location.

To assess the local orientation of nanomodifiers in the processed nanocomposites, image analysis (ImagePro®) of the SEM micrographs was carried out. The apparent aspect ratio of the nanomodifier cross-section (L_{max}/L_{min}) may be used to calculate a quantitative orientation parameter. A combination of $L_{max}/L_{min} = 1$ in the transverse view and $L_{max}/L_{min} = \infty$ in the longitudinal view signifies a perfect orientation. At least five high-magnification SEM micrographs were used for this task, which correspond to about 100-300 nanomodifiers analyzed for each cross-sectional view. Also, to evaluate the overall orientation of the nanomodifiers in the oriented composites, wide-angle X-ray diffraction (Rigaku-MSC, Houston, TX) was conducted on the composites. A Cu target Kα radiation with a wavelength of 1.5406 Å (n = 3) was used. The spectra were analyzed using Polar software version 2.6.7 from Stonybrook Technology and Applied Research (STAR). The X-ray source was operated at 45 kV and 0.65 mA, and the sample exposure time was 30 min.

5.2.4 Electrical conductivity

The DC in-plane volume electrical conductivity (S/m), of the composites was measured using a Keithley 6517B High Resistance Meter connected to a Keithley 8002A Resistivity Test Fixture modified with external copper electrodes (ASTM D257). The conductivity was obtained from resistance measurements of specimens that were 30 mm

wide, 1 mm thick and with lengths of ~ 20 mm. Silver paint was applied on the surfaces at each end of the samples and the in-plane resistance was measured. Measurements, using an alternating polarity DC voltage of ± 10V, along the longitudinal direction (LD) and the transverse direction (TD) were carried out for each composite type with a replication of 5 in each direction. Likewise, the DC through-plane electrical conductivity was measured with the same device, but using a Keithley 8009 Resistivity Test Fixture (alternating polarity DC voltage of ± 5V across the composites (n = 5)).

5.2.5 Electromagnetic shielding effectiveness (EM SE)

The electromagnetic shielding effectiveness (EM SE) was determined from the logarithmic ratio of the measured transmitted power with the material present, $P_{T,W}$, to the transmitted power without the material present, $P_{T,WO}$, which is represented with a reference specimen as described below (see also Appendix B) according to the ASTM D4935:

$$EM\ SE = -10 \log \frac{P_{T,W}}{P_{T,WO}} \tag{5.1}$$

Thus, the shielding effectiveness can be measured by subtracting the frequency dependent decibel magnitudes of the S_{21} scattering parameter of the reference specimen from that of the load specimen [6]. As explained in Appendix B, a load specimen is a sheet of the actual material that fully covers the waveguide flange, which is clamped between the gap separating the two halves of the transmission line. A reference specimen

is a sample of the same material and thickness of the load specimen cut out in the shape of the metallic flange at the gap interface (see **Figures B.3** and **C.1 (b)**). The purpose of this reference specimen is to correct for capacitive coupling effects between the disjoint metallic interfaces of the flange. Scattering parameters are typically determined using vector network analyzers. In this work, a Hewlett Packard 8753ES Network Analyzer was used to measure the magnitude of the S_{21} scattering parameter. Open-short-load calibration was performed using the Agilent 85033D calibration kit. The sample size of the load specimens for each test setup was 180 mm x 180 mm, with a thickness of ~1 mm. Two true replicates were tested (n = 2) per composite type. The references specimens were die-cut from the load specimens after the load measurements were carried out to keep the very same thickness and material for an accurate correction.

An Electro-Metrics EM-2107A which complies with the standard ASTM D4935 setup consisting of an air-core coaxial transmission line was first used to measure the EM SE of the specimens. This coaxial setup applies a radially polarized transverse electromagnetic (TEM) wave to the composite specimens from 30 MHz to 2 GHz and was measured to have a dynamic range of 80-100 dB. Additionally, in order to obtain a measure of anisotropic shielding effectiveness, rectangular waveguides were also used [17]. The frequencies used for these waveguides caused the TE_{10} mode of propagation to be applied to the composite specimens. In the TE_{10} mode of propagation, the electric field is transversely polarized in one direction [18]. In this chapter, the vertical direction of a waveguide is defined as perpendicular to the larger transverse dimension of the rectangular waveguide. This vertical direction is equivalent to the electric field

polarization in the TE_{10} mode. Two different waveguides from Space Machine & Engineering Corp. were used in order to test the specimens at different frequencies. For frequencies from 1.45-2.2 GHz a WR510 waveguide was used (129 mm width x 64 mm height). For frequencies from 2.2-3.3 GHz a WR340 waveguide was used (86 mm width x 43 mm height).

In addition, a FOCUS Microwave Inc. PTJ-2-APC7 slotted micro-strip transmission line (dynamic range: 30-40 dB) was used to test the anisotropic loss of the nanocomposite specimens from 100 MHz to 2.5 GHz. A micro-strip geometry imposes an electromagnetic field orientation where the electric field is principally polarized downward from the trace to the underlying ground plane. This mode of EM wave propagation is known as quasi transverse-electromagnetic (quasi TEM) [18]. Thus, like the rectangular waveguides, but unlike the coaxial transmission line due to its radial electric field polarization, this micro-strip structure is useful for testing the anisotropic attenuation characteristics of the oriented composite specimens. This micro-strip transmission line has a characteristic impedance of 50 Ω and consists of an approximately 3 mm wide metallic trace about 1 mm above a metallic block serving as a ground plane. There is an adjustable gap that divides the micro-strip into two halves for the insertion of the sample specimen. Due to the small height of the trace above the ground plane, measuring truly EM SE with this setup was impractical. However, the measurements of attenuation of the specimen relative to attenuation of an equal thickness air gap were obtained by subtracting their corresponding S_{21} scattering parameter decibel magnitudes. Henceforth in this chapter, the relative attenuation of the samples tested with

the micro-strip structure will refer to this ratio of power received with the material present to that received with an airgap of the same thickness. This measurement is similar to EM SE except that it does not correct for the capacitive coupling through the material between the disjoint metallic surfaces at the gap. Thus, although these measurements are not comparable to the EM SE measurements made with other setups, they are still useful for comparing between the differently oriented specimens for purposes of demonstrating effects of composite orientation on the electromagnetic properties. The reader can find in Appendix C documented details about the different wave propagation modes supported by the transmission lines used in this chapter.

5.2.6 Tensile test

Tensile test was carried out for the oriented nanocomposites using the ASTM D638 Type V technique at room temperature, which requires dogbone-shaped specimens of 25 mm of gauge-length and 3 mm of width. The specimens were about 1 mm in thickness and were die-cut into the ASTM dogbone shape. An ATS Universal 900 tensile tester at across-head speed of 25 mm/min was used. Five replicates in the longitudinal direction (LD, direction aligned with modifier orientation) and five in the transverse direction (TD, direction perpendicular to modifier orientation) were tested per nanocomposite type.

5.3 Results and Discussion

5.3.1. Composite morphology

Representative optical micrographs (OM) of the 1 vol% diluted composite films and their corresponding cluster size distributions are displayed in **Figure 5.1**. The PR-19 HT and MWNT HT diluted nanocomposites had similar cluster diameters of 14.4±5.4 μm and 14.9±4.8 μm, respectively. By optical microscopy, clusters smaller than 1 μm can be considered in the dispersed phase [19]. A measure of the non-disperse phase can be obtained with the ratio of the total cluster area, $A_{Clusters}$, to the total inspected area, A_{Total}, which, in thin films, is essentially a measurement of the volume fraction of the clusters (agglomerates) in the composite f_{Agg} [19]. Thus, PR-19 HT and MWNT HT diluted nanocomposites exhibited values of f_{Agg} of 0.0157±0.0065 and 0.076±0.0033, respectively.

Pegel et al. have defined the optical degree of dispersion, D_{OM} , as:

$$D_{OM} = 1 - {f_{Part} f_{Agg}}/{f_{Comp}} \tag{5.2}$$

where, f_{Comp} is the volume fraction of modifiers in the composites (i.e., 0.01 or 1 vol%) and f_{Part} is the volume fraction of modifiers in the clusters [19]. The bulk density of the nanomodifiers was measured at 0.1664 g/cm^3 for PR-19 HT, and at 0.1846 g/cm^3 for MWNT HT. The true density of the nanomodifiers was estimated at ~2.2 g/cm^3. Therefore, the optical degree of dispersion was determined at 0.892±0.044 and

0.942±0.025 for PR-19 HT nanocomposites and MWNT HT nanocomposites, respectively. These values are consistent with other dispersed composite systems reported by Kasaliwal et al. at about 0.80 for different MWNT types in polycarbonate matrix at 1 wt% [20].

Representative SEM micrographs of the oriented and unoriented nanocomposites, displayed in **Figure 5.2**, show no clusters, and the modifiers appear uniformly distributed. **Figures 5.2** (a) and (c) display the transverse cross-sectional areas of the oriented nanocomposites, i.e., also the cross-section of the original micro-filaments. The nanomodifiers are primarily normal to the viewed plane, which shows a preferred orientation in the direction of flow (also normal to the viewing plane). This was confirmed by the low values of the apparent aspect ratios of the modifiers (L_{max}/L_{min}), which were 1.6±0.1 and 1.9±0.2 for the PR-19 HT and MWNT HT nanocomposites, respectively. On the other hand, **Figures 5.2** (b) and (c) show the longitudinal view (i.e., along the micro-filament direction) of the cross-sections of the nanocomposites. The nanomodifiers also seem to be oriented in the direction of flow (i.e., along the micro-filament direction) and their corresponding apparent aspect ratios were 7.3±1.1 and 6.5±1.2 for the PR-19 HT and MWNT HT oriented nanocomposites, respectively. These apparent aspect ratios values are respectively about 4 and 3 times greater than those obtained for the transversal view, which confirms a preferred local orientation of the nanomodifiers in the direction of flow. **Figures 5.2** (e) and (f) display the micrographs corresponding to the cross-sections of the unoriented PR-19 HT and MWNT HT

nanocomposites, respectively. By SEM, no preferred orientation was observed for any of the unoriented nanocomposites.

Figure 5.3 contains a representative X-ray diffractogram for the unidirectional continuous CF-epoxy composites (highly oriented control sample) and its corresponding 2θ and azimuthal scans. The peak associated with the (002) graphene layer planes in the graphitic structure of the fibers is at about 25° and a high intensity region in the form of an arc suggests a high level of orientation in the composites. The corresponding in-plane Herman's orientation factor, $f_p = 2\langle \sin^2 \phi \rangle - 1$, for the azimuthal angle distribution of the (002) peak was about 0.67, indicating a high level of orientation. At 2θ values less than 20° the amorphous halo of epoxy can also be appreciated. The (100) and (101) graphene planes are overlapped in a peak at about 43° [21].

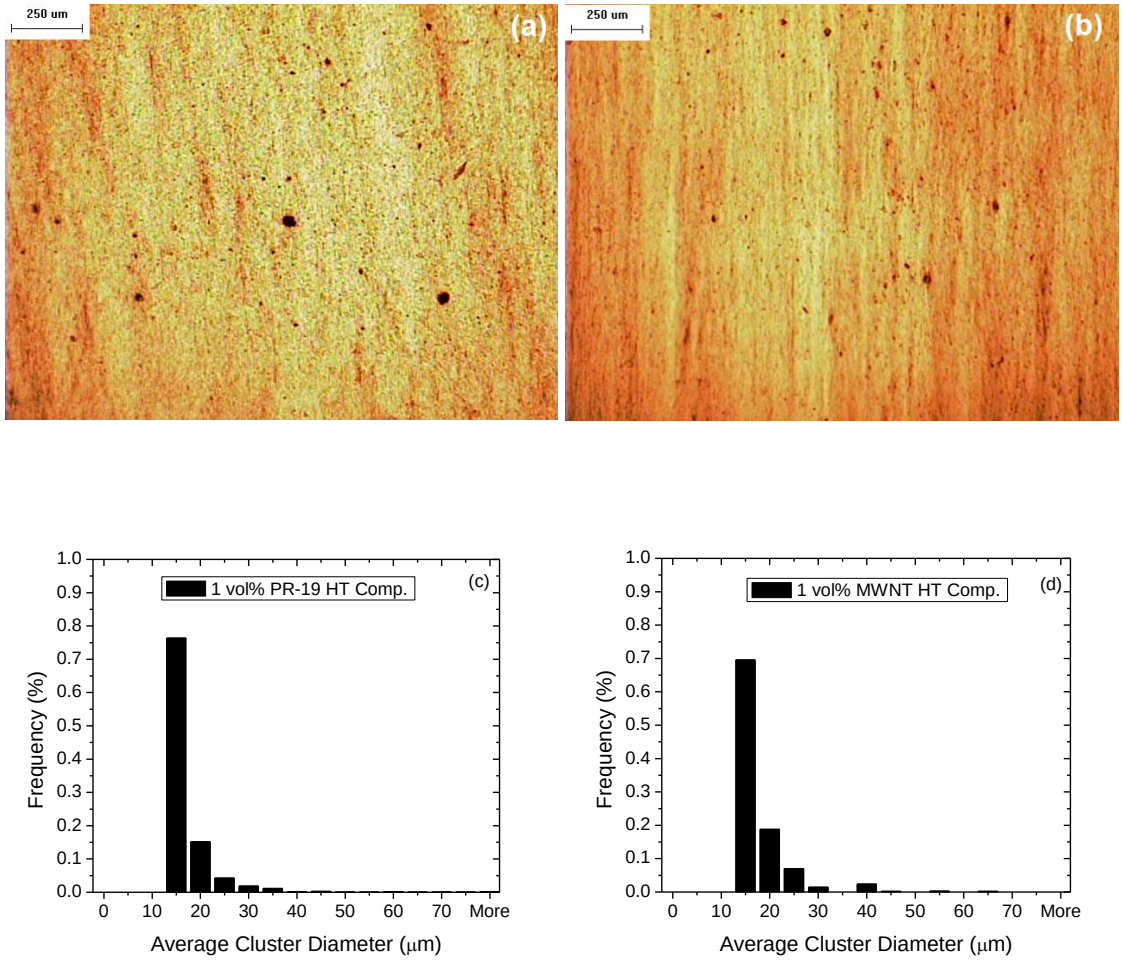

Figure 5.1. Representivative transmission optical micrographs and their corresponding cluster diameter distributions of ~10-μm thick films made of diluted nanocomposites at 1 vol%. (a, c) PR-19 HT diluted nanocomposites, (b, d) MWNT HT diluted nanocomposites.

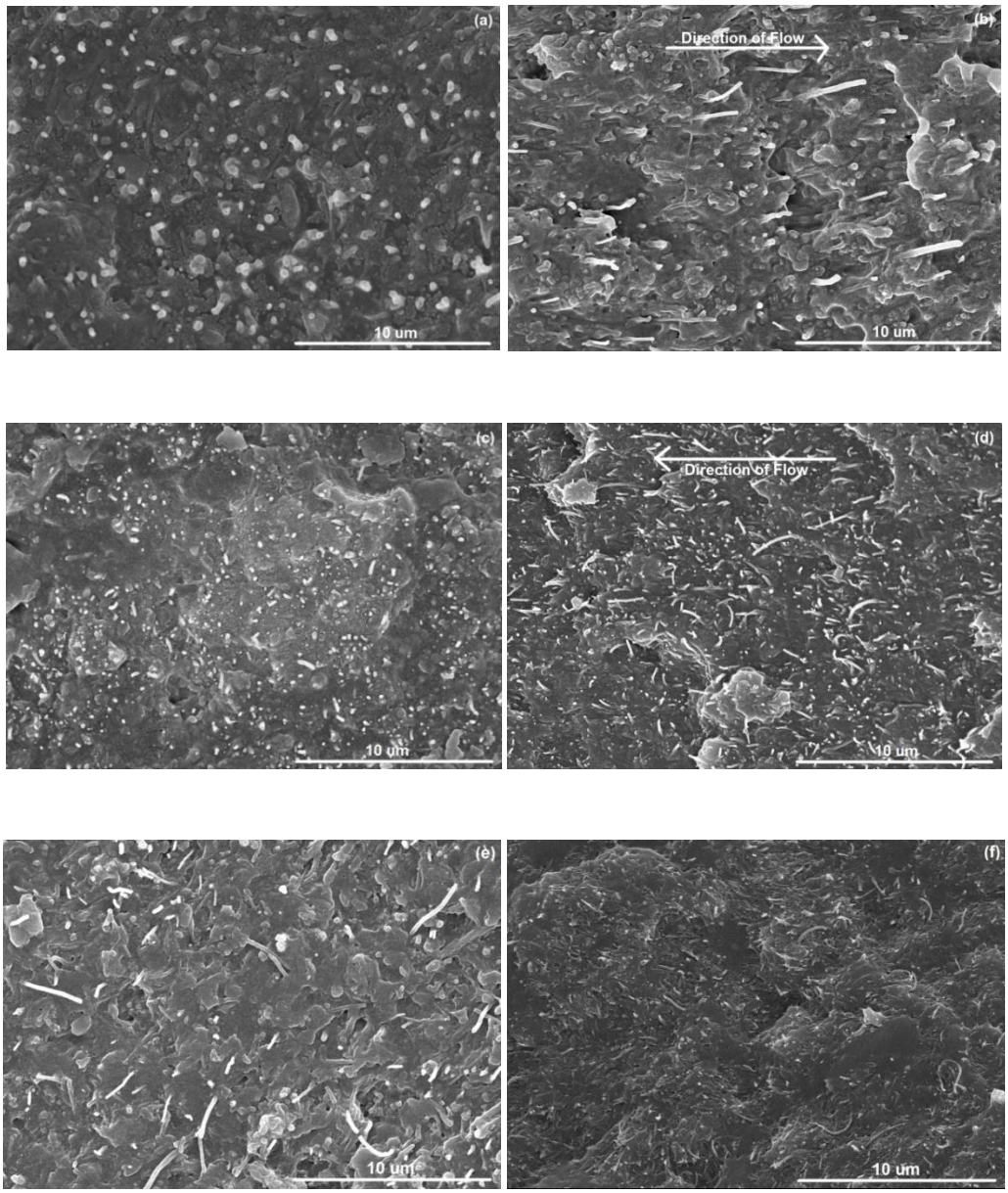

Figure 5.2. Representative scanning electron micrographs (SEM) of the cross-sections of the nanocomposites at 10 vol% (a) PR-19 HT oriented comp. transverse view, (b) PR-19 HT oriented comp. longitudinal view; (c) MWNT HT oriented comp. transverse view, (d) MWNT HT oriented comp. longitudinal view, (e) PR-19 HT unoriented comp., (f) MWNT HT unoriented comp.

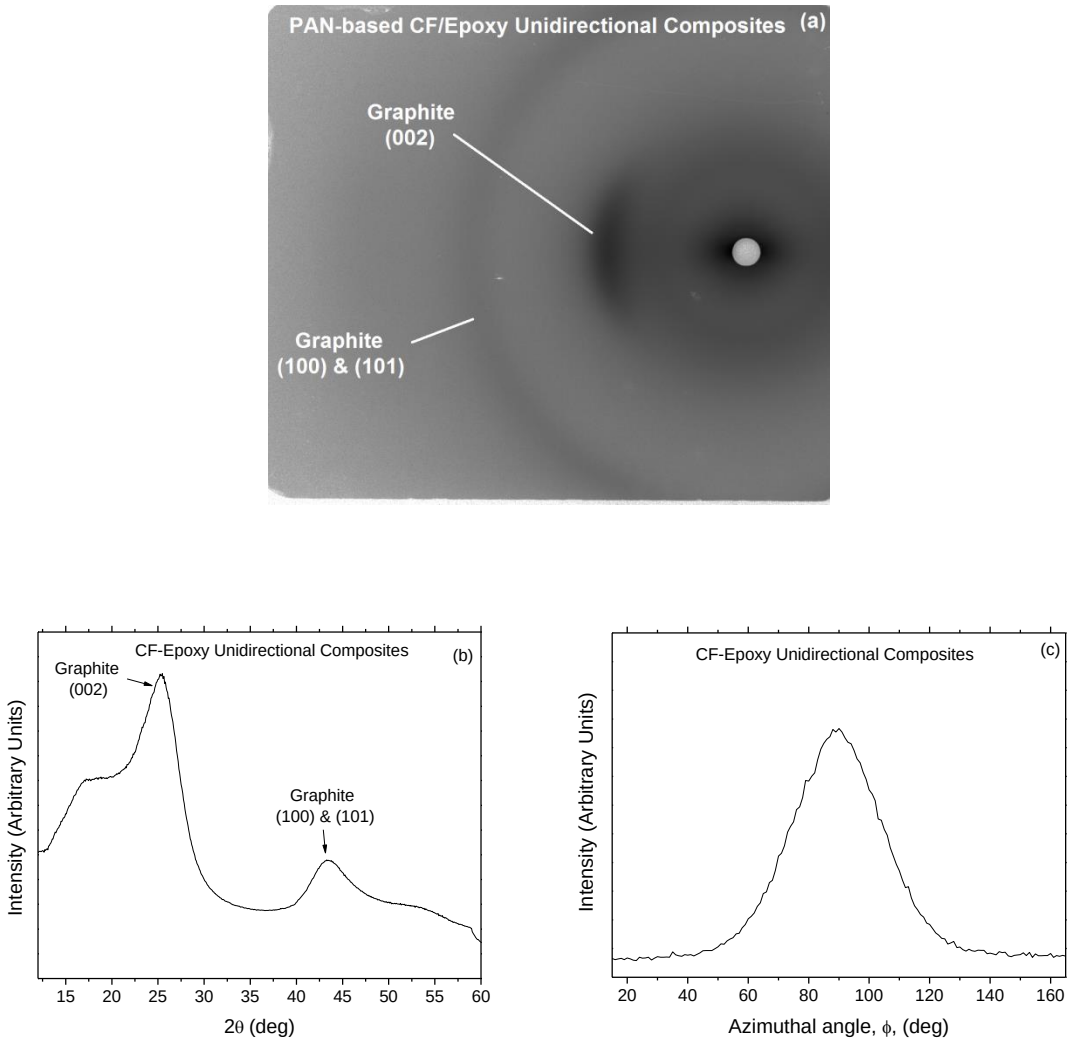

Figure 5.3. Representative wide-angle X-ray diffractogram of (a) unidirectional continuous CF-Epoxy composites at ~70 vol%, and its corresponding (b) 2θ and (c) azimuthal, ϕ, scans.

Figures 5.4 (a)-(f) display representative diffractograms of the oriented and unoriented nanocomposites, and the corresponding 2θ and azimuthal scans. In the nanocomposites, the graphitic peak associated with (002) layer planes of carbon nanomodifiers appears at approximately 26°, whereas the (110) and (200) peaks corresponding to the orthorhombic crystallites of the LLDPE matrix appear at about 21.4° and 23.7°, respectively. It is also evident from the azimuthal distribution of the graphitic (002) peak that there is a predominant fraction of nanomodifiers with a preferred angle of orientation in the oriented PR-19 HT and MWNT HT nanocomposites, with values of 0.49 and 0.39 measured for Herman's orientation factors, respectively. This is consistent with the apparent aspect ratio (L_{max}/L_{min}) measurements. In contrast, a predominantly random orientation of the modifiers was observed in the plane of the unoriented nanocomposites as their azimuthal scans showed no angular dependency (basically flat curve) with both Herman's orientation factors of only about 0.16. These differences in orientation can also be qualitatively appreciated in the diffractograms, which show a higher intensity portion (darker arc) of the (002) graphitic diffraction lines around 90° for the oriented composites. In contrast, for the unoriented nanocomposites, the intensity of their (002) graphitic diffraction lines had a uniform intensity for all azimuthal angles.

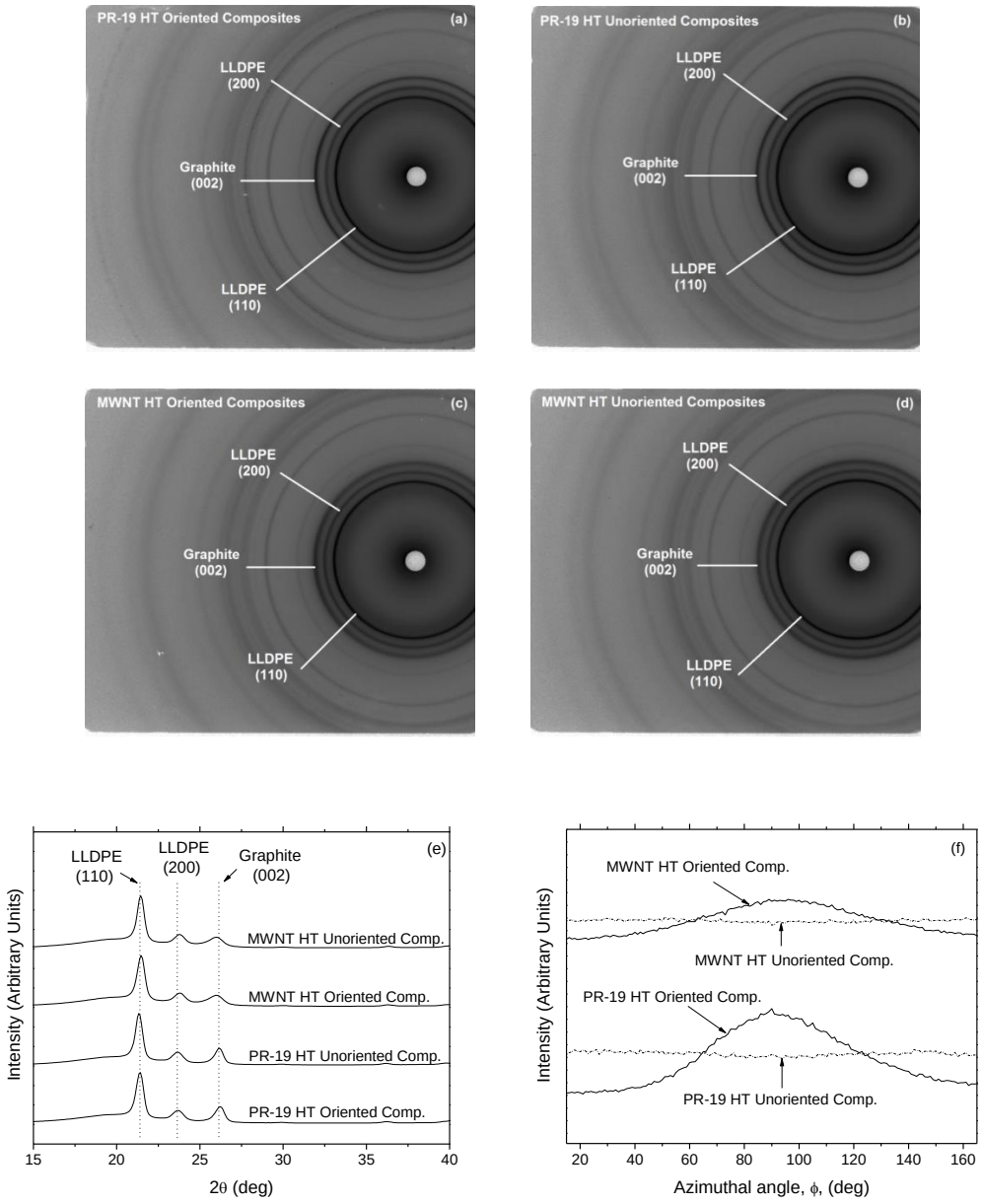

Figure 5.4. Representative wide-angle X-ray diffractograms of nanocomposites at 10 vol% (a) PR-19 HT Oriented comp., (b) PR-19 HT Unoriented comp. and (c) MWNT HT Oriented comp., (b) MWNT HT Unoriented comp. X-ray diffractograms of the composites as function of (c) the 2θ and (d) azimuthal, ϕ, angles. Curves were shifted vertically along intensity axis to avoid overlap.

5.3.2 Composite electrical conductivity

Table 5.1 summarizes the DC in-plane and through-plane conductivities of the different composites at 10 vol% (replicates, n = 5 in all cases). For the oriented composites, the in-plane conductivity in the micro-filament direction (LD) was at least an order of magnitude higher than that in the transverse direction (TD), which means that the composites displayed anisotropic conductivity. In addition, the through-plane values were smaller by several orders of magnitude when compared to their respective in-plane values. This was particularly noticeable in the continuous CF-epoxy unidirectional composites, our highly oriented control, which showed the highest electrical anisotropy. Thus, the direction of greater conductivity was LD for all oriented composite types. Overall, the CF-epoxy composites displayed in-plane conductivity values higher than those of MWNT HT oriented nanocomposites, and these, higher than those of the PR-19 HT oriented nanocomposites. This conductivity trend is consistent with the infinite true aspect ratio (L/D) of CF, followed by that of the MWNT HT at 145 and by that of the PR-19 HT at 85, which establishes a direct relationship between the modifier aspect ratio and the conductivity of the composite.

Table 5.1. DC in-plane and through-plane volume conductivity of composites at 25°C and ~ 50 % relative humidity. Ranges represent 95% confidence intervals.

Composite	DC in-plane volume conductivity (S/m)		DC through-plane volume conductivity (S/m)
	Longitudinal direction (LD)	Transverse direction (TD)	
CF-Epoxy Unidirectional‡	$4.0\pm1.8\times10^{2}$	$1.1\pm0.4\times10^{1}$	$7.5\pm1.5\times10^{-6}$
PR-19 HT-LLDPE Oriented*	$1.7\pm0.7\times10^{-2}$	$1.1\pm0.4\times10^{-3}$	$6.0\pm1.5\times10^{-6}$
MWNT HT-LLDPE Oriented*	$3.1\pm1.4\times10^{0}$	$1.7\pm0.2\times10^{-1}$	$2.3\pm0.8\times10^{-4}$
PR-19 HT-LLDPE Unoriented*	$6.2\pm1.7\times10^{-2}$		$1.4\pm0.7\times10^{-4}$
MWNT HT-LLDPE Unoriented*	$5.0\pm1.0\times10^{0}$		$6.3\pm1.6\times10^{-4}$

‡70 vol%, *10 vol%

The unoriented nanocomposites, though, displayed in-plane conductivity values about 2-3 times higher than their respective counterparts in the LD. This is expected due to a more random distribution of the modifiers, which leads to higher likelihood of electrical percolation in the electrical networks within the composites [22]. The through-plane conductivity of the unoriented composites was also 4 to 6 orders of magnitude smaller than their respective in-plane values. This difference in conductivity is due to the 2D in-plane random orientation of the modifiers in the composite specimen. In the plane, the carbon nanomodifiers use their radial electrical conductivity to conduct electrons through the thickness of the specimen, which, as in many carbon materials, is much less that their axial conductivity [8, 23]. All composites types were electrically percolated systems when compared with a conductivity of $7.0\pm1.1\text{x}10^{-15}$ S/m for pure LLDPE, which is, at least, 9 orders of magnitude lower than that of the composites.

5.3.3 Electromagnetic shielding effectiveness (EM SE)

Figure 5.5 displays the EM SE of the oriented composites obtained by the coaxial line. The EM SE was measured with the LD of the composite at 0°, 45° and 90° angles from an arbitrary angular reference position on the flange of the gapped coaxial line. The EM SE was found to be independent on the angle of orientation as all three responses overlapped each other for each oriented composite type. This is consistent with the fact that, in a coaxial line, the main electromagnetic field propagation mode has its electric field radially polarized. Thus, the composite specimen will provide a level of attenuation

independent of the specimen's angular position due to the axial symmetry of the electric field imposed by the coaxial geometry. Moreover, it is important to note that the EM SE of the composites increases with the conductivity of the composites as the CF-Epoxy composites displayed about 20 dB (for 1 mm of thickness), the MWNT HT oriented nanocomposites about 7 dB, and the PR-19 HT oriented composites about 1 dB, all values at 2 GHz.

Figure 5.6 displays the EM SE of the unoriented nanocomposites obtained by the coaxial line. Three different relative angular positions were also evaluated at 0°, 45° and 90° angles. As expected, no orientation dependency was found as the EM SE was independent of the angular position. Furthermore, since the in-plane conductivity of the unoriented nanocomposites was higher than that of the maximum in-plane conductivity of the oriented ones, the unoriented nanocomposites also displayed higher values of EM SE at about 5 dB and 9 dB, respectively for PR-19 HT and MWNT HT unoriented nanocomposites at 2 GHz.

Figure 5.7 contains the EM SE results for the unidirectional CF-epoxy composites obtained by the rectangular waveguides as function of the angle between the direction of electric field polarization in the dominant wave propagation mode (TE_{10}) and the direction of maximum conductivity of the composites (i.e., fiber or longitudinal direction, LD). As the direction of maximum conductivity went from 90° (i.e., LD perpendicular to the E-field polarization) to 45°, and from 45° to 0° (i.e., LD parallel with the E-field polarization), the EM SE respectively varied from 11±2 dB to 20±3 dB, and

from 20±3 dB to 59±4 dB for the WR510 waveguide. Likewise, for the WR340 waveguide, the EM SE increased from 11±1 dB to 19±2 dB, and from 19±2 dB to 70±4 dB, respectively. This means an increase in EM SE of about 50 dB after changing the composite LD orientation from perpendicular to parallel, relative to the direction of polarization. Thus, in vertically polarized waves the anisotropic conductivity of the composites will also infer differences in electromagnetic shielding, depending of the relative angle of alignment between the direction of polarization and that of the maximum conductivity of the composite. This electromagnetic anisotropy will lead the oriented composites to mostly shield the polarizations of the wave parallel to the direction of maximum conductivity and let the orthogonal polarizations pass through. This behavior is similar to what occurs in typical AM/FM and VHF/UHF receptor antennas in which the orientation of the antenna relative to that of the wave polarization plays an important role for proper signal reception.

Figure 5.8 displays the EM SE of the oriented nanocomposites obtained by measurements with both rectangular waveguides as described in the experimental section. This figure shows two extreme cases: i) maximum conductivity direction (LD) perpendicular to the E-field polarization (90°); and ii) maximum conductivity direction (LD) parallel with the E-field polarization (0°). When the LD was aligned with the E-field polarization, the PR-19 HT oriented nanocomposites displayed EM SE values of 3.2±1.0 dB when tested with the WR510 waveguide and 5.1±1.1 dB when tested with the WR340 waveguide. For the perpendicular alignment (90°), the EM SE of the PR-19 HT oriented composited were measured to be only 0.7±0.4 dB when tested with the WR510

waveguide and 1.3±0.8 dB when tested with the WR340 waveguide. When the LD was parallel with the E-field polarization, the MWNT HT oriented nanocomposites displayed EM SE values of 9.0±1.0 dB for the WR510 tests and 11.1±1.1 dB for the WR340 tests. For the perpendicular alignment (90°) the EM SE of the MWNT HT oriented nanocomposites displayed EM SE values of only 3.0±0.8 dB for the WR510 tests and 3.8±1.0 dB for the WR340 tests. Thus, differences in EM SE of 6 dB for the PR-19 HT oriented nanocomposites and 7.3 dB for the MWNT HT oriented nanocomposites were observed when the composite longitudinal direction (LD) was changed from perpendicular to parallel, relative to the polarization.

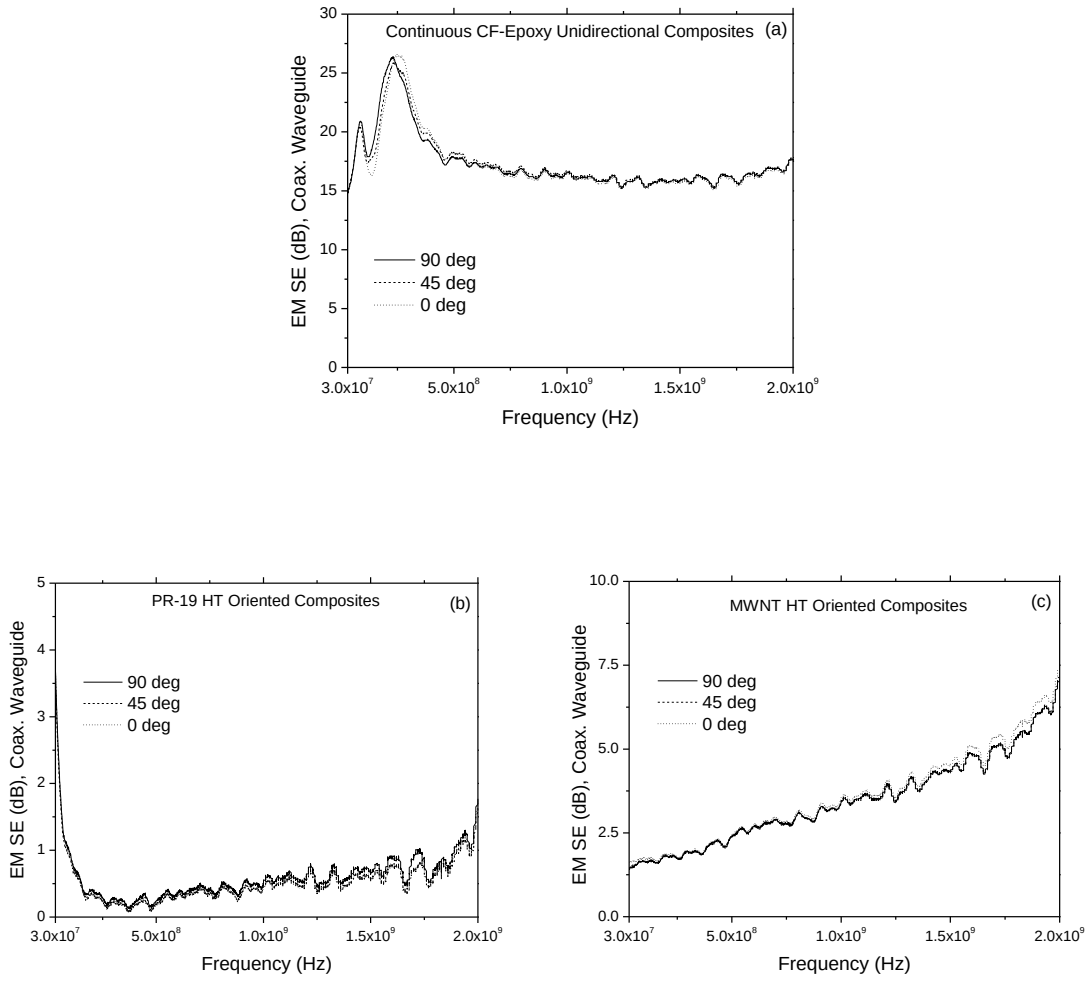

Figure 5.5. Electromagnetic shielding effectiveness (EM SE) of representative oriented composites obtained with the coaxial line as a function of the relative angular position (a) 70 vol% PAN-based CF-epoxy unidirectional composites, (b) 10 vol% PR-19 HT oriented comp., (c) 10 vol% MWNT HT oriented comp. Frequency range from 30 MHz to 2 GHz.

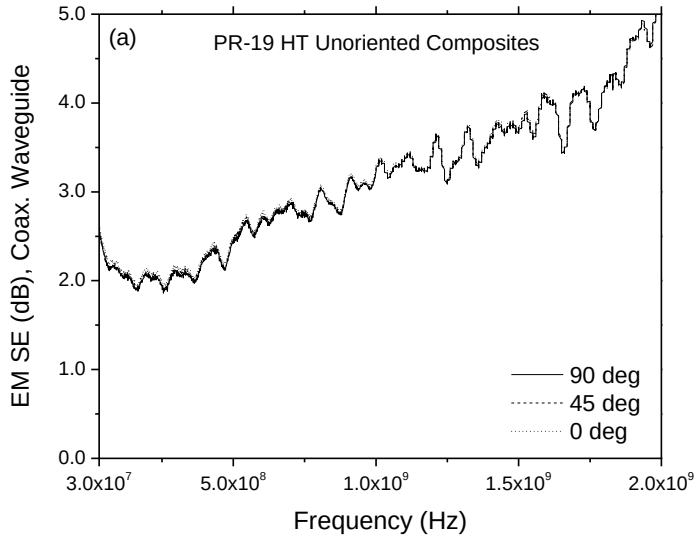

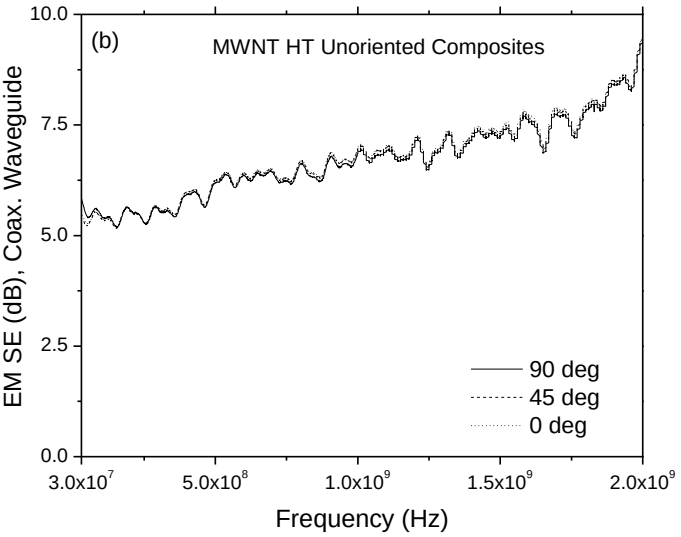

Figure 5.6. Electromagnetic shielding effectiveness (EM SE) of representative unoriented nanocomposites obtained with the coaxial line as a function of the relative angular position (a) 10 vol% PR-19 HT comp., (b) 10 vol% MWNT HT comp. Frequency range from 30 MHz to 2 GHz.

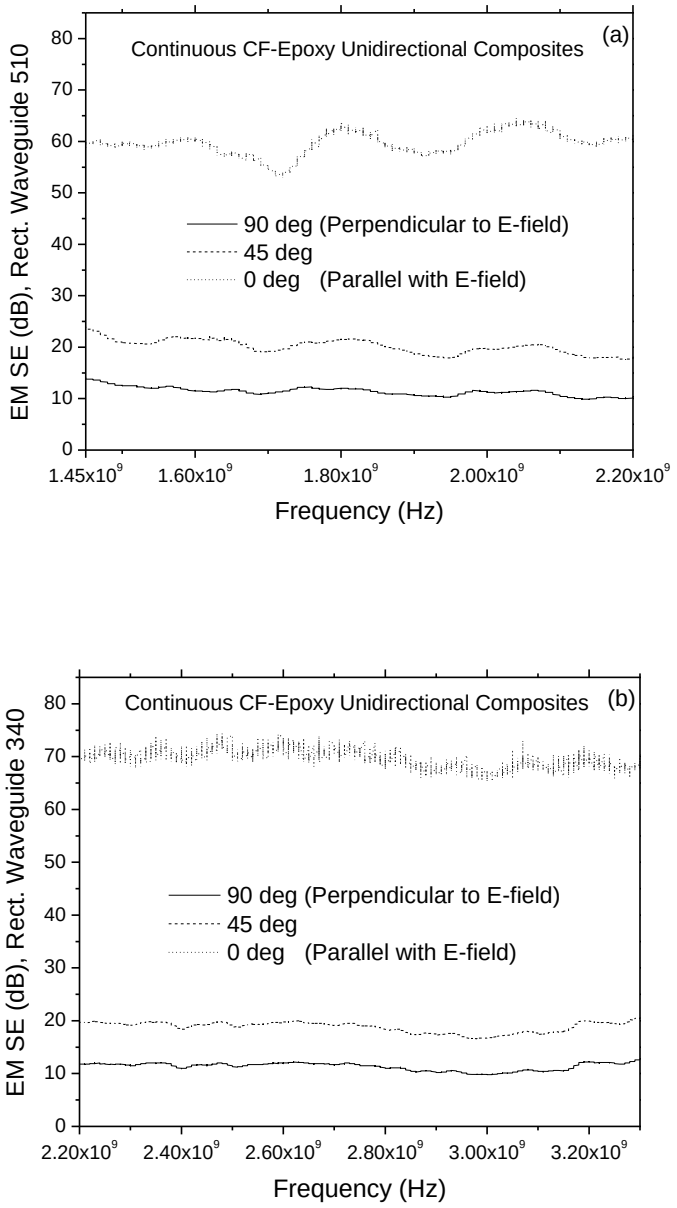

Figure 5.7. Electromagnetic shielding effectiveness (EM SE) of representative 70 vol% CF-epoxy unidirectional composites as a function of the angle of alignment between the main wave polarization of the rectangular waveguide (TE_{10}) and the direction of the highest conductivity of the composite: (a) WR510 and (b) WR340.

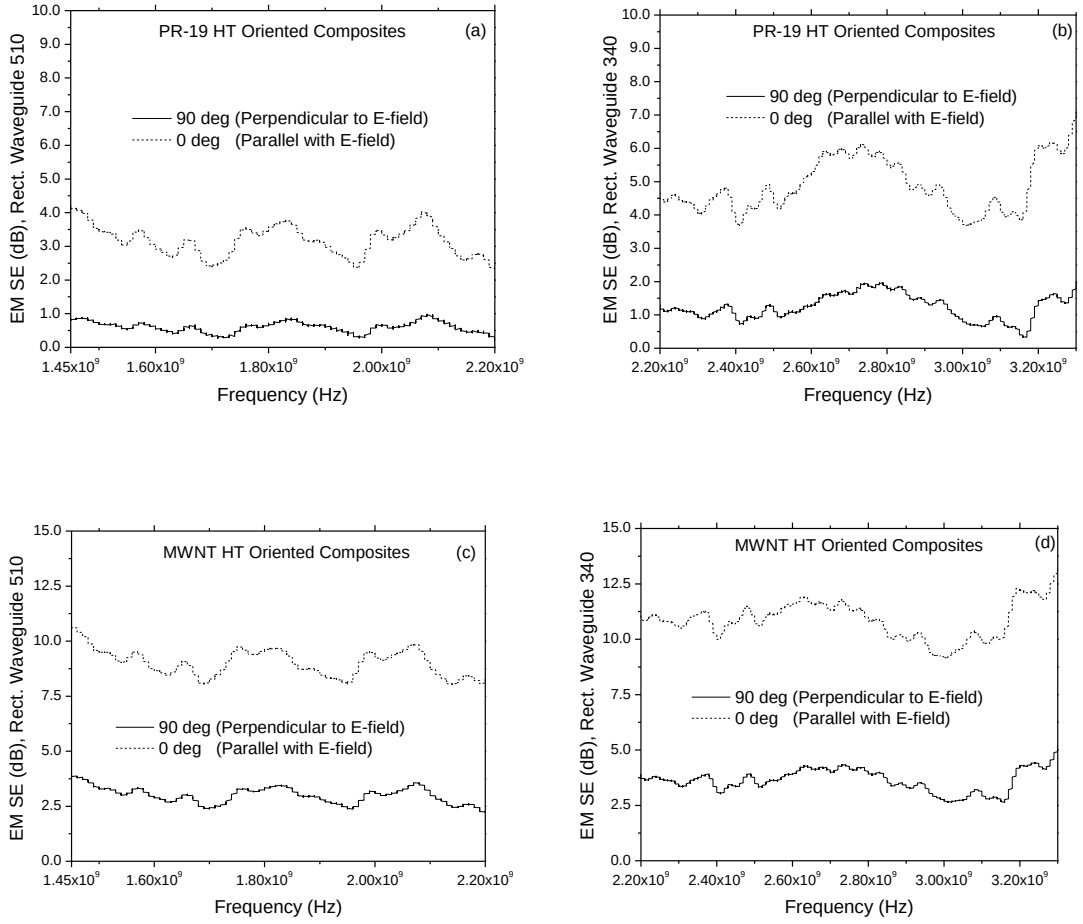

Figure 5.8. Electromagnetic shielding effectiveness (EM SE) of representative oriented nanocomposites as a function of the angle of alignment between the main wave polarization of the rectangular waveguide (TE_{10}) and the direction of the highest conductivity of the composites: (a) PR-19 HT comp. by WR510; (b) PR-19 HT comp. by WR340; (c) MWNT HT comp. by WR510; (d) MWNT HT comp. by WR340.

Figure 5.9 shows the EM SE of the unoriented nanocomposites measured with the WR340 waveguide. The EM SE values for the PR-19 HT unoriented nanocomposites were 7.6±1.1 dB when the LD was perpendicular to the E-field polarization, and 7.4±1.0 dB when the LD was parallel with the E-field polarization. For the MWNT HT nanocomposites, values of 12.6±1.2 dB and 12.8±1.3 dB were measured for the perpendicular alignment and parallel alignment of the LD with the E-field polarization, respectively. Thus, in contrast to the oriented composites, these nanocomposites showed no orientation dependency.

Figure 5.10 displays the measurements of the relative attenuation of the oriented nanocomposites in the micro-strip test setup (relative to measurements with just the air gap as described in the experimental section), over the frequency range from 100 MHz to 2.5 GHz. With the maximum conductivity direction (LD) placed perpendicular to the E-field (90°), values of relative attenuation of about 1.5±0.6 dB and 5.3±1.3 dB were measured for the PR-19 HT and MWNT HT oriented nanocomposites respectively. For the parallel alignment of the LD and the E-field polarization (0°), the respective relative attenuation values were 4.6±0.8 dB and 11.0±1.1 dB.

Figure 5.11 presents the relative attenuation of the unoriented nanocomposites obtained using the micro-strip for the same frequency range. Regardless the level of alignment between the LD and the direction of polarization, the values for the PR-19 HT and MWNT HT unoriented nanocomposites were about 10.5±0.7 dB and 15.0±1.0 dB, respectively. Once again, no orientation dependence was observed. Note that these

nanocomposites exhibited relative attenuation values higher than those of their oriented counterparts by at least 5 dB. The CF-epoxy composites were not analyzed by the micro-strip due to the low dynamic range of this test set-up (30-40 dB).

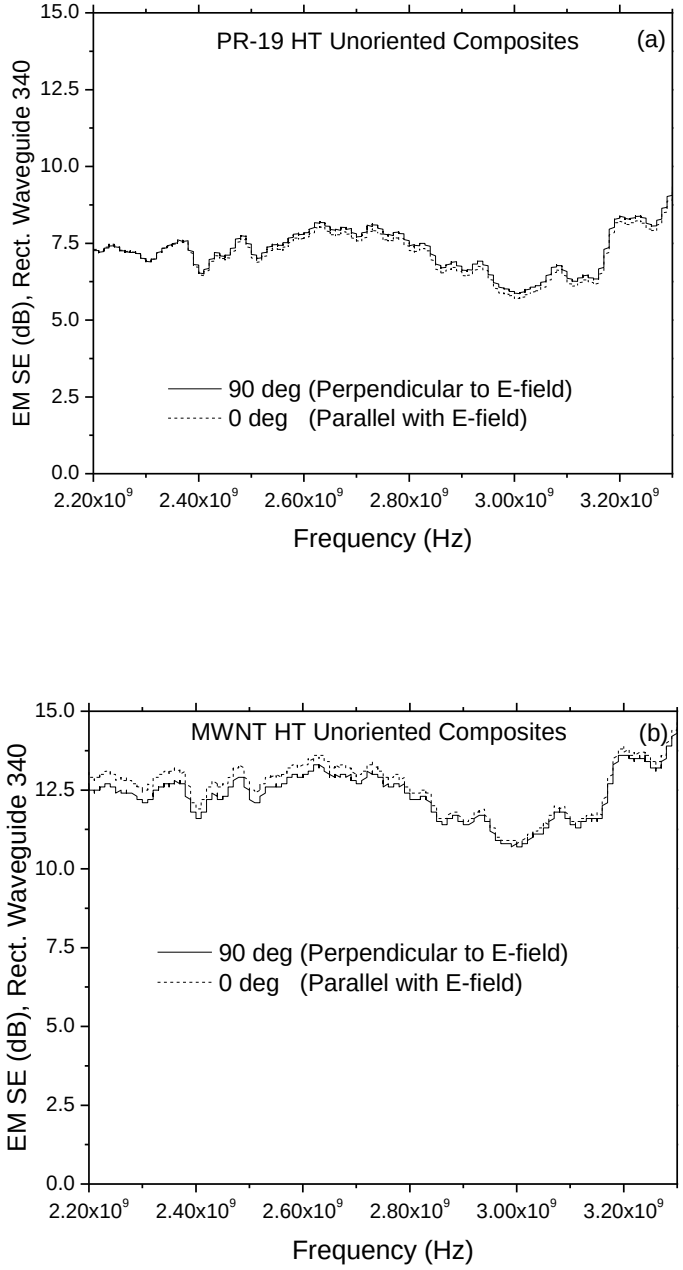

Figure 5.9. Electromagnetic shielding effectiveness (EM SE) of representative 10 vol% unoriented nanocomposites obtained by the WR340 (a) PR-19 HT composites and (b) MWNT HT composites.

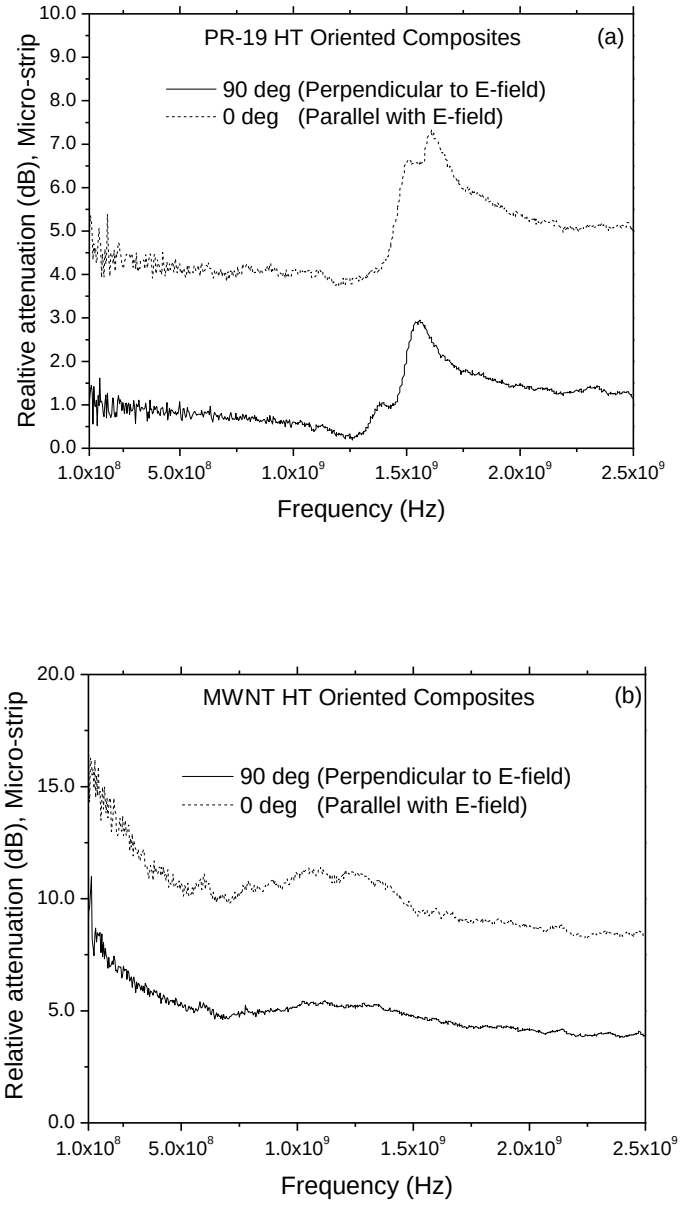

Figure 5.10. Relative attenuation of representative 10 vol% oriented nanocomposites as a function of the angle of alignment between the wave polarization of the micro-strip and the direction of the highest conductivity of the composite: (a) PR-19 HT oriented comp. and (b) MWNT HT oriented comp. Frequency range from 100 MHz to 2.5 GHz.

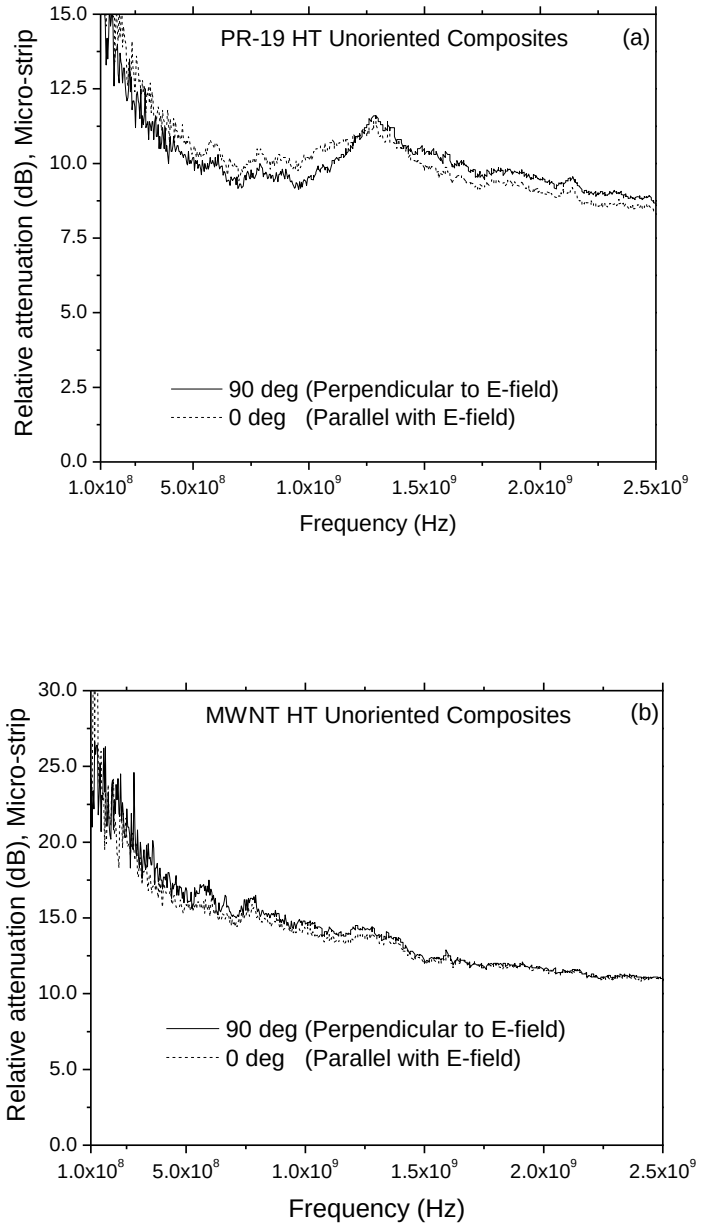

Figure 5.11. Relative attenuation of representative 10 vol% unoriented nanocomposites obtained by the micro-strip (a) PR-19 HT composites and (b) MWNT HT composites. Frequency range from 100 MHz to 2.5 GHz.

Figure 5.12 shows the correlation between the EM SE values measured in the rectangular waveguides (WR510 and WR340), and the in-plane conductivity of the composites. A strong dependency of the EM SE with respect to the conductivity aligned with the E-field was found. This dependency was especially remarkable when the parallely aligned modifiers with the E-field yielded composite conductivities greater than 1 S/m, after which a sudden increment in EM SE was observed.

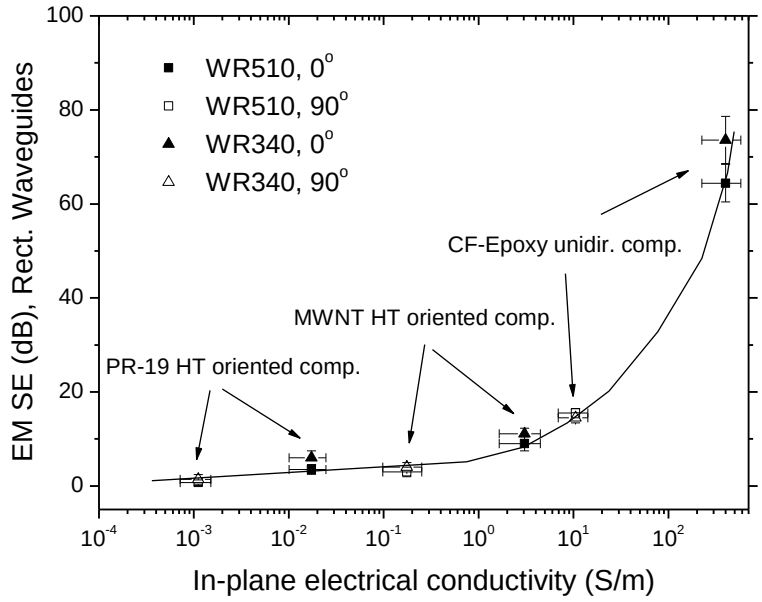

Figure 5.12. Correlation between the EM SE of the oriented composites and the in-plane electrical conductivity aligned with the E-field. EM SE from WR510 & WR340. Thickness of 1 mm was used for all samples. 0°: E-field aligned with the direction of maximum conductivity; 90°: E-field aligned with the direction of minimum conductivity of the composite.

5.3.4 Composite tensile properties

Figure 5.13 contains the tensile data obtained for the oriented nanocomposite in the longitudinal (LD) and transverse (TD) directions. The pure LLDPE data is also shown as the range between the discontinuous lines for comparison purposes. In the longitudinal direction, both nanocomposites displayed an apparent modulus and ductility that are about twice and half of those of the pure LLDPE, respectively. The tensile strength for the PR-19 HT nanocomposites in LD was about 19 MPa, while that of the MWNT HT nanocomposites was slightly higher at 24 MPa, which is very close to the strength of the pure matrix. In contrast, in the transverse direction, both nanocomposites displayed a flexibility that is not significantly different from that of the pure matrix, a strength about half of the LLDPE, and a very poor ductility (<30%). It is evident from these data that the orientation of the nanomodifiers also led to anisotropic tensile properties. Thus, the properties measured in the direction of the orientation of the modifiers (LD) tend to yield stiffer, stronger and more ductile nanocomposites. This intrinsic anisotropy in the mechanical properties needs to be taken into account when determining what type of EMC application the composites can be utilized on. However, the mechanical performance of these nanocomposites is excellent when compared with traditional carbon fiber LLDPE composites [6].

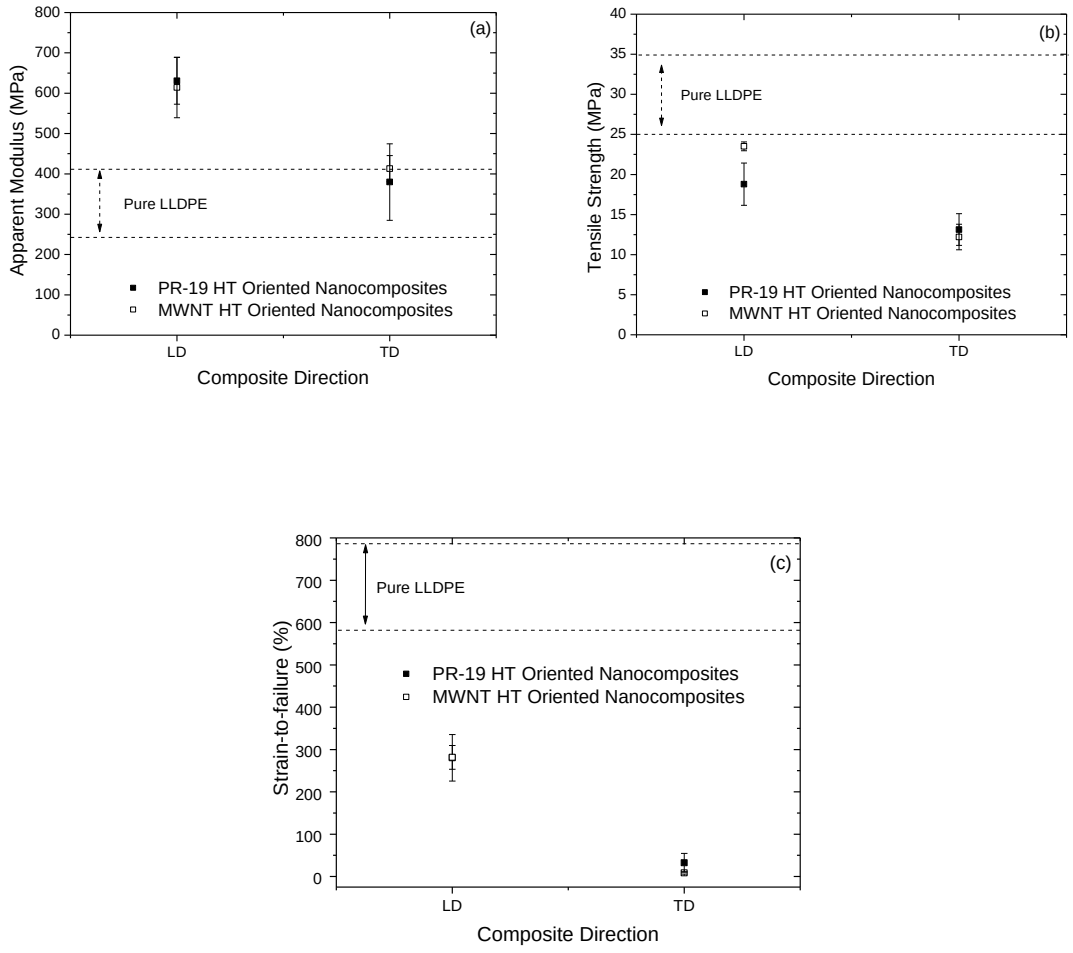

Figure 5.13. Tensile data for the oriented nanocomposites in the longitudinal (LD) and transverse (TD) directions. (a) apparent modulus, (b) tensile strength and (c) strain-to-failure.

5.4 Conclusions

WAXD analysis of the nanocomposites and microstructure observed by SEM and OM indicate a preferred orientation of the dispersed carbon nanomodifiers imparted by the combination of shearing and elongational flow-fields during filament spinning. These LLDPE-based nanocomposites containing 10 vol% of oriented carbon nanotubes/nanofibers exhibited anisotropic in-plane electrical conductivity. The highest conductivity was found to be in the direction of the micro-filaments (LD). The nanocomposites also displayed anisotropic shielding behavior when polarized electromagnetic waves were applied. The EM SE was a function of the angle of alignment between the direction of the maximum in-plane conductivity and that of the E-polarization. Thus, the 1-mm thick MWNT HT oriented nanocomposites displayed EM SE values (measured using the WR340) of only ~4 dB for perpendicular alignment, but ~11 dB for parallel alignment of modifiers and electric field. A positive correlation between the EM SE and the conductivity parallel to the E-field was observed for different composites. The oriented nanocomposites shield electromagnetic waves with electric-field components parallel to the direction of modifier orientation more strongly than orthogonal polarizations. Furthermore, the tensile properties of such nanocomposites displayed anisotropy, with stiffer, stronger and more ductile behavior in the direction of modifier orientation; and retained a great deal the properties of the pure LLDPE. Such nanomaterials may be used for compatibility applications where electromagnetic-wave polarization filtering is required in the VHF/UHF frequency range.

5.5 References

1. Paul CR. Introduction to Electromagnetic Compatibility. United States of America: John Wiley & Sons, Inc., 1992.

2. Ramo S, Whinnery JR, Van Duzer T. Fields and Waves in Communication Electronics. United States of America: John Wiley & Sons, Inc., 1984.

3. Al-Saleh MH, Sundararaj U. Electrically conductive carbon nanofiber/polyethylene composite: effect of melt mixing conditions. Polym Adv Technol 2011;22:246-253.

4. Al-Saleh MH, Sundararaj U. Electromagnetic interference shielding mechanisms of CNT/polymer composites. Carbon 2009;47:1738-1746.

5. Yamamoto N, Guzman de Villoria R, Wardle BL. Electrical and thermal property enhancement of fiber-reinforced polymer laminate composites through controlled implementation of multi-walled carbon nanotubes. Compos Sci Technol 2012;72:2009-2015.

6. Villacorta BS, Ogale AA, Hubing TH. Effect of Heat Treatment of Carbon Nanofibers on the Electromagnetic Shielding Effectiveness of Linear Low Density Polyethylene Nanocomposites. Polym Eng Sci 2013;53:417-423.

7. Villacorta BS, Ogale AA. Carbon Nanoparticle-based Flexible LLDPE Composites for Enhanced Electromagnetic Shielding Effectiveness. In: Haghi AK, Thomas S, Shanks R, Joy J, editors. Recent trends in micro and nanostructured polymer systems. Canada: Apple Academic Press, 2013.

8. Villacorta BS, Ogale AA, Hubing TH. Influence of Composite Electrical Properties on the VHF-UHF Electromagnetic Shielding Characteristics of Polyethylene-Carbon Nanoparticle Composites. Compos Sci Technol;submitted paper on 06-18-13.

9. Arjmand M, Mahmoodi M, Gelves GA, Park S, Sundararaj U. Electrical and electromagnetic interference shielding properties of flow-induced oriented carbon nanotubes in polycarbonate. Carbon 2011;49:3430-3440.

10. Abbasi S, Carreau PJ, Derdouri A. Flow induced orientation of multiwalled carbon nanotubes in polycarbonate nanocomposites: Rheology, conductivity and mechanical properties. Polymer 2010;51:922-935.

11. Kuringer R.J., Alam MK, Anderson DP, Jacobsen RL. Processing and Characterization of aligned vapor grown carbon fiber reinforced polypropylene. Composites Part A 2002;33:53-62.

12. Malwitz MM, Lin-Gibson S, Hobbie EK, Butler PD, Schmidt G. Orientation of Platelets in Multilayered Nanocomposite Polymer Films. J Polym Sci Part B 2003;41:3237-3248.

13. Jou WS, Wu TL, Chiu SK, Cheng WH. The Influence of Fiber Orientation on Electromagnetic Shielding in Liquid-Crystal Polymers. J Electronic Mat 2002;31(3):178-184.

14. Larin B, Lyashenko T, Harel H, Marom G. Flow induced orientated morphology and properties of nanocomposites of polypropylene/vapor grown carbon fibers. Compos Sci Technol 2011;71:177-182.

15. Arjmand M, Apperley T, Okoniewski M. Comparative study of electromagnetic interference shielding properties of injection molded versus compression molded multi-walled carbon nanotube/polystyrene composites. Carbon 2012;50:5126-5134.

16. Villacorta BS, McDowell A, Hubing TH, Ogale AA. Polarized-wave Electromagnetic Shielding of Anisotropic Carbon Nanoparticle-based LLDPE Composites. Polym Eng Sci, 2013, Submitted on 10-10-2013.

17. Mohanraj GT, Chaki TK, Chakraborty A, Khastgir D. AC impedance analysis and EMI shielding effectiveness of conductive SBR composites. Polym Eng Sci 2006;46: 1342-1349.

18. Pozar DM. Microwave engineering. United States of America: Addison-Wesley Publishing Company, Inc., 1990.

19. Pegel S, Villmow T, Potschke P. Quantification of dispersion and distribution of carbon nanotubes in polymer composites using microscopy techniques. In: McNally T, Pötschke P, editors. Polymer-carbon nanotube composites, Preparation, properties and applications. Cambridge, UK: Woodhead Publishing, 2011, pp. 265-294.

20. Kasaliwal GR, Villmow T, Pegel S, Potschke P. Influence of material and processing parameters on carbon nanotube dispersion in polymer melts. In: McNally T, Pötschke P, editors. Polymer-carbon nanotube composites, Preparation, properties and applications. Cambridge, UK: Woodhead Publishing, 2011, pp. 92-132.

21. Lee S, Kimb T-R, Ogale AA, Kimb M-S. Surface and structure modification of carbon nanofibers. Synthetic Metals 2007;157:644-650.

22. Dani A, Ogale AA. Percolation in Short-fiber Composites: Cluster Statistics and Critical Exponents. Compos Sci Technol 1997; 57:1355-1361.

23. Motlagh GH, Hrymak AN, Thompson MR. Improved through-plane electrical conductivity in a carbon-filled thermoplastic via foaming. Polym Eng Sci 2008;48: 687-696.

CHAPTER 6

CONCLUSIONS AND RECOMENDATIONS

In this chapter, the most important concluding remarks of this research are stated. Conclusions from Chapters 2, 3, 4 and 5 are made based on their results, and recommendations are made to draw lines of continuity for this research field.

6.1 Conclusions

In Chapter 2, it was established that a 1-hour heat treatment at 2500°C of PR-19 HT nanofibers led to significant increase in their graphitic crystallinity. Consequently, nanocomposites containing 10 vol% PR-19 HT exhibited an outstanding improvement in their electrical conductivity and EM SE as compared to their untreated counterparts. Over the VHF-UHF frequency, the EM SE of PR-19 HT twin-screw extruded nanocomposites (2.5-mm thick) was 12-16 dB, which was significantly larger than that measured for untreated PR-19 nanocomposites (~1 dB). Absorption was found to be the dominant shielding component of the heat-treated CNF-based composites.

Next, in Chapter 3, composites containing carbon nanomodifiers with similar graphitic crystallinity, but with different morphologies, led to EM SE values directly dependent on the modifier morphology. Thus, at 10 vol%, MWHT HT, whose aspect ratio was the largest, led to the greatest composite conductivity and EM SE (~24 dB). In contrast, the HCNT HT, due to their coiled shape and low aspect ratio, led to highly

segregated composite microstructures with little electrical percolation and low EM SE (<1 dB). Nevertheless, HCNT HT composites exhibited the highest ductility and flexibility, owing to the matrix-modifier interlocking provided by their helical morphology.

In Chapter 4, LLDPE-based composites containing 40 vol% of in-plane randomly oriented carbon nanotubes/nanofibers exhibited EM SE values of up to 25 dB/mm in the VHF-UHF frequencies. Moreover, predictions of the far-field EM SE and its components, using a model for the shielding mechanisms in generally lossy materials (i.e., intermediately conductive), were consistent with the experimental values when the in-plane effective conductivity of the nanocomposites was employed.

Finally, in Chapter 5, a preferred orientation of the dispersed carbon nanomodifiers in LLDPE by the combination of shearing and elongational flow-fields was induced. These composites containing 10 vol% of oriented carbon nanotubes/nanofibers exhibited anisotropic in-plane conductivity and tensile properties. The composites exhibited the highest conductivity in the direction of flow, and displayed shielding anisotropy when polarized electromagnetic waves were applied. Thus, oriented MWNT HT nanocomposites displayed EM SE values of only ~4 dB for perpendicular alignment, but ~11 dB for parallel alignment of modifiers and electric field (WR-340).

In summary, the morphological and intrinsic transport properties of carbon nanomodifiers, their concentration, and the processing methodology are factors that

determine the microstructure and the transport properties of the composites, which, in turn, control their electromagnetic shielding performance.

6.2. Recommendations for future work

As discussed in Appendix A, it was found that shorter mixing times and less shearing mixing geometries led to a higher electrical conductivity and EM SE. However, to further optimize the modifier networks, more sophisticated mixing studies that include distributive and dispersive processing geometries/elements, and different mixing speeds and temperatures may be conducted.

In Chapter 3, the influence of different carbon modifier morphologies on the EM SE of their composite was investigated. It was found that morphologies with large aspect ratio and straight-shape led to higher electrical interconnection, whereas helical shapes led to entanglements that led to a large amount of non-percolating clusters. However, morphologies such as single-walled carbon nanotubes (SWNT), with extraordinary large aspect ratios, were not investigated. These have potential of reaching high composite conductivities at much lower concentrations, although at a much higher cost relative to their multi-walled counterparts. Moreover, higher frequency bands such as X, Ku and K bands can be investigated for radar and satellite systems EMC applications.

The effect of nanomodifier ultra-sonication on the EM SE of their composites was briefly studied [1]. The size of the modifier agglomerates was not significantly reduced

after 45 min of sonication in n-hexane, leading to essentially the same EM SE of that of composites made of unsonicated nanomodifiers. Possibly, a more detailed study on the effect of the initial state of aggregation of the modifiers and matrix before melt-mixing, with a focus on the modifier-matrix interfacial phenomena, is recommended.

Chapter 5 dealt with the effect of anisotropic conductivities impressed by flow-induced orientation. Further studies on the effect of modifier orientation using shearing flow-fields attained by scalable industrial processing techniques such as injection molding are also recommended. Moreover, the Center for Advanced Engineering Fibers and Films (CAEFF) possesses a custom-made biaxial stretching unit in which high levels of biaxial orientation can be attained in the composites.

Finally, in an independent study, special micro-patterned films dies were studied to establish that micro-textured films can be produced by continuous cast-film extrusion [2]. As a follow-up of that project, carbon nanomodifiers, whose dimensions make them suitable for flowing through the micro-channels of the patterned dies, may be used to create conductive textured composite films. These textured nanocomposites may help in various EMC applications such as in high-frequency resonant grating waveguide structures [3].

6.3 References

1. Villacorta BS, Ogale AA. Carbon Nanoparticle-based Flexible LLDPE Composites for Enhanced Electromagnetic Shielding Effectiveness. In: Haghi AK, Thomas S, Shanks R, Joy J, editors. Recent trends in micro and nanostructured polymer systems. Canada: Apple Academic Press, 2013.

2. Villacorta BS, Hulseman S, Cannon AH, Hulseman R, Ogale AA. Continuously Extruded Micro-Textured Polypropylene Films. Polym Eng Sci, DOI 10.1002/pen.23762.

3. Rosenblatt D, Sharon A, Friesem AA. Resonant Grating Waveguide Structures. IEEE J Quantum Electron, 1997;33:2038-2059.

APPENDICES

APPENDIX A

MIXING CONDITIONS

A.1 Mixing time effect

Figures A.1 (a) and **(b)** are representative SEM micrographs displaying the microstructure of the nanocomposites prepared in a DSM Xplore conical twin-screw micro-compounder (DSM) at 190°C and 20 rpm for 20 min and 2 minutes of mixing time, respectively. At the length-scale provided by SEM, the microstructures appear similar for both mixing times, and no isolated clusters were identified in the nanocomposites. Nonetheless, the DC in-plane electrical conductivity of the nanocomposites prepared for 20 min was only 2.0±0.2 S/m, whereas that of the nanocomposites processed for 2 min was 5 times higher, at 10.0±1.0 S/m.

Figure A.2 displays the effect of the mixing time on the EM SE of their nanocomposites in the frequency range of 30 MHz to 1.5 GHz. The EM SE of the nanocomposites mixed for only 2 min displayed values of 15±1.3 dB, whereas those mixed for 20 min exhibited only 6.6±1.4 dB. These results are consistent with the DC conductivity measurements.

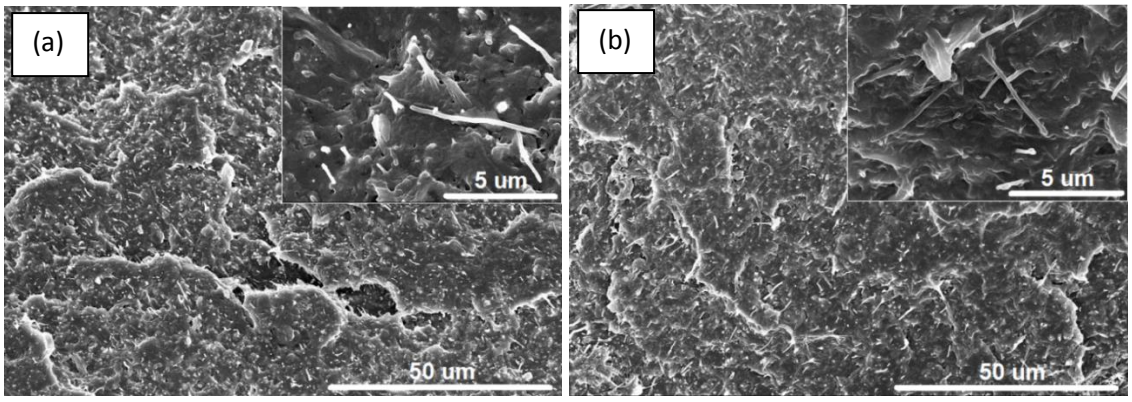

Figure A.1. Representative scanning electron micrographs (SEM) of twin-screw extruded nanocomposites at 10 vol%, 190°C and 20 rpm for (a) 20 min and (b) 2 min of mixing time. Insets display the microstructure at higher magnification.

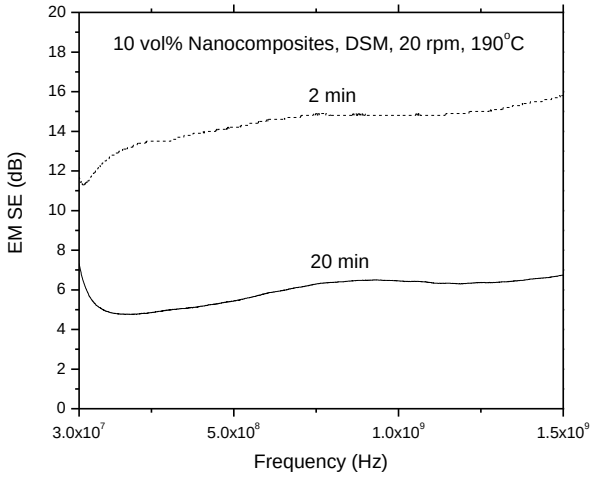

Figure A.2. Electromagnetic shielding effectiveness (EM SE) of twin-screw extruded nanocomposites at 10 vol%, 190°C and 20 rpm for 20 min and 2 min of mixing time.

A.2 Mixing geometry

After determining that shorter mixing times led to higher electrical properties, a mixing geometry that applies less energy of mixing was investigated. Thus, the co-rotational twin-screw geometry (continuous mode) that applies high levels of shear was changed to a Brabender-type geometry of a Rheomix 600 batch mixer (BM) (batch mode). The nanocomposites made in BM at 190°C and 20 rpm for 2 min displayed a DC in-plane conductivity of 20.4±3.3 S/m, which is twice of that of the twin-screw extruded (DSM) nanocomposites made at 190°C and 20 rpm for the same mixing time. The EM SE of the batch-mixed vs. that of the twin-screw-mixed nanocomposites, displayed in **Figure A.3**, shows that that the batch-mixed nanocomposites exhibited a higher shielding performance, reaching values as high as 24.7 dB at 1.5 GHz. Thus, a softer mixing led to composites with higher EM SE.

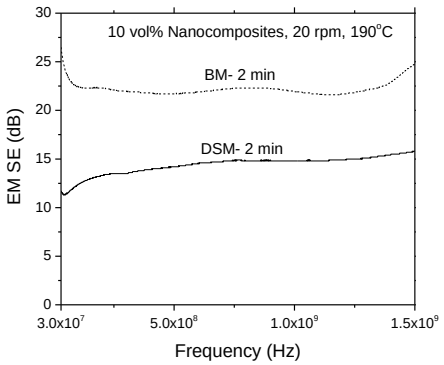

Figure A.3. Electromagnetic shielding effectiveness (EM SE) of twin-screw extruded (DSM) nanocomposites vs. that of the batch-mixed (BM) nanocomposites. Both prepared at 10 vol%, 190°C and 20 rpm for 2 min.

A.3 Melt-dilution

Previous studies have established that melt-dilution can lead to higher levels of electrical network as higher levels of percolating clusters can be retained by certain composite systems [1]. Thus, the batch mixer (BM) was used to make a dilution of a 40 vol% PR-19 HT master batch down to 10 vol%. Processing conditions were held constant at 190°C, 20 rpm, and 2 min for the dilution step. **Figure A.4** displays SEM micrographs comparing the cross-sections of the direct batch and diluted batch. By SEM, the batch-mixed nanocomposites displayed no identifiable clusters in their microstructure, and the CNFs appear to be uniformly distributed all over the matrix. In contrast, the diluted batch led to microstructures with clusters larger than 50 μm in diameter, as well as zones in which a very low concentration of CNF was observed. This indicates that, under these mixing conditions, the geometry of the batch mixer did not provide enough mixing energy to establish cluster interconnections. As a result of this segregated microstructure, the diluted batch of nanocomposites displayed a DC in-plane conductivity of only 0.08±0.01 S/m, which is about two and a half orders of magnitude lower than that of the direct batch prepared by the same mixing conditions.

Figure A.5 displays the EM SE of the diluted batch as compared with that of the direct batch. The diluted batch displayed EM SE values of only 2.8±1.1 dB, whereas the direct batch of 23.4±2.0 dB. Hence, the EM SE of the composites was dependent on the microstructure impressed by the different processing conditions.

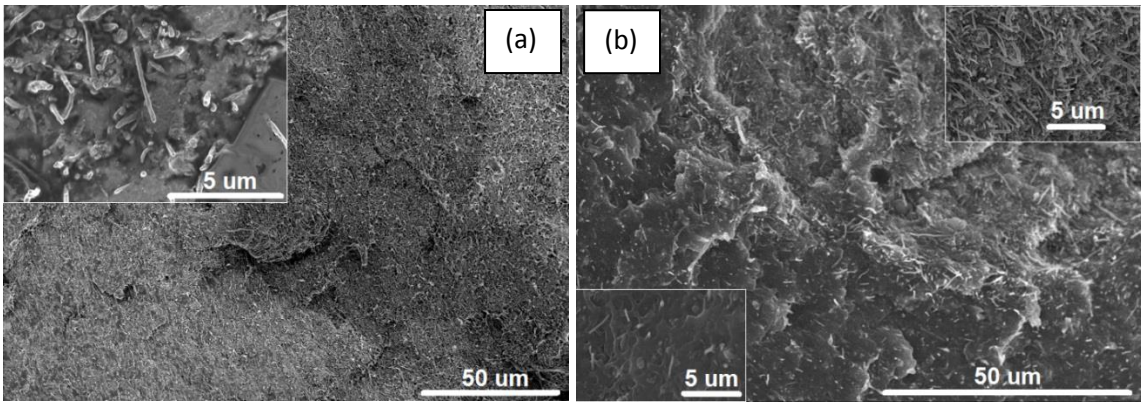

Figure A.4. Representative scanning electron micrographs (SEM) of nanocomposites at 10 vol%, and prepared at 190°C and 20 rpm for 2 min (a) direct batch (b) diluted batch. Insets display the microstructure at higher magnification.

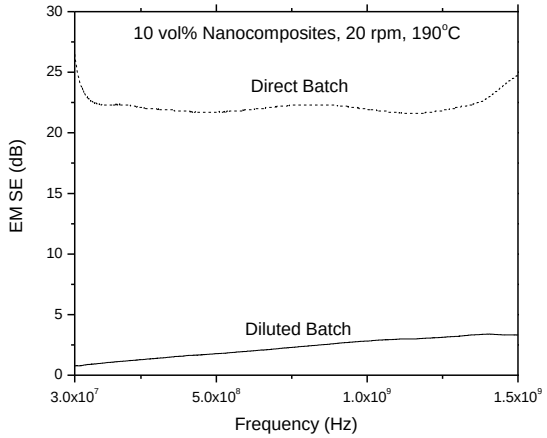

Figure A.5. Electromagnetic shielding effectiveness (EM SE) of the diluted batch of nanocomposites vs. that of the direct batch. Both prepared at 10 vol%, 190°C and 20 rpm for 2 min.

A.4 References

1. Villmow T, Kretzschmar B, Pötschke P. Influence of Screw Configuration and Mixing Conditions in Twin-Screw Extrusion on Dispersion of MWNT in PCL Composites. SPE ANTEC 2010, PENG-11-2010-0509.

2. Nobile MR. Rheology of polymer-carbon nanotube composite melts. In: McNally T, Pötschke P, editors. Polymer-carbon nanotube composites, Preparation, properties and applications. Cambridge, UK: Woodhead Publishing, 2011, pp. 428-481.

3. Makosco CW. Rheology: Principles, Measurements, and Applications. United States of America: Wiley-VCH, Inc., 1994.

APPENDIX B

EXPERIMENTAL PROCEDURES

B.1 Electromagnetic shielding effectiveness (EM SE)

Figure B.1 is a representation of a specimen shielding an EM wave with incident power, P_o. When the wave strikes the material, due to the change in wave impedance, part of that power is reflected back, P_R [1]. Another part of that power passes through the material while being absorbed by the material and converted into heat, P_A, whereas the remainder gets transmitted, P_T [1]. [1, 2].

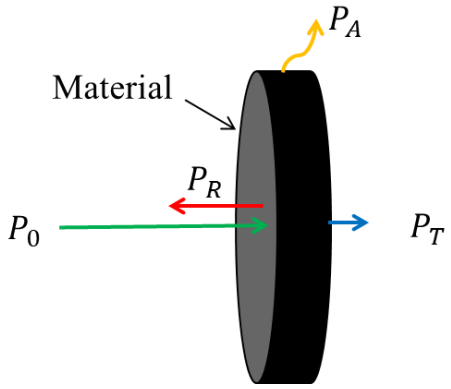

Figure B.1. Schematic representation of a shielding material interacting with an electromagnetic wave of incident power, P_o.

Figure B.2 is a schematic that shows a slotted coaxial transmission line connected to a two-port network analyzer. The network analyzer sends a wave through the line from port 1 to port 2, passing through the material. The network analyzer measures the received power at the ports, relative to the incident power. These ratios are given by the

scattering parameters, S_{ij} (i.e., reflection or scattering matrix), which relate the incident power to the powers reflected from the ports [1]. Thus, $|S_{21}|^2$ is the power ratio of the power received in port 2 to that sent from port 1, $\left|\frac{P_T}{P_0}\right| = |S_{21}|^2$. $|S_{11}|^2$ is the power ratio of the power received in port 1 to that sent from the same port 1, $\left|\frac{P_R}{P_0}\right| = |S_{11}|^2$. Therefore, the uncorrected $EM\ SE'$ and $EM\ SE_R{}'$ are respectively obtained from the scattering parameters obtained from the network analyzer by [2]:

$$EM\ SE' = -10\log(|S_{21}|^2) \tag{B.1}$$

$$EM\ SE_R{}' = -10\log(1 - |S_{11}|^2) \tag{B.2}$$

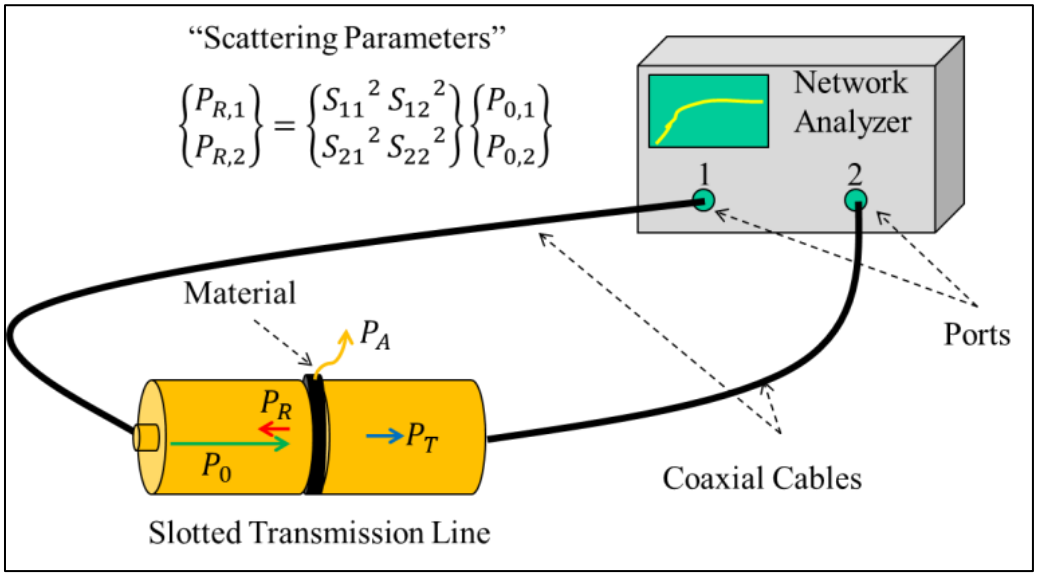

Figure B.2. Schematic representation of a coaxial transmission line connected to a network analyzer for the computation of the scattering parameters.

Because SE is defined as the attenuation relative to the situation when no shielding material is present, corrections must be made to the measurements shown in Eqns. (B.1) and (B.2). **Figure B.3** displays the ASTM D4935 method that includes such corrections in a coaxial line measurement. The corrected values of SE are obtained by subtracting the attenuation measured with a "reference" specimen from that of the "load" specimen. This corrects for capacitive coupling effects and intrinsic absorptive and reflective characteristics of the transmission line as distorted by presence of the load specimen. In other words, the reference specimen measurement sets a base-line for the measurements. Thus, two sets of data are measured: a) one for the test (also called "load") specimen, b) and one for the reference specimen.

The load specimen needs to be a planar sample of the material being tested with dimensions large enough to cover the whole fixture/waveguide flange (material measurement). The reference specimen has an aperture with the shape and dimensions of the flange of the fixture/waveguide (base-line measurement). The reference specimen is made of the same material and thickness than that of the load specimen.

The subtraction of the measurements made with the specimens relative to the incident power, P_o, is mathematically equivalent to the shielding effectiveness definition as the logarithmic ratio of the transmitted power with the material present, $P_{T,\ W}$, to the transmitted power without the material present, $P_{T,\ WO}$ (Eqn. B.3). This concept is also depicted in **Figure B.3.**

$$EM\ SE\ (dB) = -10\ log\frac{P_{T,\ W}}{P_{T,\ wo}} = \left(-10\ log\frac{P_{T,\ W}}{P_0}\right) - \left(-10\ log\frac{P_{T,\ WO}}{P_0}\right) \qquad \text{(B.3)}$$

Similarly, Eqn. B.4 defines the correction for the reflective EM SE measurement, (obtained from the reflected power with the material present, $P_{R,\ W}$, and the reflected power without the material present, $P_{R,\ WO}$), which is essentially based on the same concept of reference correction. Here, intrinsic reflective characteristics of the transmission line itself are similarly subtracted with the reference specimen measurement.

$$EM\ SE_R\ (dB) = -10\ log\left(\frac{P_o - P_{R,\ W}}{P_o - P_{R,\ WO}}\right) = \left(-10\ log\left(1 - \frac{P_{R,\ W}}{P_0}\right)\right) - \left(-10\ log\left(1 - \frac{P_{R,\ WO}}{P_0}\right)\right) \quad \text{(B.4)}$$

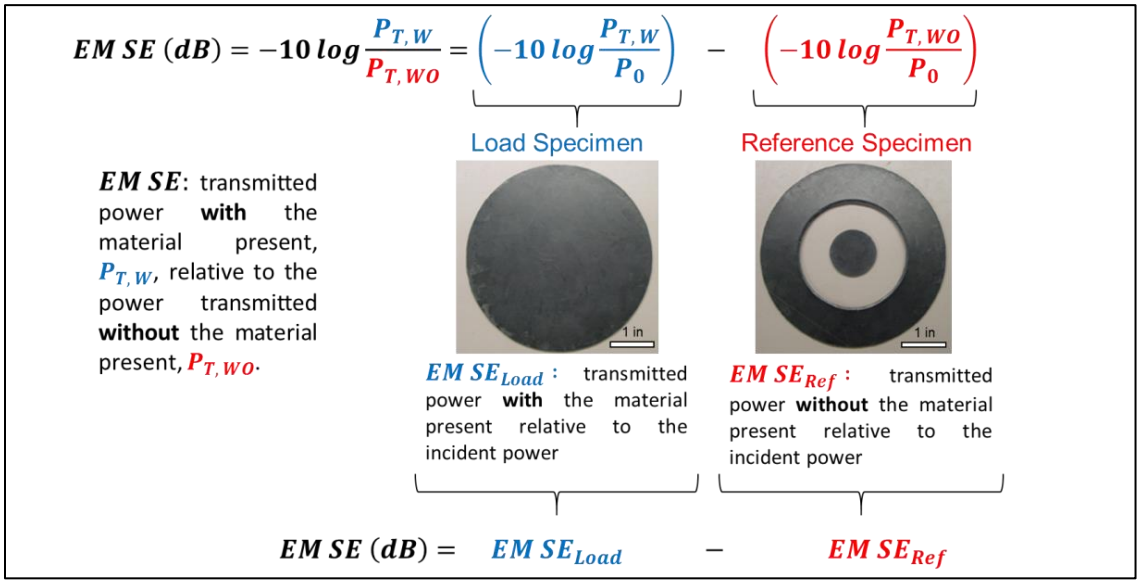

Figure B.3. ASTM type of measurements for EM SE including the reference correction.

Thus for the SE measurements, two set of measurements are recorded: $|S_{21}|^2{}_{Load}$ and $|S_{11}|^2{}_{Load}$ for the load specimen, and, $|S_{21}|^2{}_{Ref}$ and $|S_{11}|^2{}_{Ref}$ for the reference specimen. The following analysis will explain how the definitions from Eqn. B.3 and Eqn. B.4 are obtained from the scattering parameters.

For the load and reference specimens, the respective power balances are [3]:

$$P_o = P_{T,\ Load} + P_{R,\ Load} + P_{A,\ Load} \tag{B.5}$$

$$P_o = P_{T,\ Ref} + P_{R,\ Ref} + P_{A,\ Ref} \tag{B.6}$$

which are equivalent to:

$$1 = \frac{P_{T,\ Load}}{P_o} + \frac{P_{R,\ Load}}{P_o} + \frac{P_{A,\ Load}}{P_o} = T_{Load} + R_{Load} + A_{Load} \tag{B.7}$$

$$1 = \frac{P_{T,\ Ref}}{P_o} + \frac{P_{R,\ Ref}}{P_o} + \frac{P_{A,\ Ref}}{P_o} = T_{Ref} + R_{Ref} + A_{Ref} \tag{B.8}$$

where T_{spec}, R_{spec} and A_{spec} are the transmittance, reflectance and absorbance for each specimen (spec) type.

For the load specimen, the transmittance and reflectance are obtained (in dB) from the analyzer as:

$$T_{Load,\ dB} = |S_{21}|^2{}_{dB,\ Load} = -10\ \log\left|\frac{P_{T,\ Load}}{P_o}\right| \tag{B.9}$$

$$R_{Load,\ dB} = |S_{21}|^2{}_{dB,\ Load} = -10\ \log\left|\frac{P_{R,\ Load}}{P_o}\right| \tag{B.10}$$

Similarly, for the reference specimen, the transmittance and reflectance (in dB) obtained respectively are:

$$T_{Ref,\ dB} = |S_{21}|^2{}_{dB,\ Ref} = -10\ \log\left|\frac{P_{T,\ Ref}}{P_o}\right| \tag{B.11}$$

$$R_{Ref,\ dB} = |S_{21}|^2{}_{dB,\ Ref} = -10\ \log\left|\frac{P_{R,\ Ref}}{P_o}\right| \tag{B.12}$$

For the further analysis, the scattering parameters are needed in their fractional or decimal form. To obtain the fractional reflectance and transmittance for each specimen the antilog is used:

$$T_{Load} = |S_{21}|^2{}_{Load} = 10^{-\frac{|S_{21}|^2{}_{dB,\ Load}}{10}} \tag{B.13}$$

$$R_{Load} = |S_{11}|^2{}_{Load} = 10^{-\frac{|S_{11}|^2{}_{dB,\ Load}}{10}} \tag{B.14}$$

$$T_{Ref} = |S_{21}|^2{}_{Ref} = 10^{-\frac{|S_{21}|^2{}_{dB,\ Ref}}{10}} \tag{B.15}$$

$$R_{Ref} = |S_{11}|^2{}_{Ref} = 10^{-\frac{|S_{11}|^2{}_{dB,\ Ref}}{10}} \tag{B.16}$$

The corrected EM SE is defined by:

$$EM\ SE\ (dB) = (-10\log T_{Load}) - (-10\log T_{Ref}) = -10\log\frac{T_{Load}}{T_{Ref}} \tag{B.17}$$

Defining $T = |S_{21}|^2 = \frac{T_{Load}}{T_{Ref}}$ as the corrected transmittance, the corrected EM SE is therefore:

$$\boxed{EM\ SE = -10\log T} \tag{B.18}$$

which is equivalent to the definition of Eqn. B.3.

Similarly, the corrected reflective EM SE is:

$$EM\ SE_R(dB) = (-10\log(1 - R_{Load})) - (-10\log(1 - R_{Ref})) = -10\log\frac{(1-R_{Load})}{(1-R_{Ref})} \tag{B.19}$$

where, $(1-R) = 1 - |S_{11}|^2 = \frac{(1-R_{Load})}{(1-R_{Ref})}$ or $R = \frac{R_{Load}-R_{Ref}}{1-R_{Ref}}$. Sometimes R_{Ref} is very small, then $R \approx R_{Load}$. Therefore, the corrected reflective EM SE is:

$$\boxed{EM\ SE_R = -10\log(1-R)} \tag{B.20}$$

which is equivalent to the definition of Eqn. B.4.

The corrected absorptive EM SE can be calculated from the balance as:

$$\boxed{EM\ SE_A = EM\ SE - EM\ SE_R} \tag{B.21}$$

These equations can be used not only for measurements in a coaxial line, but also for other waveguide shapes, such as rectangular/circular waveguides and micro-strip lines. **Figure B.4** displays the different experimental set-ups by which the EM SE measurements were conducted for this study. Networks analyzers were used to generate and measure the fields by connecting the fixtures through coaxial cables. The EM SE was obtained by the method described above

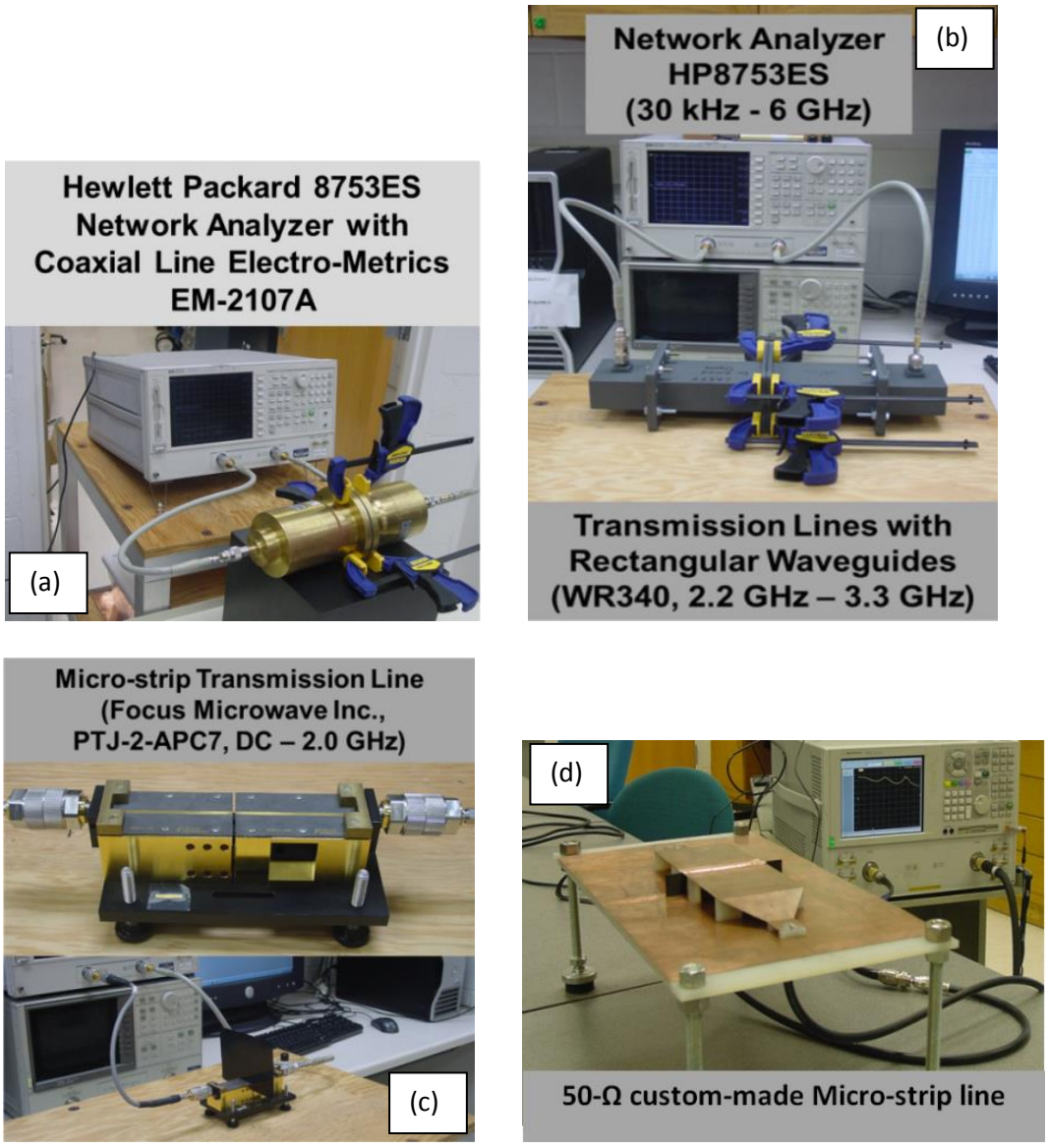

Figure B.4. Experimental set-ups for: a) split coaxial line, b) split rectangular wave-transmission line, c) split micro-strip line, and d) continuous micro-strip line.

B.2 Electrostatic decay (ESD)

The static decay time was measured using an Electro-Tech Systems, Inc. 406D Static-Decay Meter that complies with the Federal Test Method 101D, Method 4046 and Military Standard Mil-B-81705C (**Figure B.5**). This standard requires that 99% of the initial induced charge be dissipated is less than 2 seconds for qualifying material per Mil-B-81705C. The samples are placed inside of the Faraday's cage and tested using the following procedure:

1. Press the "POWER" button and set "HIGH VOLTAGE" off.
2. Allow 15 min for warm-up.
3. Place STM-1 test module in sample holder electrodes
4. Insert white banana plug into jack on chassis.
5. Cage cover is down and select "+ HIGH VOLTAGE".
6. Rotate "HIGH VOLTAGE ADJUST" for "+5KV" on "CHARGING VOLTAGE" meter.
7. Select "MANUAL" mode and "10% CUTOFF".
8. "SAMPLE CHARGE" meter was set to "0" by adjusting "ZERO" control.
9. Press "CHG" button and adjust "FULL SCALE" control (STM-1 position) for setting "+5KV" reading on "SAMPLE CHARGE" meter.
10. Press "ZERO/STBY" button and recheck "0" setting.
11. Press "CHG" button. When "SAMPLE CHARGE" meter reads "+5KV", press "TEST" button. Decay time should equal time on STM-1±0.05 sec.
12. Repeat steps 8-11 for -5KV. Measured decay time should be within 0.2sec of time measured at +5KV
13. Select desired "CUTOFF" and press "CHG" button.
14. Check "SAMPLE CHARGE" meter read "0".
15. Place a 3" X 5" aluminum foil in test cage electrodes.
16. Select "+5KV" and adjust "FULL SCALE" control ("NORM" position) for "+5KV" reading on "SAMPLE CHARGE" meter.
17. Do not readjust this control when testing samples.
18. Remove foil and place test sample in sample holder electrodes.
19. Press "ZERO/STBY" button and adjust "ZERO" setting.

20. Press “CHG” button. When “SAMPLE CHARGE” meter reads full scale, press “TEST” button.
21. Record measures decay time displayed on the screen.
22. Repeat steps 14-21 for “-5KV”.

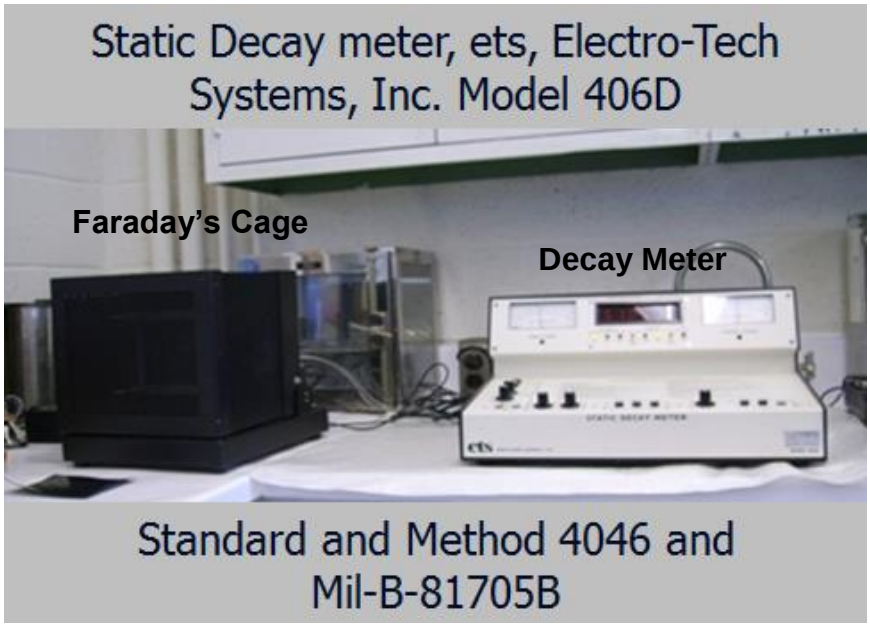

Figure B.5. Picture displaying the static decay meter.

B.3 DC electrical conductivity

The DC electrical conductivity measurements were conducted according to the ASTM D257 standard with a Keithley 6517B High Resistance Meter (1 pA to 20 mA, 0 to ±1000 Volts) as shown in **Figure B.6**. The alternating polarity method was applied with the Keithley 6524 software. To measure through-thickness conductivity, the Keithley 8009 Resistivity Test Fixture was used in conjunction of the Keithley 6517B.

Figure B.6. Keithley 6517B High Resistance Meter and Keithley 8009 Resistivity Test Fixture.

The measurements were carried out by the following steps:

1. A sample with dimensions no larger than 75 mm x 75 mm x 3 mm is placed in the fixture.
2. From Programs/Keithley/6517 Hi-R Test, the 6517 Hi-R Test.exe must be executed from the Keithley 6524 software. A dialogue box with preset numbers will pop up. (displayed in **Figure B.6** in the computer's monitor)
3. The option for "volume resistivity" is chosen in the fixture and in the 6524 software.
4. The fixture is closed with the sample inside. Make sure the clamp is fully close for a proper contact of the sample and electrodes.
5. In the software option "Geometries" the sample thickness is entered and the option for Keithley 8009 is chosen. By choosing this, the software will calculate the electrode area for resistivity computation.
6. The alternating voltage is set in the dialogue box of the software (0 to ±1000 V). Preset as 50 V.

7. The current range is chosen in the software (1 pA to 20 mA). Auto range can also be used but is less accurate than doing a set of trials to determine the most appropriate current range.
8. The measure time is preset at 15 s. A different value can also be set by the user.
9. The offset voltage is typically set as zero. A different value can also be set by the user.
10. The number of readings to discard is preset as 3. A different value can also be set by the user.
11. The number of readings to store is preset as 8. A different value can also be set by the user.
12. The voltage is applied across the circular electrodes with the 6524 software by pressing "Run".
13. The progress of the measurement is shown in a set of plots and graphs and at the blank space of the option "Resistivity (Ohm.cm)".
14. The set of measurements can be save by pressing "Save/Load"

To measure the in-plane resistivity, the Keithley 8002A Test Fixture modified with external electrodes was used. Silver paint was applied at the opposite ends of the samples. The measuring procedure is the same as that with the 8009 fixture, with the exception that instead of selecting "Volume Resistivity", the option for "Resistance" must be chosen in the software. Then the resistivity must be computed from the sample geometry and the measured resistance.

B.4 AC electrical permittivity

The AC electrical permittivity was measured in an Agilent 4291B RF Impedance/Material Analyzer (**Figure B.7**) connected to an Agilent 16453A Dielectric Material Test Fixture (**Figure B.7**) using the following steps:

1. Connect the High Impedance Head to the Agilent 4291B RF Impedance/Material Analyzer.
2. Turn on the power button. Give the equipment about 30 minutes to warm up.
3. Carry out the calibration of the analyzer. Thus, Open/Short/Load (50 Ω) calibration with the calibration quit. The equipment will ask for each calibration elements.
4. After the calibration is done. Connect the Agilent 16453A Dielectric Material Test Fixture to the Impedance Head. The permittivity fixture 16453 option must be selected.
5. Input thickness of the Teflon specimen (0.5 mm). Provided by the equipment.
6. Perform short fixture compensation.
7. Perform open fixture compensation.
8. Perform load (Teflon specimen) fixture compensation.
9. Place the sample (MUT) to measured and enter its thickness.
10. Format options of the results can be chosen as Cole-Cole plot, real and imaginary relative permittivity as functions of frequency and tan δ.

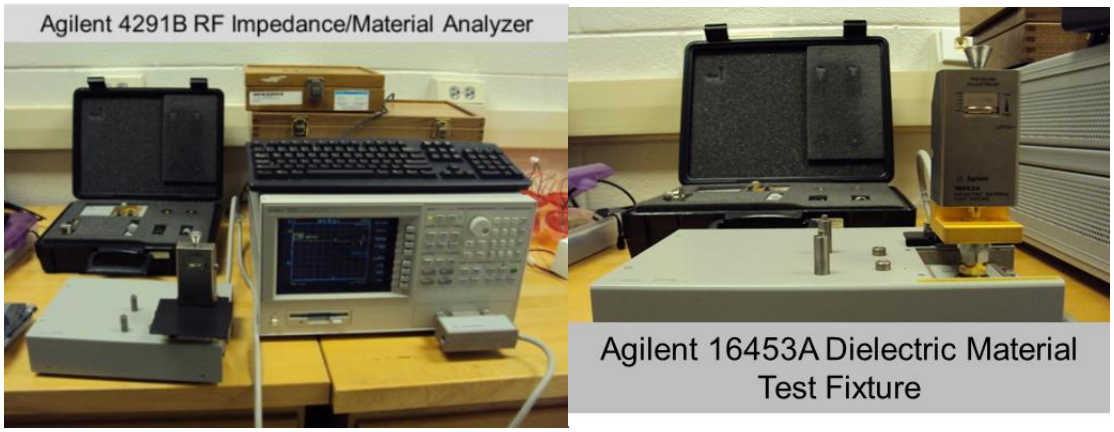

Figure B.7 Agilent 4291B RF Impedance/Material Analyzer and Agilent 16453A Dielectric Material Test Fixture.

B.6 References

1. Pozar DM. Microwave Engineering. United States of America: Addison-Wesley Publishing Company, Inc., 1990, 2005.

2. Villacorta BS, Ogale AA, Hubing TH. Effect of Heat Treatment of Carbon Nanofibers on the Electromagnetic Shielding Effectiveness of Linear Low Density Polyethylene Nanocomposites. Polym Eng Sci 2013;53:417-423.

APPENDIX C

WAVE PROPAGATION MODES

C.1 Wave Modes

Figure C.1 exhibits (a) a typical coaxial line, (b) a rectangular waveguide, and (c, d) micro-strip lines in which the attenuation of the EM field by a sample can be measured. Different geometries in a transmission line develop different wave propagation modes. A transverse electromagnetic (TEM) wave propagation mode is that in which both fields, electric and magnetic, are perpendicular to the direction of wave propagation. A transverse electric (TE) wave is one where the electric field is perpendicular to the direction of propagation, but there is no restriction for the magnetic field, allowing magnetic field in the direction of propagation. A transverse magnetic (TM) wave is the opposite of a TE, allowing the electric field in the direction of wave propagation, but restricting the magnetic perpendicularly to the direction of propagation.

A coaxial line will primarily develop TEM waves, whose electric and magnetic fields are perpendicular to the direction of wave propagation. It can also support other modes such as the TE_{11} but they are of less relevance [1]. **Figure C.2** depicts the most important wave propagation modes in a coaxial line. A radial polarization is imposed by this geometry for the TEM mode.

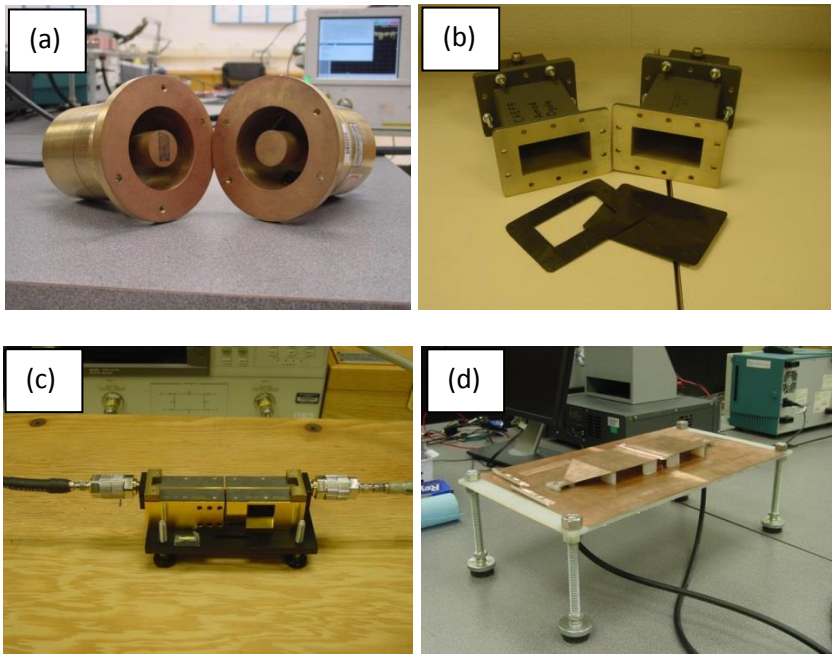

Figure C.1. Transmission line fixtures for electromagnetic attenuation measurements (a) an Electro-Metrics EM-2107A split coaxial line 50Ω, (b) WR340 rectangular waveguide with representative load and reference specimens 50Ω, (c) a 50Ω FOCUS Microwave Inc. PTJ-2-APC7 slotted micro-strip transmission line and (d) a 50Ω custom-made continuous micro-strip transmission line.

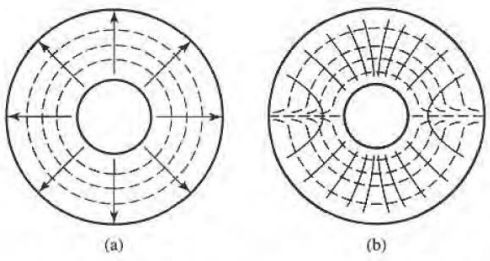

Figure C.2. Coaxial transmission line fields (a) TEM mode and (b) TE_{11} mode. Adapted from [1].

For a micro-strip line, a quasi-TEM mode is primarily developed. **Figure C.3** displays the geometry and fields for a micro-strip line. Notice the vertical wave polarization for the region in between the conducting trace and the underlying ground plane.

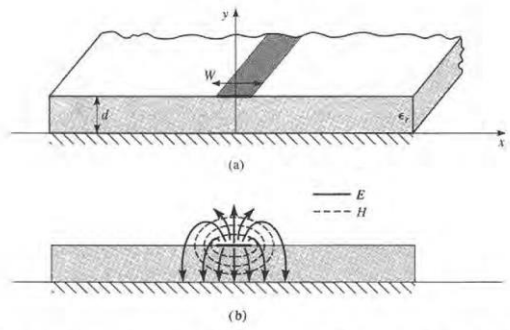

Figure C.3. Micro-strip line: (a) geometry and (b) field lines in a quasi-TEM mode [1].

The wave modes developed in a rectangular waveguide are far more complicated. **Figure C.4** displays the different modes that a rectangular waveguide supports. The predominant modes are the TE_{10} and TE_{20} that display vertical wave polarizations (perpendicular to the largest dimension of the waveguide) [1].

C.2 References

1. Pozar DM. Microwave Engineering. United States of America: Addison-Wesley Publishing Company, Inc., 1990, 2005.

2. Ramo S, Whinnery JR, Van Duzer T. Fields and Waves in Communication Electronics. United States of America: John Wiley & Sons, Inc., 1984.

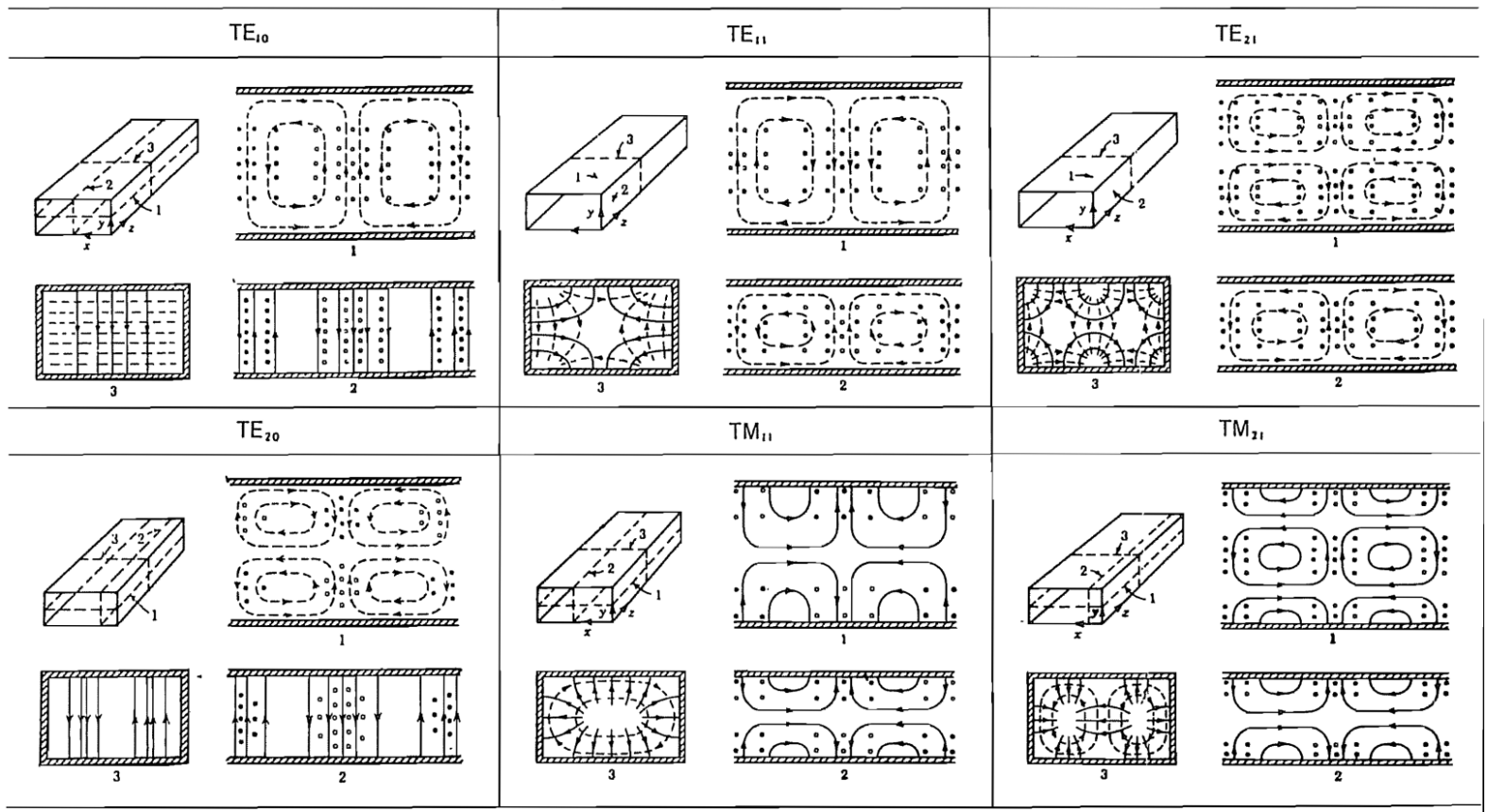

Figure C.4. Wave modes in a rectangular waveguide. Electric and Magnetic fields continuous and discontinuous, respectively. Adapted from [2].